SAPIENZA
UNIVERSITÀ DI ROMA

A study of wall-injected flows into closed–open rectangular cylinders

Dipartimento di Ingegneria Meccanica e Aerospaziale

Dottorato di Ricerca in Meccanica Teorica e Applicata – XXX Ciclo

Candidate

Andrea Perrotta
ID number 1229828

Thesis Advisors

Prof. Giovanni Paolo Romano
Prof. Bernardo Favini

A thesis submitted in partial fulfillment of the requirements
for the degree of Doctor of Philosophy in Theoretical and Applied Mechanics

October 19, 2017

Thesis defended on Month Day, 2018
in front of a Board of Examiners composed by:

Prof. Nome Cognome (chairman)
Prof. Nome Cognome

A study of wall-injected flows into closed–open rectangular cylinders
Ph.D. thesis. Sapienza – University of Rome

This thesis has been typeset by LaTeX and the Sapthesis class.

Version: December 18, 2017

Author's email: andrea.perrotta@uniroma1.it

Contents

List of Figures

List of Tables

Preface

The present work concerns with the study of the fluid motion within a channel when a gas is injected from its wall. This kind of flow appears in a wide variety of engineering applications and it is realized either with low or high injection velocity. The most fruitful scientific production about this argument comes from the propulsive community. In fact, a Solid Rocket Motor (SRM) is a hollowed cylinder, whose inner walls burn and hence inject gas into a channel. Thus, propulsive applications involves wall-injected flows and combustion. Actually, the most of combustion takes place in a very thin limited region near the propellant (the flame) and it is often neglected in modeling. However, pressure and temperature are extremely high in a SRM. Therefore, due to this extreme condition, real firing tests provide a number of dataset limited to the number of probes. Usually, sophisticated pressure transducers, withstanding high temperature, placed at the head-end and aft-end of the motor and ultra-sound pads are employed in order to gauge pressure oscillations and monitor the radial regression of the propellant surface. As stated in [1], it is extremely hard to equip model rocket motor to allow for visual access to its interior and also punctual temperature are of limited interest. A first simplification had been to employ a cold flow injected into a hollow cylinder. Although it has been very useful to confirm theoretical predicted instabilities, also this experimental equipment was limited to punctual measurements. A further simplification leads to a closed-open rectangular cylinder, which can be seen as a bi-dimensional approximation of what happens in three-dimensions. Despite this kind of configuration have been developed, moreover with visual access, it has been mostly used for visualizations and no global flowfield measurements were conducted.

In this work, a closed-open rectangular cylinder has been adopted in order to obtain a global velocity flowfield by means of Particle Image Velocimetry (PIV). The test section of the experiment is a 24 cm-long, 4 cm-wide and 2 cm-high rectangular channel into which a mixture of air and oil droplets, necessary to the PIV measurement, is injected through a porous material in order to simulate the propellant gas injection. As the propellant heterogeneity, the injection due to the flame presents a non-trivial spatial pattern and unsteady temporal behavior. Therefore, the porosity of the adopted material has been investigated in order to understand whether it yields a simulative phenomenon of the propellant flame evolution and, if so, which is the mechanism behind it. Since porosity implies morphological structures of the material of the dimensions of tens of a micron, a high resolution measuring technique is required for the analysis of the flow generated from the injection through this porous material. Hence, Single Pixel Ensemble Correlation PIV, which has a resolution as small as one pixel, has been applied in addition to the more classical Window Correlation technique, which has instead a resolution related to the window size, usually around 16 pixel. The velocity field of the whole channel, reconstructed by means of Window Correlation PIV, is then compared with analytical models opportunely presented. The influence of the flow structure due to porosity has been analyzed. The injection Reynolds number, based on the injection velocity and the height of the channel, for the present set-up is around 100 and the flowfield does not seems to show any transition to turbulence within the full length of the channel.

The presence of corners and cavities is a fundamental point of interest for a better comprehension of the internal fluid dynamics of a SRM. Therefore, a second configuration has been taken into account. It presents a ninety degrees corner backward facing step, on the injecting wall, doubling the port area, and a subsequent non-porous, movable block forming a cavity. Investigations have been performed for different cavity lengths and in presence or not of injection from the bottom of the cavity itself. This aspect is strictly related to the flow structure at the aft region of a segmented grain with a tubular segment at the head followed by a star-shaped segment. In fact, the star-shaped segment and the nozzle form a cavity that injects until the propellant of the star-shaped segment burns, thereafter the cavity becomes inert and the flow is due to the tubular segment. The capability of a numerical scheme to accurately solve acoustic waves is fundamental in this circumstance, because the acoustical interaction plays a crucial role in the fluid dynamics of cavities.

Definitely, numerical simulations provide a more complete outline and will be also employed in order to compare and go beyond the limitations of the experimental apparatus. A numerical code has been developed implementing high order centered finite difference schemes for the compressible Navier-Stokes equations. Since the physical phenomenon is confined into a bounded region with several boundary conditions, the Navier-Stokes Characteristics Boundary Conditions (NSCBC) technique has been adopted. It consists in a local one-dimensional approximation near the boundary, where the method of the characteristics is adopted in order to adequately compute the quantities deriving from the boundary conditions. Since a fourth-order finite difference scheme has been adopted, a selective low-pass filtering process was mandatory in order to overcome the spurious naturally arising oscillations. Moreover, the coefficients of the schemes and filters have been chosen so that the scheme minimizes the dispersion error in order to solve the acoustical waves as accurately as possible.

The present thesis is organized as follows:

Chapter 1 The state of the art of wall-injected flows is presented. Possible applications, such as film cooling, boundary layer control, filtration, mixing systems and solid rocket motor modeling, are presented. Furthermore, the mathematical formulation of this kind of flow is reported and has been used to derive several analytical solutions under different hypothesis — e.g. irrotational, rotational, viscous, compressible — that will be used as a comparison with experimental and numerical data.

Chapter 2 A brief introduction to the Particle Image Velocimetry is reported, giving the basic tools of the Window Correlation and Singel Pixel Ensemble Correlation techniques to the readers who do not have any experience in optical methods of velocimetry. After a detailed description of the experimental apparatus, the measurements are illustrated. First, the injection characterization with particular attention to the jet coalescence phenomenon. Afterwards, the whole channel measurements for both straight and cavity configurations are analyzed.

Chapter 3 The numerical code development is presented. In particular, the construction of the scheme coefficients and the implementation of the boundary conditions. A detailed study of the outflow boundary condition, which revealed the most knotty one, is reported. Then a validation with benchmark problems is carried on. Simulations of the experimental apparatus are conducted in order to enlarge the range of available data, such as pressure.

Chapter 4 Concluding remarks and comparisons between experimental data and numerical simulation are discussed. Further investigations and possible improvements are suggested.

Chapter 1

General considerations

In this chapter general considerations about the study of wall-injected flows, their possible applications and physical models that have been adopted are presented. *Wall-injected flows* are those flows arising when a fluid comes from a wall either because it passes through the wall itself, as in the case of a filtering wall, or because it is generated at the wall, for instance when the wall burns. Clearly, while the latter case involves chemical reactions, which are typical of combustion, the former is pure cold-fluid dynamics.

1.1 Applications and state of the art

As explained in the preface, this study on wall-injected flows has been inspired by the flow taking place into Solid Rocket Motors (SRM). Typically [2], a schematic representation of a SRM is a hollow cylinder surrounded by a thermal protected case with a chocked nozzle at one end, which is essential to accelerate the flow. When combustion is activated, the inner wall of that cylinder burns emitting gas until the propeller is completely exhausted. A real representation of a SRM, instead, should take into account the complex geometry of the propellant grain, which actually is far from a straight cylinder, the physics of chemical reactions and gas mixtures and the presence of solid particulates that pop up during grain degradation [3, 4, 5]. Since the realistic problem requires a huge effort, it is very common in literature the study of a schematic representation, even simpler than the one reported above, i.e. with a planar surface, among others [6], instead of a cylindrical. One of the most important aspect related to SRMs is the coupling

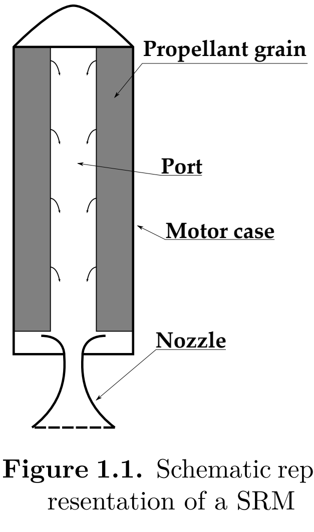

Figure 1.1. Schematic representation of a SRM

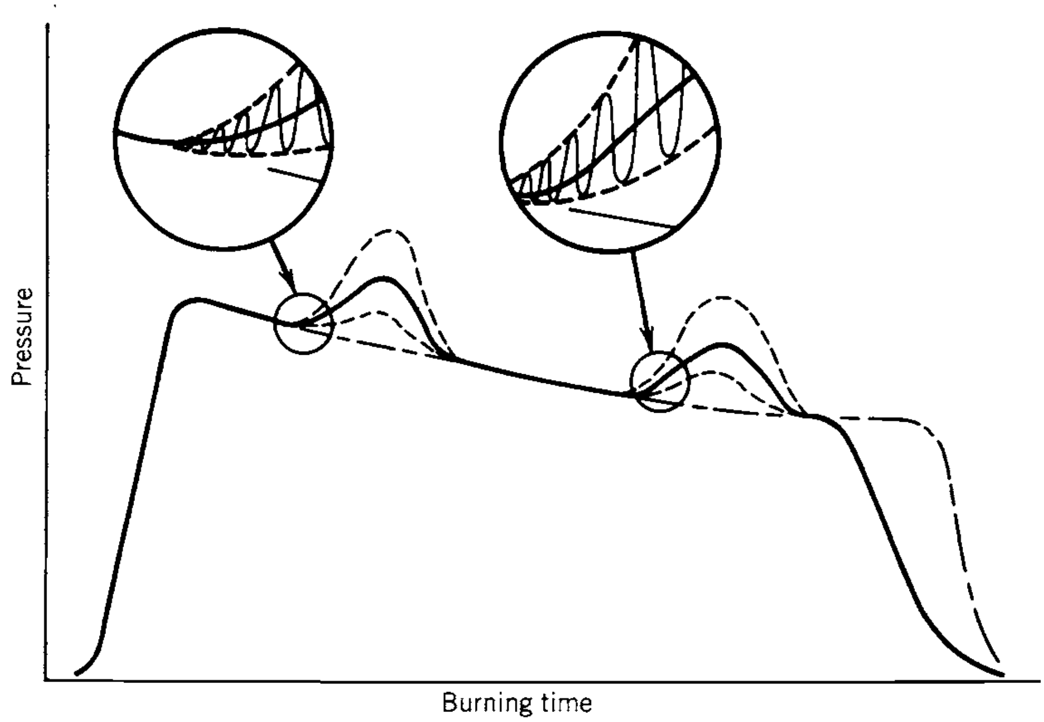

Figure 1.2. Simplified diagram showing two periods of instability in the pressure-time history. The dashed lines show the upper and lower boundaries of the high-frequency pressure oscillations and the dot-dash is the behavior without instability. Extracted from [9]

between pressure oscillations of the combustion chamber and wall-injected flow [7, 8]. Solid rocket motors length ranges from 1.2 m (STAR$^{\text{TM}}$ 27) to 38.4 m (US Space Shuttle Solid Rocket Booster) and consequently the average chamber pressure levels are different: 30 bar for the STAR$^{\text{TM}}$ 27 and 62 bar for the US Space Shuttle Solid Rocket Booster; [9]. The study of SRMs requires, among others, the understanding of the pure hydrodynamics of wall-injected flows and its coupling with the acoustics of a pressurized chamber, which can lead to pressure oscillations of more than 30% of the chamber pressure [9], see Fig. 1.2. In fact, while acoustically "softer" than a liquid rocket combustion chamber, because of the presence of stronger damping factors such as solid particles and viscoelastic materials, the port of a SRM is still a low-loss acoustical cavity containing a very large acoustical energy source, the combustion itself. Note that pressure oscillations of about 0.5% of the mean value can generate thrust oscillations about 5% of the mean thrust value [10].

Wall-injected flows appear widely in many engineering applications, not only for solid rocket motors modeling but also for the design of nuclear reactors [11, 12], food-drying/cooling processes [13], purification by reverse osmosis, fuel cell stacks, filtration [14], design of injectors and mixing systems [15, 16], boundary layer

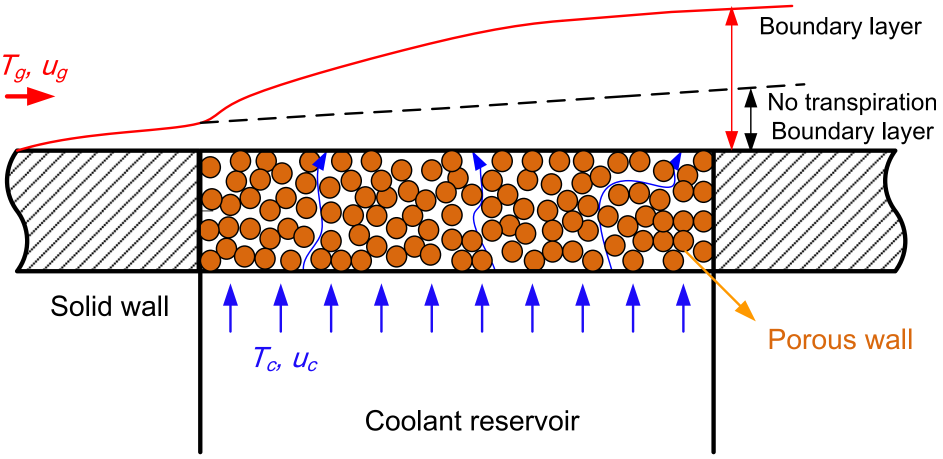

Figure 1.3. Schematic representation of a cooling system with coolant wall injection. Extracted from [27]

control [17, 18, 19, 20], and cooling systems [21, 22, 23, 24, 25, 26, 27, 28]. The main difference between solid rocket motors applications and all those enumerated above is that the injected flow crosses a main flow, see Fig. 1.3 for a schematic representation of a cooling system. In addition, the injecting Reynolds number, i.e. $\mathrm{Re_w} = v_\mathrm{w} H/\nu$ where v_w is the injecting velocity and H the height of the channel, is much higher in SRM, say $\mathrm{Re_w} \sim 1000$ rather than $\mathrm{Re_w} \sim 10$ for the other flows.

Berman [29] was among the earliest to examine the problem of laminar viscous flow bounded by porous surfaces. He has shown, for a planar configuration with wall suction, that Navier-Stokes equations can be reduced to a fourth order non-linear ordinary differential equation. His approach is based on a spatial similarity, i.e. the transverse velocity v is axially invariant, leading to a stream function $\psi(x, y) = xF(y)$. In order to find the mean flow function $F(y)$, Berman adopted a series expansion in $|\mathrm{Re_w}| \sim \epsilon$, and therefore its analytical solution is valid only for $|\mathrm{Re_w}|$ of the order of the unity. Soon, Sellars [30] extended Berman's solution to very large suction Reynold number by neglecting at the outset the no-slip boundary condition, hence for an inviscid fluid, and viewing the solution from a boundary layer perspective, leading to $F(y) = y$ except for the boundary layer region, which for $\mathrm{Re_w} = 100$ occupies 4.6% of the channel. This inviscid solution has been employed by McClure, Cantrell, and Hart [31] as mean flow for their analysis of the aeroacoustics of SRMs. This may be the reason why the solution proposed by Sellars is also known in literature as Hart-McClure solution (HC). Of particular interest is the work of Taylor [32], in which he proposed an inviscid rotational solution for the planar and cylindrical configurations, as limit cases of cones and wedges. With Berman's notation, in the planar case, the Taylor's solution reads $F(y) = \sin(\pi y/2)$. The cylindrical version has been spread by Culick [33], after this article the solution proposed by Taylor became the Taylor-Culick (TC) profile and it is, even now, one of the most cited models in rocket motors analysis. Further general analytical solutions have been proposed maintaining the viscosity active, but valid for a range of injection/suction Reynolds numbers larger than one [19], i.e. $|\mathrm{Re}_\mathrm{w}| > 1$. The profile proposed in [19] by Yuan matches the TC profile asymptotically as Re_w approaches $\pm\infty$. Another solution, suitable for $15 \leq \mathrm{Re}_\mathrm{w} \leq 35$, expanded in power series was proposed by Terrill [34] but then abandoned because of the difficulty involved in evaluating the constants appearing in his formula. For both small [35] and large [36] Reynolds numbers, series solutions have been proposed in the case of different injection velocities from the two walls of the channel.

Similarly, starting from Taylor [32] that dealt with both planar and cylindrical configurations, almost the same theory of the wall-injected flow between two parallel flat plates has been developed for the cylindrical configuration [37, 38, 39, 40, 41]. Together with the analytical effort, experimental verifications were conducted during those years. Two pioneering experimental works were conducted by Mickley et al. [42] and Wageman and Guevara [43], respectively for the planar and cylindrical case. The first one was was criticized by Mickley and Davis [44] who reported unsuspected errors due to mechanical difficulties with the apparatus and therefore further experimental investigations have been conducted in order to produce a satisfactory collection of data, in particular with the “Stanford heat and mass transfer apparatus” [45, 20]. The second one simulates a cylindrical configuration without head-wall injection but it looks like a preliminary work, in fact it is believed that the first experimental attempt to verify most of the analytical profiles cited above were carried out by Bundy and Weissberg [46] in 1970, nearly a decade later the analytical solution proposed by Berman. Furthermore, it should be noted that, for most of the applications and theoretical works cited above the presence of a head-wall free-stream is preponderant. In fact, all the experimental set-ups cited until now, along with [47, 48, 49], but with the exception of [43], took into account a primary flow with respect to the injected one.

Just to give an idea of how one of the experimental apparatuses cited above is made, here a brief description of the “Stanford heat and mass transfer apparatus” is presented: its test section consists of two fixed side walls, an adjustable top cover, and the test plate which forms the bottom surface. Beneath the bottom surface, which is actually an assembly of twenty-four segments forming a porous plate of 2.4 m, there is a system of heating and injection. The test section is located within a primary duct, which provide a free-stream of $13\,\mathrm{m\,s^{-1}}$.

While in transpiration cooling and boundary layer control applications the main attention is on the temperature distribution, heat transfer coefficients and skin-friction, [50, 51, 52, 53] to name a few, in propulsive applications involving solid motors one of the primary concern for the scientists is the stability of the whole chamber flow-field [54]. In order to study stability, the traditional strategy is to decompose the instantaneous flow-field into a steady flow and a fluctuating term [55, 56, 57]. The steady part is actually the mean flow that corresponds to the steady-state solution of some approximation of the Navier-Stokes equations. The unsteady part, instead, is the remaining part of some expansion with respect to a small parameter, such as the Mach number or the inverse of the Reynolds number. Flandro [55] revealed the importance of the double nature of the unsteady velocity, that is the Helmholtz decomposition in a rotational and irrotational part, showing how vorticity is generated by the coupling between the steady and unsteady pressure gradients and the incoming flow from the wall [56]. This coupling between longitudinal pressure waves and the mean flow has been extensively studied [58, 59, 60, 61, 62]. Analytical expressions of these unsteady terms have been proposed [55, 56, 63] when the mean flow is the TC profile. The equations that governs these perturbations are strongly dependent on the mean flow-field, therefore it is clear the importance of its deep understanding. For the sake of generality, stability studies with a general form of the mean flow field [57] or with arbitrary time-independent wall injection velocity [64] have been conducted. Also compressibility has been taken into account by Maicke and Majdalani [65] and Maicke, Saad, and Majdalani [66], who adopted the Rayleigh-Janzen perturbation technique in order to produce a compact closed-form solution for the TC and HC mean flow-fields, respectively. Furthermore, Balakrishnan, Linan, and Williams [67] reduced the problem of compressibility to a single integral equation that must be integrated numerically.

Real solid rocket motors have expanding inner walls because of regression of the burning propellant grain, therefore the bulk motion inside the port should depend with continuity on the varying geometry. Majdalani, Vyas, and Flandro [68], introducing the expansion rate parameter and self-similarity in time and space, have found an improved mean flow profile and proved that, for slow burning propellant, inviscid solutions are practical. This technique has been extended to suction by Majdalani and Zhou [69] and Dauenhauer and Majdalani [70]. Boutros et al. [71] applied the Lie-group method in order to find the transformation that reduces the number of independent variables in the Navier-Stokes equations with boundary conditions implementing injection from expanding walls. Homotopy Analysis Method (HAM) has been used [72] to reduce the Navier-Stokes equations to a highly nonlinear ordinary differential equation but the convergence of the solution for large values of the injection Reynolds number does not give accurate results, as well as Spectral

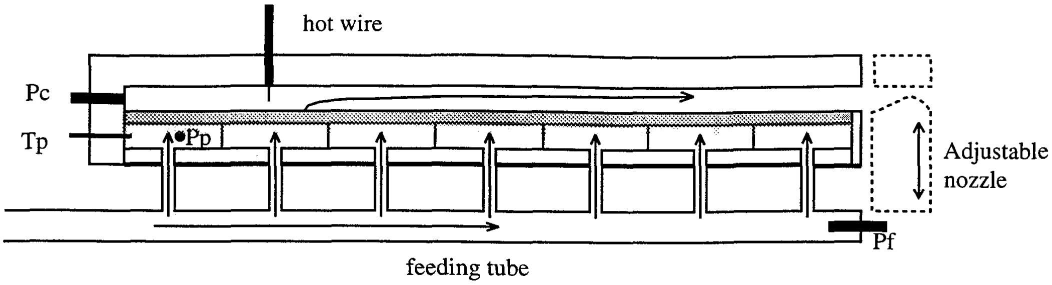

Figure 1.4. VECLA facility. Extracted from [76]

HAM (SHAM) [73]. To the best of the author's knowledge, the only purely numerical work on the simulation of the Navier-Stokes equation in a pipe with regressing wall and fluid injection from the wall itself is due to Volkov [74] but no experimental investigations have been carried out yet.

Even though several improved solutions of the mean flow field have been proposed, the Taylor-Culick profile is the most used among linear stability theories. Casalis, Avalon, and Pineau [75] proposed, in the planar configuration, three different approaches for modeling the perturbation and compared their instability results with the pressure and velocity data obtained with a facility called VECLA: a parallelepipedic channel, at the bottom of which air is injected through a porous plate, with an open exit as described in Fig. 1.4. The experimental data, reported in this work, shows that some frequencies are amplified, in accordance with the stability theory, but the mechanism that yields this instability is not explained. Avalon, Casalis, and Griffond [76], who carried out measurements on the VECLA facility too, examined the hydrodynamic instability already proved theoretically as a possible cause of the Parietal Vortex Shedding (PVS), which in turn can produce acoustic resonance, as explained in [77, 78]. Griffond, Casalis, and Pineau [79] extended the planar theory to the cylindrical case and compared their results with the experimental data published by Dunlap et al. [59], who by the way showed that the cylindrical mean flow has a non-zero swirling component later confirmed by the mean flow field proposed by Majdalani and Fist [2]. Further theoretical investigations have been conducted on the stability problem, in order to have a more complete understanding on the unstable behavior of this kind of flow. Griffond and Casalis [80], by means of the secondary instability theory, have asserted that non-linear mechanism of vortices emission is probably two-dimensional, hence it could be investigate by means of two-dimensional computations. Chedevergne, Casalis, and Féraille [81], within a linear approach, have not made any assumption on the spatial shape of the perturbation, which was instead assumed "quasi-parallel" (i.e. $q = q(r)e^{i(kx+m\theta-\omega t)}$ in the cylindrical configuration) in previous works, but have let the eigen-function be a function of the two spatial variables, so this approach is called *bi-global*. This theoretical results have been compared with the experimental data obtained with the VALDO facility. This apparatus has been thoroughly described by Cerqueira, Avalon, and Feyel [82]. Moreover, bi-global stability has been presented together with Direct Numerical Simulation (DNS) computations [83], in which an eigen-mode extracted from the bi-global stability results is superimposed to the DNS-calculated mean flow and the coupling between acoustic-mode and this hydrodynamic perturbation is analyzed. It should be remarked that other comparable strategies exist for exploring the character of oscillations in simulated SRMs. For example, Apte and Yang [84, 85, 86] introduce white noise or an acoustic excitation to perform Large Eddy Simulation (LES) calculations that can be quite effective at capturing the triggered instabilities. The unstable modes, found out with bi-global stability analysis, are globally damped in time. In fact, according to Casalis, Boyer, and Radenac [87], firings performed in basic configuration has hardly shown the appearance of thrust oscillations. They conclude that both acoustic excitation and geometric perturbations yield hydrodynamic instabilities. Furthermore, unstable modes have been recovered by decomposition of DNS simulations of a straight geometry with a localized spatial disturbance [88, 89].

It has been pointed out that geometry variations from either the straight planar channel or the straight cylinder are necessary for the onset of instabilities (if there are not external acoustic sources). Despite analytical solutions have been proposed with noncircular grain perforations [90], i.e. the cylindrical port has a non-constant radius section, when the domain geometry is not sufficiently simple, theoretical approaches becomes impracticable and numerical simulations should stand in for them. Starting from the nineties, the feasibility to use computer numerical procedures to analyze full motor stability by means of the direct full numerical simulation of the unsteady internal flow field had been demostrated [91, 92]. Lupoglazoff and Vuillot used a finite volume explicit predictor-corrector MacCormack scheme that solves the unsteady Euler [91, 92] and the Navier-Stokes [92] equations. They used two test cases geometry in which a sheared flow at a corner of the propellant grain, due to a diverging injecting wall, is present and observed nearly the same results for both inviscid and viscous simulations. Kourta [93] implemented an implicit version of the MacCormack scheme, in addition to the explicit one, and showed that it can be used for simulating unsteadiness only with low CFL numbers (≤ 50). He simulated three configurations: a rectangular chamber, the channel with a diverging wall used in [92] and a segmented configuration based on the ONERA LP3 experiment. Further geometries: LP3D and LP3E; have been simulated by Lupoglazoff and Vuillot [94], the paper [94] is a continuation of [92]. They state that PVS appears without geometrical discontinuities, but by the effect of hydrodynamic instability, spreading away from the injecting wall. Actually, the presence of a submergence region within their simulations could activate the acoustic feedback that excites the hydrodynamic instability. Lupoglazoff and Vuillot [95] analyzed how obtain instability, even with a straight geometry. They followed three attempts: forcing the injected flow at different frequencies, spatial variations of injection velocity and applying noise on the injection velocity; none of these makes the flow unstable. They speculate that there is no sufficient spatial correlation of the noise, therefore, in order to obtain and maintain the instability, a noise in the entire flow field have been applied and periodically refreshed. This is confirmed by [96] that have simulated a straight cylindrical geometry obtaining a stable solution without adding noise and coherent structures by adding white noise, furthermore these structures were found without adding noise but placing either an intersegment cavity or a submergence region. Even more realistic geometric configurations have been simulated with reduced order models [97] or fully 3D Inviscid LES (ILES) [98] simulations taking also into account the evolution of the propellant grain.

1.2 Formulation

In this section, the flow in a channel between two parallel flat walls is considered, but the axial-symmetric configuration could be presented in the same manner. Here the mathematical formulation is reported in order to have a set of equations that with results will be useful for comparisons with experimental data and numerical simulations. Consider a region bounded by two parallel walls at a distance of H, closed at one end and open at the other, with two indefinitely distant lateral walls (Fig. 1.5). The observed length of this channel is L. A right-handed coordinate system of dimensional variables, which are denoted with super-scripted letters, is placed on the line formed by the top and head walls. To facilitate the analysis, it is common practice to non-dimensionalize the variables of interest. A standard methodology is employed:

$$x = \frac{x^*}{H}, \quad y = \frac{y^*}{H}, \quad u = \frac{u^*}{v_\mathrm{w}}, \quad v = \frac{v^*}{v_\mathrm{w}}, \quad p = \frac{p^*}{p_0}, \quad \rho = \frac{\rho^*}{\rho_0} \tag{1.1}$$

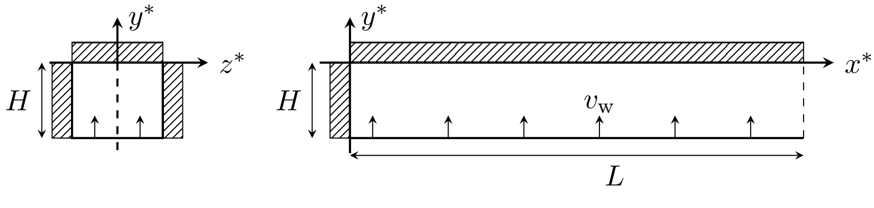

Figure 1.5. Sketch of the planar configuration and reference frame

where u and v are the velocity components, respectively in the x and y direction, v_{w} is the constant injection velocity and the subscript "0" describes a reference value at the headwall. Given this normalization, the steady Navier-Stokes equations, for a calorically perfect gas, become

$$\frac{\partial \rho u}{\partial x} + \frac{\partial \rho v}{\partial y} = 0 \tag{1.2}$$

$$\frac{\partial(\rho u u + p)}{\partial x} + \frac{\partial \rho u v}{\partial y} = \frac{1}{\mathrm{Re}_{\mathrm{w}}}\left(\frac{\partial \tau_{11}}{\partial x} + \frac{\partial \tau_{12}}{\partial y}\right) \tag{1.3}$$

$$\frac{\partial \rho u v}{\partial x} + \frac{\partial(\rho v v + p)}{\partial y} = \frac{1}{\mathrm{Re}_{\mathrm{w}}}\left(\frac{\partial \tau_{21}}{\partial x} + \frac{\partial \tau_{22}}{\partial y}\right) \tag{1.4}$$

$$\frac{\partial \rho u h}{\partial x} + \frac{\partial \rho v h}{\partial y} = \frac{1}{\mathrm{Re}_{\mathrm{w}}}\left(\frac{\partial(u\tau_{11} + v\tau_{21})}{\partial x} + \frac{\partial(u\tau_{12} + v\tau_{22})}{\partial y}\right), \tag{1.5}$$

where $h = E + p/\rho$ is the total enthalpy, $E = (u^2 + v^2)/2 + p/[\rho(\gamma - 1)]$ is the total energy and $\boldsymbol{\tau}$ is the stress tensor. Following [65], the Rayleigh-Janzen perturbation, which is a series expansion of the squared Mach number, $M_{\mathrm{w}} = v_{\mathrm{w}}/a_0$ where a_0 is the speed of sound at the origin, yields:

$$\begin{aligned} &u(x,y) = U + \mathcal{O}(M_{\mathrm{w}}^2), \quad v(x,y) = V + \mathcal{O}(M_{\mathrm{w}}^2) \\ &\rho(x,y) = 1 + \rho_1 M_w^2 + \mathcal{O}(M_{\mathrm{w}}^4), \quad p = 1 + P M_{\mathrm{w}}^2 + \mathcal{O}(M_{\mathrm{w}}^4). \end{aligned} \tag{1.6}$$

Substitution of (1.6) into (1.2) yields the following term of magnitude $\mathcal{O}(1)$:

$$\frac{\partial U}{\partial x} + \frac{\partial V}{\partial y} = 0. \tag{1.7}$$

Note that the pressure is of the order of M_{w}^2.

Irrotational solution Let be ψ the stream-function of the field of order zero, which is actually an incompressible flow, then

$$U = \frac{\partial \psi}{\partial y}, \quad V = -\frac{\partial \psi}{\partial x}. \tag{1.8}$$

The conservation of mass, implies

$$\int_{-1}^{0} \frac{\partial \psi}{\partial y}\, dy = x, \tag{1.9}$$

then $\partial\psi/\partial y$ should be a linear function of x and can be written as

$$\frac{\partial \psi}{\partial y} = x\alpha(y) + \beta(y) \implies \psi(x,y) = x\int \alpha(y)\, dy + \int \beta(y)\, dy + \gamma(x) \tag{1.10}$$

with $\alpha(y)$ and $\beta(y)$ two unknown functions such that

$$\int_{-1}^{0} \alpha(y)\,dy = 1, \tag{1.11}$$

$$\int_{-1}^{0} \beta(y)\,dy = 0. \tag{1.12}$$

The zero vorticity hypothesis can be expressed in terms of the stream-function as

$$\Omega = \Omega_z = \nabla^2\psi = 0 \tag{1.13}$$

and, thanks to (1.10), yields

$$0 \equiv \frac{\partial^2\psi}{\partial x^2} + \frac{\partial^2\psi}{\partial y^2} = \gamma''(x) + x\alpha'(y) + \beta'(y) \implies \beta'(y) = -\gamma''(0) \quad \text{for all } y.$$

Since

$$\gamma''(x) = -\frac{\partial V}{\partial x}(x,-1) = -\frac{\partial v_{\mathrm{w}}}{\partial x} \equiv 0, \tag{1.14}$$

$\beta'(y)$ equals zero for all $y \in [-1, 0]$. Furthermore, thanks to Eq. (1.12), β has zero integral, hence $\beta(y) \equiv 0$. Up to an additive constant, see Eq. (1.10) and (1.14), one can choose the stream function as[1]

$$\psi(x, y) = xF(y). \tag{1.15}$$

Thus, Equation (1.13) becomes an ordinary differential equation in F

$$xF''(y) = 0 \implies F(y) = Ay + B. \tag{1.16}$$

Now, imposing the boundary conditions of injection at $y = -1$ and impermeability at $y = 0$, which must be satisfied by the leading-order terms and read

$$V(x,-1) = -F(-1) = 1, \quad V(x,0) = -F(0) = 0 \tag{1.17}$$

yields $B = 0$ and $A = 1$; actually, we have also made an implicit assumption of zero headwall velocity in (1.9) zeroing the mass flow when x is equal to zero. Then the solution is

$$U = x \quad \text{and} \quad V = -y. \tag{1.18}$$

These are the predicted non-dimensional, velocity components of the mean flow-field for an irrotational flow, also known as HC. Note that this solution has oblique injection velocity at the wall and it is not affected by viscosity. By the way, with this

---

[1] We proved that this form of ψ is a consequence of the conservation of mass under the zero vorticity hypothesis. Without this hypothesis we are not able to prove that β is zero.

approach, we would not have satisfied the boundary conditions if we had imposed a no-slip condition at the wall $y = 0$.

Furthermore, in order to find the pressure field one has to integrate the inviscid part of the momentum equation of magnitude $\mathcal{O}(M_{\mathrm{w}}^2)$

$$\begin{aligned} -\frac{\partial P}{\partial x} &= (\boldsymbol{U} \cdot \nabla)U = x \\ -\frac{\partial P}{\partial y} &= (\boldsymbol{U} \cdot \nabla)V = y \end{aligned} \tag{1.19}$$

hence, being the partial derivatives functions of only x and y respectively, the pressure is

$$P = -\frac{1}{2}(x^2 + y^2) \tag{1.20}$$

Vortical solution Instead of assuming Eq. (1.13), consider the leading order of the vorticity equation:

$$\nabla \times (\boldsymbol{U} \times \boldsymbol{\Omega}) = \frac{1}{\mathrm{Re_w}} \nabla^2 \boldsymbol{\Omega}. \tag{1.21}$$

Now, assuming the linearity hypotesis (1.15), Eq. (1.21) becomes

$$FF''' - F'F'' = \frac{1}{\mathrm{Re_w}} F^{IV} \tag{1.22}$$

that has been proposed for the first time by Berman [29]. The inviscid version, $FF''' - F'F'' = 0$, valid for $\mathrm{Re} \to \infty$, together with the boundary conditions (1.17) and $U(x, -1) = F'(-1) = 0$, admits the non-unique solution (see Appendix A)

$$F(y) = (-1)^n \sin\left[\left(\frac{\pi}{2} + n\pi\right) y\right]. \tag{1.23}$$

The only physical solution, which gives a radial velocity vanishing only on the axis, is the case $n = 0$, the other ones are excluded being unphysical. Therefore,

$$U = \frac{\pi x}{2} \cos\left(\frac{\pi y}{2}\right) \quad \text{and} \quad V = -\sin\left(\frac{\pi y}{2}\right) \tag{1.24}$$

that is also known as TC profile.

If viscosity is retained, the fourth order equation (1.22) could be solved numerically when equipped with a further boundary condition, in this case the boundary

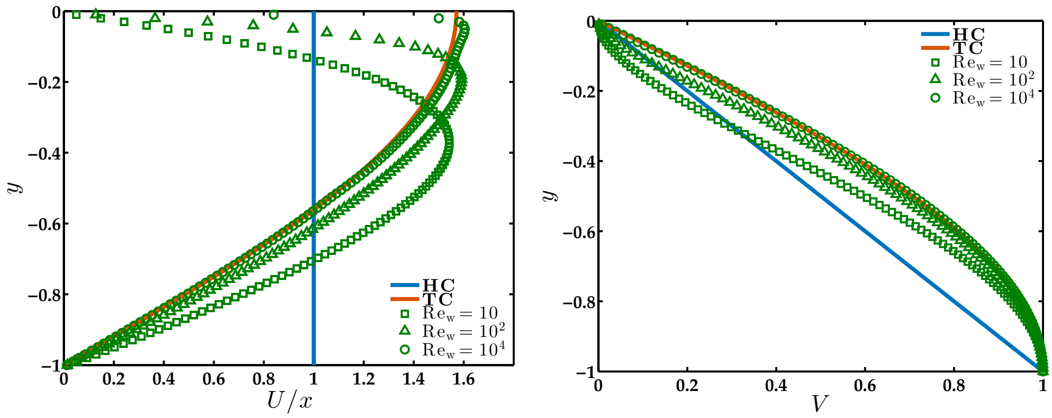

(a) **(b)**

Figure 1.6. Profiles of the x-component velocity normalized with respect to the abscissa and y-component for: Eq. (1.25) green symbols for three different Reynolds numbers, Eq. (1.18) blue and Eq. (1.24) brown

condition used is the no-slip on the wall $y = 0$,

$$\begin{cases} FF''' - F'F'' = \mathrm{Re}_{\mathrm{inj}}^{-1} F^{IV} \\ V(x,-1) = -F(-1) = 1 \\ V(x,0) = -F(0) = 0 \\ U(x,-1) = F'(-1) = 0 \\ U(x,0) = F'(0) = 0. \end{cases} \tag{1.25}$$

In Fig. 1.6a–1.6b the profiles of U and V for the three models: (1.18), (1.24) and (1.25); have been reported. Since the x-component of HC and TC are both linear with x, this velocity component has been reported normalized with respect to the x itself. The numerical solutions of (1.25) have been obtained with a four-stage Lobatto IIIA collocation method, which provides a C^1-continuous fifth-order accurate solution, for three increasing Reynolds numbers (10, 100 and 10000) showing the convergence to the inviscid model.

For small values of $\mathrm{Re_w}$, a comparison with the results obtained following the perturbation theory adopted in [29] is useful. Eqs. (1.3)–(1.4) can be rewritten as follows

$$U\frac{\partial U}{\partial x} + V\frac{\partial U}{\partial y} = -\frac{\partial p}{\partial x} + \frac{1}{\mathrm{Re_w}}\left(\frac{\partial^2 U}{\partial x^2} + \frac{\partial^2 U}{\partial y^2}\right) \tag{1.26}$$

$$U\frac{\partial V}{\partial x} + V\frac{\partial V}{\partial y} = -\frac{\partial p}{\partial y} + \frac{1}{\mathrm{Re_w}}\left(\frac{\partial^2 V}{\partial x^2} + \frac{\partial^2 V}{\partial y^2}\right). \tag{1.27}$$

Since the primary hypothesis is alway Eq. (1.15), Eqs. (1.26)–(1.27) become

$$xF'^2 - xFF'' - \frac{1}{\mathrm{Re_w}} xF''' = -\frac{1}{\rho}\frac{\partial p}{\partial x} \tag{1.28}$$

$$FF' - \frac{1}{\mathrm{Re_w}} F'' = -\frac{1}{\rho}\frac{\partial p}{\partial y}. \tag{1.29}$$

As the right-hand side of (1.29) is a function of y only, thence by deriving with respect to x gives $\partial^2 p/\partial x \partial y = \partial^2 p/\partial y \partial x = 0$. As a consequence

$$\frac{\partial}{\partial x}\left[x\left(F'^2 - FF'' - \frac{1}{\mathrm{Re_w}} F'''\right)\right] = 0, \tag{1.30}$$

which integrated gives

$$F''' - \mathrm{Re_w}(F'^2 - FF'') = C. \tag{1.31}$$

In order to find a solution of the third order ordinary differential equation (1.31) F and C are expanded as a power series of the small parameter $R = \mathrm{Re_w}$

$$F(y) = F_0(y) + F_1(y)R + F_2(y)R^2 + \mathcal{O}(R^3) \tag{1.32}$$

$$C = C_0 + C_1 R + C_2 R^2 + \mathcal{O}(R^3). \tag{1.33}$$

If Eqs. (1.32) and (1.33) are substituted into (1.31) and powers of R are collected, then

$$\mathcal{O}(1): \qquad F_0''' = C_0 \tag{1.34}$$

$$\mathcal{O}(R): \qquad F_1''' = C_1 + F_0'^2 - F_0 F_0'' \tag{1.35}$$

$$\mathcal{O}(R^2): \qquad F_2''' = C_2 + 2F_0'F_1' - F_0F_1'' - F_1F_0''. \tag{1.36}$$

Integrating three times Eq. (1.34) yields

$$F_0 = C_0 y^3 + k_2 y^2 + k_1 y + k_0, \tag{1.37}$$

where constants are determined by the boundary conditions. If one considers the boundary conditions in Eq. (1.25) thence

$$\left.\begin{aligned} &F_0(-1) = -1 \\ &F_n(-1) = 0; \qquad n \geq 1 \end{aligned}\right\} \tag{1.38}$$

$$F_n(0) = F_n'(0) = F_n'(-1) = 0; \qquad n \geq 0. \tag{1.39}$$

and F_0 becomes

$$F_0 = -(2y^3 + 3y^2) \tag{1.40}$$

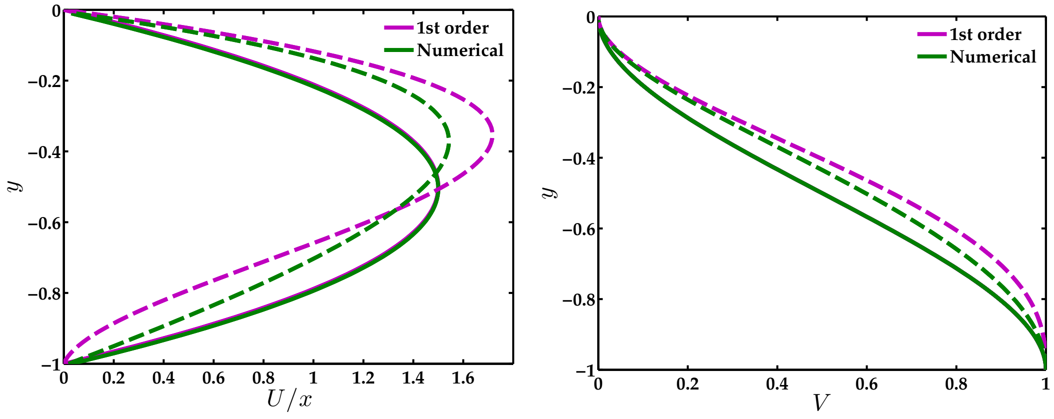

(a) **(b)**

Figure 1.7. Velocity profiles of the x-component **(a)** and y-component **(b)** for two Reynolds numbers: $\mathrm{Re_w} = 0$ solid line and $\mathrm{Re_w} = 10$ dashed line

that readily substituted into (1.36) gives the expression of the third derivatives of F_1 that, once it has been integrated three times and the constants have been found by means of Eqs. (1.38) and (1.39), yields

$$F_1 = -\frac{8}{35}y^2 - \frac{27}{70}y^3 + \frac{3}{10}y^5 + \frac{1}{5}y^6 + \frac{2}{35}y^7. \tag{1.41}$$

Eqs. (1.40) and (1.41) gives the first-order perturbation solution

$$F^{(1)}(y) = -3y^2 - 2y^3 + R\left(-\frac{8}{35}y^2 - \frac{27}{70}y^3 + \frac{3}{10}y^5 + \frac{1}{5}y^6 + \frac{2}{35}y^7\right), \tag{1.42}$$

where the superscript (1) denotes that terms of the order of R^2 have been neglected. Note that this solution has non-zero vorticity, in fact

$$\Omega^{(1)} = \nabla^2\psi^{(1)} = xF^{(1)''} = -6x(1+2y) \not\equiv 0. \tag{1.43}$$

From Eq. (1.42) one can derive the first-order expression for the velocity components:

$$\left.\begin{aligned} U &= x\left[-6y - 6y^2 + \mathrm{Re_w}\left(-\frac{16}{35}y - \frac{81}{70}y^2 + \frac{3}{2}y^4 + \frac{6}{5}y^5 + \frac{2}{5}y^6\right)\right] \\ V &= 3y^2 + 2y^3 - \mathrm{Re_w}\left(-\frac{8}{35}y^2 - \frac{27}{70}y^3 + \frac{3}{10}y^5 + \frac{1}{5}y^6 + \frac{2}{35}y^7\right), \end{aligned}\right\} \tag{1.44}$$

which are compared with the viscous numerical solution of (1.25) in Fig.1.7 for two Reynolds numbers. Note that for small Reynolds the two profiles are identical to the straight channel parabolic profile and when $\mathrm{Re_w} = 10$ the first-order solution is already inaccurate.

As for the HC profile, integrating the partial derivatives of P one obtains the pressure distribution within the channel:

$$\left.\begin{aligned} -\frac{\partial P}{\partial x} &= (\boldsymbol{U}\cdot\nabla)U = \left(\frac{\pi}{2}\right)^2 x \\ -\frac{\partial P}{\partial y} &= (\boldsymbol{U}\cdot\nabla)V = -\frac{\pi}{2}\sin\left(\frac{\pi}{2}y\right)\cos\left(\frac{\pi}{2}y\right) \end{aligned}\right\}\text{Eq. (1.24)}, \tag{1.45}$$

and

$$\left.\begin{aligned} -\frac{\partial P}{\partial x} &= x\left(F'^2 - FF'' - \frac{1}{\mathrm{Re_w}}F'''\right) = \frac{x}{\mathrm{Re_w}}C \\ -\frac{\partial P}{\partial y} &= \frac{1}{\mathrm{Re_w}}F'' - FF' \end{aligned}\right\}\text{Eq. (1.44)} \tag{1.46}$$

yield

$$P = -\left(\frac{\pi x}{2\sqrt{2}}\right)^2 - \frac{1}{2}\sin^2\left(\frac{\pi}{2}y\right), \tag{1.47}$$

for the inviscid TC, and

$$P = -\left(\frac{2}{\mathrm{Re_w}} + \frac{81}{35} + \mathcal{O}(\mathrm{Re_w})\right)x^2 - \frac{1}{\mathrm{Re_w}}F' - \frac{F^2}{2}, \tag{1.48}$$

valid for Reynolds numbers of the order of the unity. In the x-direction we have a parabolic profile due to the linear growth of velocity, which is the most evident effect (Fig. 1.8a). The three pressure fields: (1.20), (1.47) and (1.48); have different constant factors that yield, for high x-values, very different pressure levels. Despite in the y-direction the profiles are sensibly different, see Fig. 1.8b, this is perceivable only for small x where the global level of pressure is still not dominated by the x-velocity contribute.

Non-uniform injection If one considers a spatially varying time independent function $v_\mathrm{w}(x)$ as velocity injection [64], the conservation of mass (1.9) and Eq. (1.15) suggest that

$$\psi(x,y) = G(x)F(y) = \left(\int_0^x v_\mathrm{w}(\tau)\,d\tau\right)F(y). \tag{1.49}$$

This stream function must satisfy the vorticity equation, which reads

$$GG'(F'F'' - FF''') = FF'(G'G'' - GG'''), \tag{1.50}$$

where $'$ denotes the first derivative with respect to the variable on which each function depends, e.g. $G' = dG/dx$. For x and y such that F, F', G and G' are non-zero, one

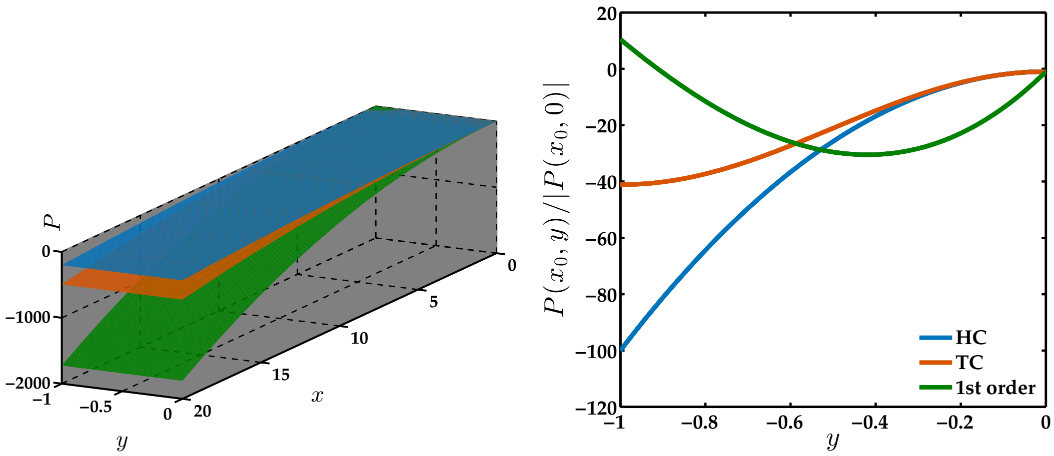

(a) **(b)**

Figure 1.8. Mean pressure distributions **(a)** and pressure profiles, normalized with respect to its value at $y = 0$, for a fixed x **(b)**; the first-order profile is obtained from (1.48) with $\mathrm{Re_w} = 1$

can separate the variables

$$\frac{F'F'' - FF'''}{FF'} = \frac{G'G'' - GG'''}{GG'} = C, \tag{1.51}$$

where C is a constant determined by the boundary conditions. Let be $F(0) = 0$, $F''(0) = 0$ and $F'(0) \neq 0$, that means $V(x,0) = 0$ and $\partial U(x,0)/\partial y = 0$, then the left-hand side of Eq. (1.51) is undetermined because of division by zero. Since, also the numerator is zero the limit for $y \to 0$ yields

$$\lim_{y\to 0} \frac{F'F'' - FF'''}{FF'} = \lim_{y\to 0} \frac{F''^2 - FF^{IV}}{F'^2 + FF''} = 0, \tag{1.52}$$

hence $C = 0$, so that Eq. (1.51) admits the TC profile as solution for F and gives the following limitation on possible profiles of injection velocity

$$\int_0^x v_\mathrm{w}(\tau)\, d\tau = \begin{cases} A\left(e^{kx} - e^{-kx}\right) \\ Ax \\ A\sin(kx), \end{cases} \tag{1.53}$$

where A and k are two arbitrary constants. Since linear combinations of the three possible solutions reported in Eq. (1.53) are also solutions, the sinusoidal one is very useful in order to model the injection as a Fourier expansion series. In fact, if the following solutions are considered: $\frac{a_0}{2}x$ and $\frac{a_n}{n}\sin(nx)$ with $a_n = \frac{1}{n}\int_{-\pi}^{\pi} f(x)\cos(nx)\, dx$ and $f(x)$ a given function; and are added together, then the

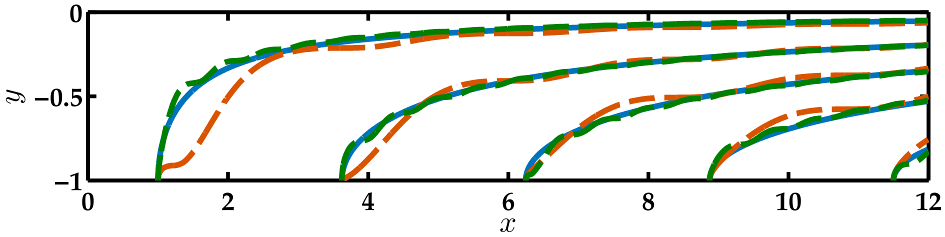

Figure 1.9. Streamlines of the two non-uniform injection flowfields yielded by $v_\mathrm{w} = 1 + \cos(k2\pi/Lx)$ (dashed): $k = 5$ (orange) and $k = 20$ (green); in comparison with the TC (solid)

injection velocity will be the Fourier series of $f(x)$

$$v_\mathrm{w}(x) = \frac{a_0}{2} + \sum_{n=1}^{\infty} a_n \cos(nx). \tag{1.54}$$

For instance, let us consider the following injection velocity $v_\mathrm{w}(x) = 1+\cos(2k\pi/Lx)$, which can be considered as a prototype of spatially varying injection. The velocity field is, therefore, given by

$$\left.\begin{aligned} U &= \left[x + \frac{L}{2k\pi}\sin\left(\frac{2k\pi}{L}x\right)\right]\frac{\pi}{2}\cos\left(\frac{\pi}{2}y\right) \\ V &= -\left[1 + \cos\left(\frac{2k\pi}{L}x\right)\right]\sin\left(\frac{\pi}{2}y\right). \end{aligned}\right\} \tag{1.55}$$

The horizontal component, U, tends to the one provided by the Taylor-Culick solution as k tends to infinity because of the presence of $1/k$ in front of the spatial varying term, while the vertical component is equal to v_w at the lower wall. Thus, the effect of a spatially varying injection is the less visible the more we are far from the injecting wall and the higher is the spatial variability, as shown in Fig. 1.9 where the streamlines for two increasing values of k are reported and compared with the Taylor-Culick field.

Compressibility effect When higher-order terms of Eq. (1.6) are retained, compressibility effects are captured. The general outline is to solve the vorticity equation first ($\sim \mathcal{O}(M_\mathrm{w}^2)$ terms), and then the momentum equation for the pressure ($\sim \mathcal{O}(M_\mathrm{w}^4)$ terms). The details given by Maicke and Majdalani [65] are not reported here, how-

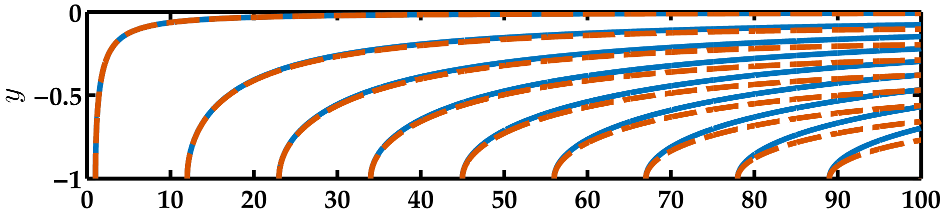

(a) $M_\mathrm{w} = 0.01$

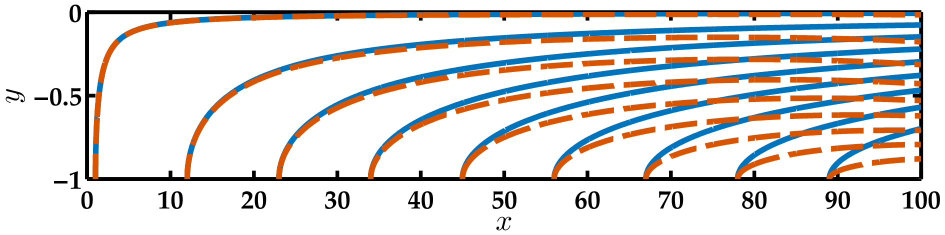

(b) $M_\mathrm{w} = 0.015$

Figure 1.10. Streamlines of the TC profile (solid) and compressible corrections (dashed)

ever the analytical expression of the mean flow affected by compressibility is

$$\left.\begin{aligned} U =& \frac{\pi}{2} x \cos\left(\frac{\pi}{2} y\right) \left\{1 - \frac{M_\mathrm{w}^2}{48} \pi^2 x^2 \left[(3 + \cos(\pi y)) + 3\,(7 - \cos(\pi y))\right]\right\} + \\ & x \sin\left(\frac{\pi}{2} y\right) \left\{-\frac{M_\mathrm{w}^2}{48} \pi^2 x^2 \left[-\pi \sin(\pi y) + 3\pi \sin(\pi y)\right]\right\} \\ V =& - \sin\left(\frac{\pi}{2} y\right) \left\{1 - \frac{M_\mathrm{w}^2}{48} \pi^2 x^2 \left[(3 + \cos(\pi y)) + 3\,(7 - \cos(\pi y))\right]\right\} - \\ & x \sin\left(\frac{\pi}{2} y\right) \left\{-\frac{M_\mathrm{w}^2}{24} \pi^2 x \left[(3 + \cos(\pi y)) + 3\,(7 - \cos(\pi y))\right]\right\}. \end{aligned}\right\} \tag{1.56}$$

In Fig. 1.10 the streamlines of the TC solution are compared with the one relative to Eq. (1.56). When compressibility effects are accounted for, the streamlines turn more rapidly, thus generating a steeper profile. As the injection velocity is increased, the behavior becomes more pronounced, and deviations from the incompressible condition are observed earlier in the flow. The effect of compressibility is negligible near the wall and becomes more evident as the fluid travels toward the end and increases in speed. However, for channels with an aspect ratio $L/H < 40$ and $M_\mathrm{w} < 10^{-2}$, the magnification of the velocity via compressibility is not appreciable.

Chapter 2

Experimental data

2.1 Particle Image Velocimetry

In this section a brief description of the experimental technique adopted in the present work is given. This technique is the Particle Image Velocimetry (PIV), hence the reader who already is expert in PIV measurements can skip to the next section. The basic principle of this technique is extremely simple: an identifiable object immersed into the fluid reveals the motion of the fluid itself. During the past two decades, the scientific and technical progress achieved in optics, lasers, electronics, video and computer techniques was necessary to develop a technique for quantitative measurements that in its early stages was only qualitative.

The experimental setup of a PIV system typically consists of several subsystems. Tracer particles have to be added to the flow and have to be illuminated in a plane (or volume for three-dimensional measurements) at least twice within a short time interval. The displacement of the particle images between the light pulses has to be determined through evaluation of the PIV recordings. Fig. 2.1 briefly sketches a typical setup for PIV recording in a wind tunnel. Small tracer particles are added to the flow. A plane (light sheet) within the flow is illuminated twice by means of a laser (the time delay between pulses depending on the mean flow velocity and the magnification at imaging). It is assumed that the tracer particles move with local flow velocity between the two illuminations. The light scattered by the tracer particles is recorded on special cross-correlation digital cameras. The output of the digital sensor is transferred to the memory of a computer and then analyzed by means of statistical algorithms that yield the velocity flow-field.

The PIV technique, in contrast to those techniques employing probes such as hot-wire anemometry, being an optical method provides a non-intrusive velocity measurement. However, it is an indirect measurements because it is based on the velocity of tracers particles that we assume to follow the fluid. PIV is a technique

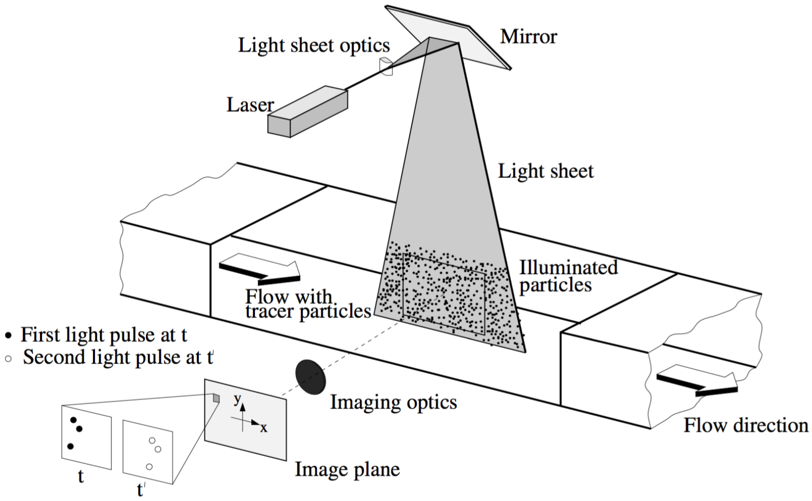

Figure 2.1. Experimental arrangement for PIV in a wind tunnel. Extracted from [99]

which allows to record images of large portion of flow-fields and hence to extract the velocity information out of these images. All other techniques, instead, only allow the measurement of the velocity of the flow at a single point, however in most cases with a high temporal resolution. The temporal resolution of the PIV is limited to the operative frequencies of lasers and camera. Since a high power light source is required to well expose the tiny tracer particles, the typical frequencies of pulsed laser are low. Therefore, researchers are developing particles capable to scatter lower intensity light and hence higher repetition pulses [100]. As already mentioned, PIV is an indirect measurements, therefore fluid mechanical properties of the particles have to be taken into account in order to avoid significant discrepancies between fluid and particle motion [99]. Another important aspect is the light-scattering properties of the tracer particles and how they are generated. However, this goes beyond the interest of this section and will not be discussed here.

2.1.1 Window cross-Correlation

The digital sensor produces a matrix of pixels in which a number between 0 and 255 (8-bit system) indicates the gray level of the image, 0 is black and 255 is white. In order to compute the motion of the fluid each image is divided into square *interrogation windows*, IW, and the cross-correlation function

$$R_{ij}(r_1, r_2) = \iint F_i(x, y) F_j(x + r_1, y + r_2)\, dx dy, \tag{2.1}$$

between two images i and j is calculated, where $F_i(x, y)$ is the intensity function of the i-th image and (x, y) is the pixel position within IW. The integral in Eq. (2.1) is computed over a deformation of IW. If there is a mean displacement of the particles inside IW of Δx_0 and Δy_0, then R_{ij} will show a peak at $(\Delta x_0, \Delta y_0)$ in the (r_1, r_2)-plane.

For each interrogation area we will obtain a mean displacement and hence a global velocity field. The resolution of this technique depends on the number of interrogation windows and, despite it can be increased by overlapping IWs, it is always of the order of the size of the window. Moreover, each interrogation window has to contain a sufficient number of particles, hence it cannot be too small.

2.1.2 Single Pixel Ensemble Correlation

In order to increase the resolution it is not possible to compute the instantaneous displacement based on single particles because there will always be an empty space with no particle inside. Therefore, rather than the instantaneous correlation function, the average of all the correlation function is take into account. This technique was introduced by Westerweel, Geelhoed, and Lindken [101], while a detailed formulation is due to Scharnowski, Hain, and Kähler [102]. Let be N_p the number of couples of images and denote with A the first image and with B the second one. The correlation function can be written as

$$C(\xi, \psi, x, y) = \sum_{n=1}^{N_p} \frac{\left[A_n(x,y) - \bar{A}(x,y)\right]\left[B_n(x+\xi, y+\psi) - \bar{B}(x+\xi, y+\psi)\right]}{\sigma_A(x,y)\sigma_B(x+\xi, y+\psi)} \tag{2.2}$$

with $\bar{A}$ the mean image and σ_A the root mean square of the sequence $\{A_n\}$. Since the correlation function has the following analytical expression

$$\begin{aligned} C(\xi, \psi, x, y) \sim \exp \Bigg[&- \left(\frac{\cos\phi(\xi - \Delta x) - \sin\phi(\psi - \Delta y)}{C_x} \right)^2 8 \\ &- \left(\frac{\sin\phi(\xi - \Delta x) + \cos\phi(\psi - \Delta y)}{C_y} \right)^2 8 \Bigg] \end{aligned} \tag{2.3}$$

where C_x, C_y and ϕ are functions of x and y, it is possible to compute the displacement Δx and Δy for each individual pixel. Also the Reynolds stresses can be estimated with these relations [102].

2.2 Experimental equipment

In order to reproduce the planar configurations presented in Section 1.2, a modular chamber has been developed. It consists of five slabs of acrylic glass, which allow optical access, and one of Aluminum at which four inlets are mounted. Once the chamber is assembled, these inlets fed the chamber with premixed air and oil droplets that work as seeding particles for the Particle Image Velocimetry. The mixture is generated by a Laskin nozzle, which produces oil droplets with diameters between 1 µm to 5 µm (estimated with wind-tunnel measurements), and contains approximately 0.18 particles per pixel. The feeding system can be summarized as follows: **air compressor** → **Laskin nozzle** → **four inlets** → **test section**. In order to split the flow coming from the Laskin nozzle into four inlets we used three bifurcations. We are able to measure the pressure upstream the Laskin nozzle and the flow–rate downstream. In order to produce droplets with diameters from 1 µm through 5 µm a pressure around 1 bar is required yielding a flow-rate of approximately $1 \times 10^{-3}\,\mathrm{m^3/s}$. Fig. 2.2 shows how the chamber is assembled in its two versions: one straight and another with a cavity of variable length. The size of the cavity is given by the position of the movable block. The chamber is divided into the actual test section and a pre–chamber by a porous plate made of Polyethylene. The top cap can be removed in order to analyze the inlet free flow going out straight from the porous plate.

PIV measurements have been conducted with the equipment specified in the following and sketched in Fig. 2.3, together with the feeding system. A **pco.pixelfly usb** CCD sensor camera with a sensor size of 1392 × 1040 pixels and an interframing time of 1 µs is triggered by a **BNC Pulse/Delay Generator – Model 575** with a frequency of 5 Hz. At the same time the Pulse/Delay Generator activates two laser beams, which are generated by a **Quantel Twins BSL double pulsed Nd:YAG Q-switched laser**, as in the scheme in Fig. 2.4. The light pulse, which determines the actual time at which an image is taken, is generated by means of the Q-switching technique therefore there are two times, say $t_1 < t_2$, such that the pulse appears at t_2 and the intensity peak decays as $L = t_2 - t_1$ grows. Two light pulses are generated

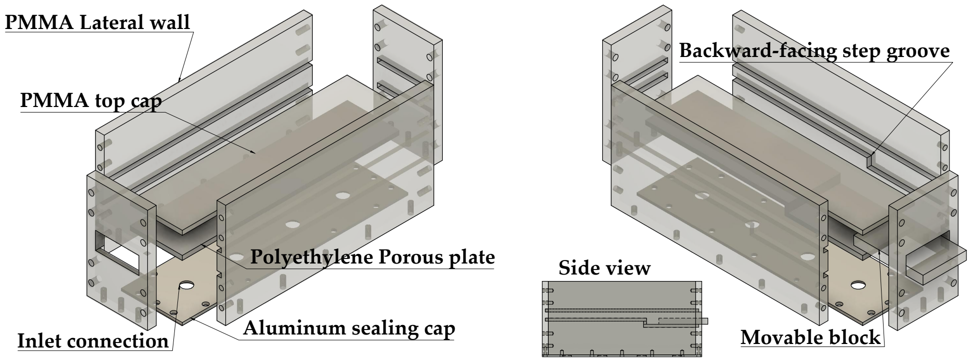

(a) straight **(b)** cavity

Figure 2.2. Exploded sketches of the two versions of the test chamber

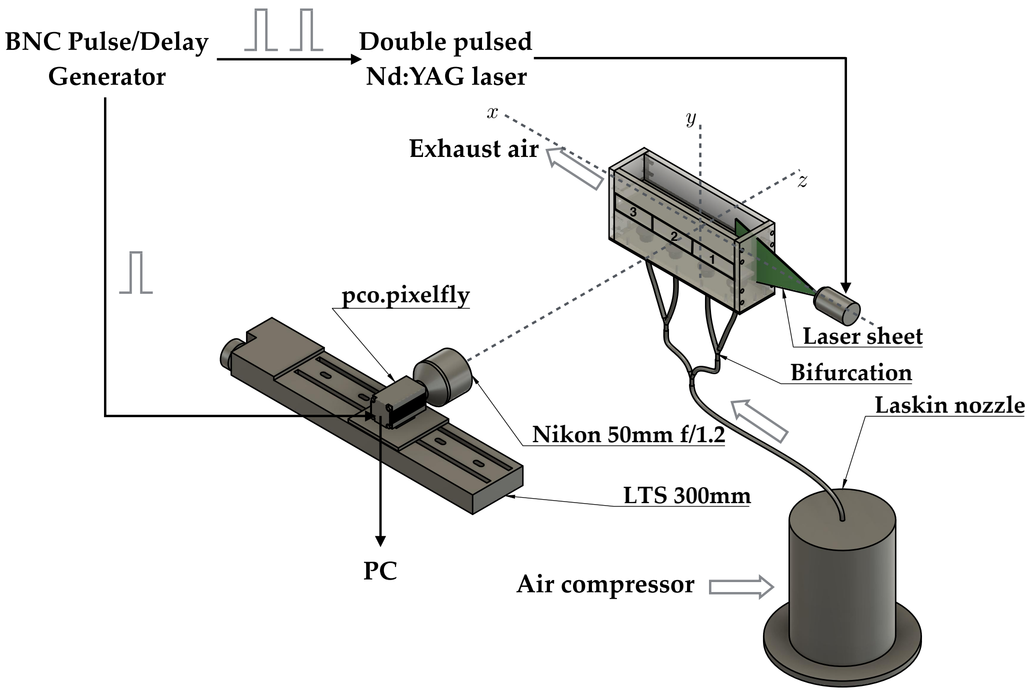

Figure 2.3. Scheme of the experimental setup

T_{tr}	T_{exp}	T_1	T_2	Δt
2000	1500	2860	3860	1000

Table 2.1. Typical values of the synchronization times in µs

with a repetition rate of 5 Hz, spaced by a time Δt in order to acquire two images. Hence, the time interval Δt determines the range of displacement of the particles form the first image, frame A, to the second image, frame B, of each couple. Since the two light pulses have to fall into the frame A and frame B respectively, there is a constraint on the triggering time, the exposure time and the two light pulses. Let T_1, T_2, T_{tr} and T_{exp} respectively the time of the first pulse, the time of the second pulse, the time at which the camera starts the first exposition and the duration of the first exposition; then

$$\begin{cases} T_{\mathrm{tr}} < T_1 < T_2 \\ T_{\mathrm{tr}} + T_{\mathrm{exp}} + 1\,\mu\mathrm{s} < T_2 < T_{\mathrm{tr}} + 1/7.3\,\mathrm{s}, \end{cases}$$

where 1 µs is the interframing time and 7.3 fps is the frame–rate of the camera. Typical values of this times are reported in Tab. 2.1. Each couple of images, which are acquired with the system described above, is stored into the PC and will be then

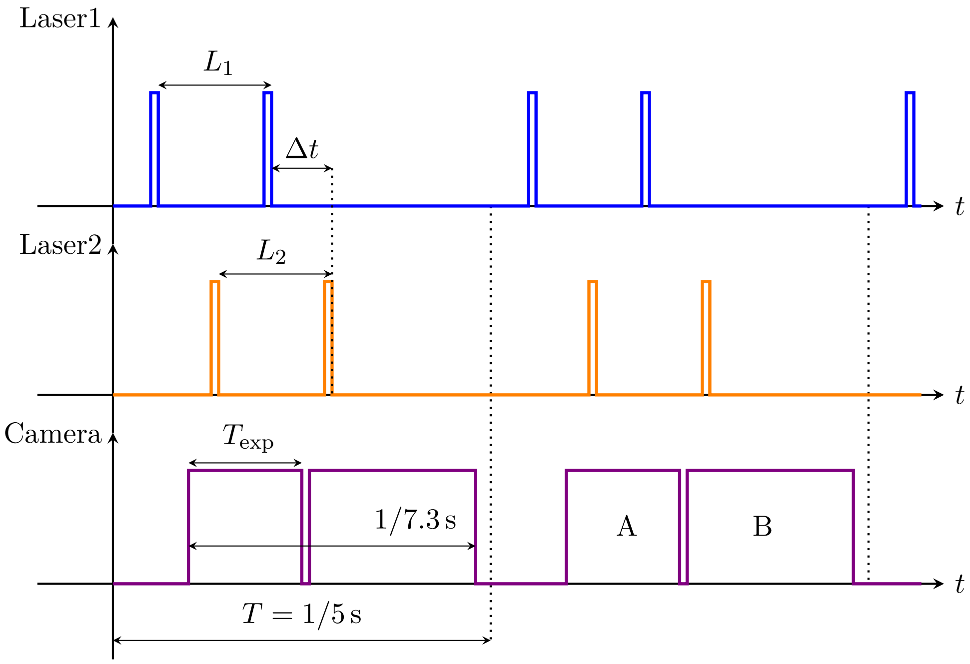

Figure 2.4. Acquisition timing scheme: the first two plots show the signal emitted by the pulse generator in order to generate light pulse by means of Q-switching, the third one represents the exposure times of the two consecutive images

pre–processed and analyzed in a second time.

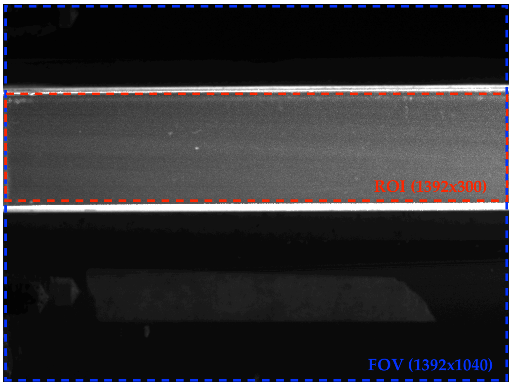

Figure 2.5. FOV vs ROI

The **pco.pixelfly** camera is equipped with a **Nikon 50 mm f/1.2** objective, which at a distance of around 50 cm enables the camera to frame a 8 cm–wide region. Since the full length of the test channel is 24 cm, in order to cover the full length, it has been necessary to place side by side three sections. Note that the region of interest (ROI) within the field of view (FOV) consists of 1392×300 pixels as shown in Fig. 2.5. Then, the pixel density is 174 pixel per centimeter. The three neighboring sections have been obtained moving the camera with the **Thorlabs Linear Translation Stage (LTS) 300mm** while the laser and the test section was fixed as in Fig. 2.3. When the cavity have been analyzed, the light source was moved on the top in order to light the hollow part of the channel, therefore the light sheet did not illuminate the full length of the channel anymore so that we fixed the camera to the axis of the laser and moved the whole chamber by means of the

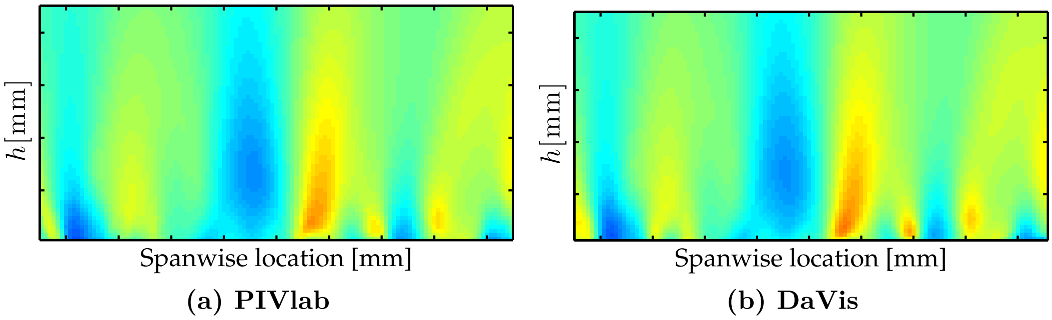

(a) PIVlab **(b) DaVis**

Figure 2.6. Comparison between the flow fields computed respectively with the open-source software **PIVlab (a)** and the commercial **DaVis (b)**

LTS. Non-perfect alignment between camera and laser sheet would lead to blurred images, non-perfect align- ment between optical system and injection direction would cause loss of tracers, yielding spurious vectors during the analysis. Therefore, orthogonality is a fundamental issue and has been ensured by the optical bench on which all the devices are fastened. As the width of the laser sheet is 1-2 mm and the dimensions of an image are 2-8 cm, the maximum angle that a velocity vector can have with respect to the (x, y)-plane is 2.8° leading to an error of $1 - \cos(2.8°) \approx 10^{-3}$ that is largely below the intrinsic error due to the PIV algorithm.

The PIV analysis have been performed with the open-source software **PIVlab** developed by Thielicke and Stamhuis [103], which is a MATLAB® App that enables multi pass using FFT window deformation analysis and adjustable overlapping between windows only at the first pass (successive passes have a 50% of overlapping). A comparison with another commercial software, **DaVis** by LaVision, showed that results were in complete agreement, see Fig. 2.6. On one hand**DaVis** offers the possibility to choose the window overlapping percentage at each pass of the analysis, in order to increase the resolution with the same amount of tracer. On the other hand, it smooths data at every pass and therefore we decided to use **PIVlab**. In order to highlight the seeding particles and to remove reflections, each sequence of images has been pre-processed applying the following filter, also known as *Minimum Subtraction*,

$$\mathrm{MS}[I^n] = I^n - \min_{k=1,\dots,N_{\mathrm{im}}} I^k,$$

where $I^n = \{I^n_{ij}$, for $i = 1, \dots, N$ and $j = 1, \dots, M\}$ is an $N \times M$ image and N_{im} is the number of images. An example is shown in Fig. 2.7. Once each sequence had been analyzed, data were smoothed by means of a robust smoothing procedure [104].

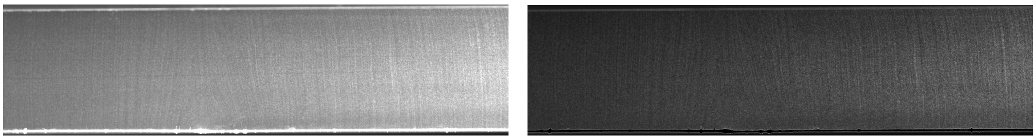

(a) original **(b)** minimum subtraction

Figure 2.7. Comparison between an original image I, **(a)**, and its transformed MS[I], **(b)**

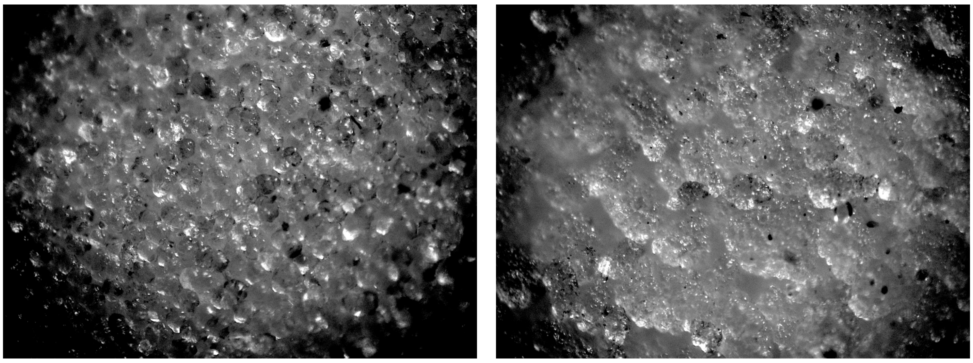

(a) Porosity: 10 µm **(b)** Porosity: 20 µm

Figure 2.8. Micro-structure of porous Polyethylene (PE)

2.3 Injection characterization

In the apparatus described above, the mixture of air and oil droplets is injected through a plate made of porous Polyethylene (Fig. 2.8), a widely used semi-crystalline polymer. Products made from standard polyethylene grades typically have pore size diameters ranging from 7 to 150 µm. Two different filtration grade have been used: 10 µm and 20 µm pore size diameters, in order to assess how the structure of the injecting material influences the injection velocity. Therefore the PMMA top cap has been removed so that the flow goes straight from the porous plate towards the aspiration hood and only one velocity component is present (actually the other one is small), the y-component with respect to the reference frame used in the previous Chapter. Since the structure of the porous material described earlier resembles the one of a fine grid, one can expect the presence of some sort of small fluid structures and therefore a measuring technique that ensures a better resolution is desirable. Thence, the standard Window cross-Correlation (WC) PIV technique has been used beside the Single Pixel Ensemble Correlation (SPEC) PIV technique [101, 102]. While the former yields a resolution proportional to the dimension of the smallest window used, e.g. if the smallest window is 16 × 16 pixels with an overlapping of eight pixels (i.e. 50 % overlapping), then the final resolution of velocity vectors is one vector per eight pixels, the latter instead gives one velocity vector per each pixel of the image. However, SPEC does not produce any instantaneous velocity field but only statistics and, moreover, it converges very slowly so a huge sample of images is necessary.

A great amount of investigations on the flow through porous screens have been concerned with the measurement of pressure drop. Another important aspect, pointed out for the first time by Morgan [105], is the pattern that the flow emerging from the plane of the screen assumes, i.e. an array of interacting jets. The first visualization of this phenomenon, then named as *coalescent jets*, is due to Bradshaw [106] that has simulated a porous material with a row of parallel cylinders in which, by means of smoke, observed about nine jets rapidly coalesce into about three groups. He asserts that this mechanism is at the basis of the instability of screens with an open-area ratio lower than 0.57, where the open-area ratio is hole-area/total-area. This is confirmed by the finding that screens with an open-area ratio greater than 0.57 do not produce shear-stress variations. When porous materials are adopted, as in the present work, the hole-area is not directly available. However, the structure of a Polyethylene plate shown in Fig. 2.8 exhibits several homogeneous spheres, therefore the open-area should corresponds to the empty space between these spheres. Let be d_{s} the diameter of one sphere and $L \times H$ the sample dimensions, then a two-dimensional array of spheres occupies a percentage of the total area equal to $\frac{H-d}{H}\frac{\pi}{2\sqrt{3}} \to 0.9$ as H tends to infinity[1], which is independent on the diameter. Therefore, the open-area ratio is 0.1 and does not depend on the porosity. Note that this approximate model of flanked spheres overestimates the nominal porosity, in fact the biggest sphere able to pass through the empty space between three sphere has radius equal to $(\sqrt{3}/2 - \frac{1}{2}\tan(\pi/6) - 1/2)d_{\mathrm{s}}$ that with $d_{\mathrm{s}} = 0.2\,\mathrm{mm}$, i.e. the average diameter of a sphere computed from Fig. 2.8b, yields a porosity of around $30\,\mu\mathrm{m}$. Hence, it is reasonable that the open-area ratio is even less than 0.1. Pimenta and Moffat [107] published the first measurements of velocity above an injected, porous plate. They used two different materials: one made of $1270\,\mu\mathrm{m}$-diameter particles, the other, made of $127\,\mu\mathrm{m}$-diamater spheres; it should be noted that some authors use as characteristic length the grain size, whereas other studies consider the pore size or filtration grade.

Pimenta and Moffat studied several blowing rates and have found a critical velocity, $5\,\mathrm{cm\,s^{-1}}$ for the $1270\,\mu\mathrm{m}$-diameter particles material, beyond which jets coagulate. Moreover, a kind of hysteresis is shown: when the blowing rate is increased up to the critical velocity coalescence appears and persists when the blowing rate is subsequently decreased. Since the spatial fluctuations of the velocity traces in [107] are stationary in time, they have been termed by Beddini [108] as

---

[1] The factor $\frac{H-d}{H}$ takes into account the correction at the boundaries

pseudo-turbulence, in contrast with the classical temporal-fluctuating turbulence. Ramachandran, Heaman, and Smith in [109] extensively studied the blowing velocity from a porous wall, in particular: the variation of mass flow with pressure drop, the pseudo-turbulence behavior and the spatial jet characteristics. It has been shown that Pseudo-Turbulence-Intensity (PTI) increases almost linearly with the mean injection velocity for $v_\mathrm{w} < v_\mathrm{cr}$ and seems to converge towards a limit value at high injection velocities ($v_\mathrm{w} > 100\,\mathrm{cm\,s^{-1}}$). The critical velocity has been found to vary inversely as the filter rating while the PTI is directly proportional, in accordance with the findings of Pimenta and Moffat but no hysteresis has been observed.

The structure of the jet pattern is thoroughly analyzed in [109], and it has been found that for four filtering rates: 3 µm, 10 µm, 30 µm and 100 µm; the jets dimensions are independent of the pore size and the most common size is $\approx 1\,\mathrm{mm}$ as in [110]. Ramachandran, Heaman, and Smith suggests that this dimension, $d = 1\,\mathrm{mm}$, can be adopted as the length scale for jetting phenomenon from porous plates. In fact, the Reynolds number based on the average injection velocity ($6.9\,\mathrm{cm\,s^{-1}}$) is 0.04 using the pore size ($d = 10\,\mathrm{\mu m}$) as length scale, a similar value to the one adopted herein where $v_\mathrm{w} \approx 9\,\mathrm{cm\,s^{-1}}$ and $d =$ 10-20 µm. For such a low Reynolds number the Stokes flow should prevail and hence individual jets should not be observed. Nevertheless, Yeh et al. [111] asserts that the injection-induced flow exhibits laminar, transition and turbulent flow as the pore Reynolds number increases and that the flow regime strongly depends on the porous material structure. Both Ramachandran, Heaman, and Smith and Yeh et al. have shown the smearing of the lumpy velocity profile as the distance from the injecting surface increases due to the diffusion mechanism. The phenomenon thus seems to be a cascade like behavior with the gradual build up of jet strength from the merging of smaller jets. The coalescence itself is due to air entrainment in the wakes of jets and the resulting pressure differentials between jets.

2.3.1 WC and SPEC measurement

A first measurement has been carried out for the porous plate of 20 µm filtering rate, and an image resolution of 19 pixel per mm. Since the SPEC-PIV technique requires a huge sample of images, 5000 couples have been acquired but only 1000 have been used for the WC-PIV analysis. The smallest window that contained a sufficient number of particles, for the WC-PIV algorithm, was 16×16 pixel wide and, in order to increase the resolution, a 50% overlapping have been adopted, thus obtaining one velocity vector per eight pixel. Therefore the two analysis, WC and SPEC, yield grids of 37×88 and 292×697 respectively.

As stated in the previous section, the characteristic dimension of a jet emerging

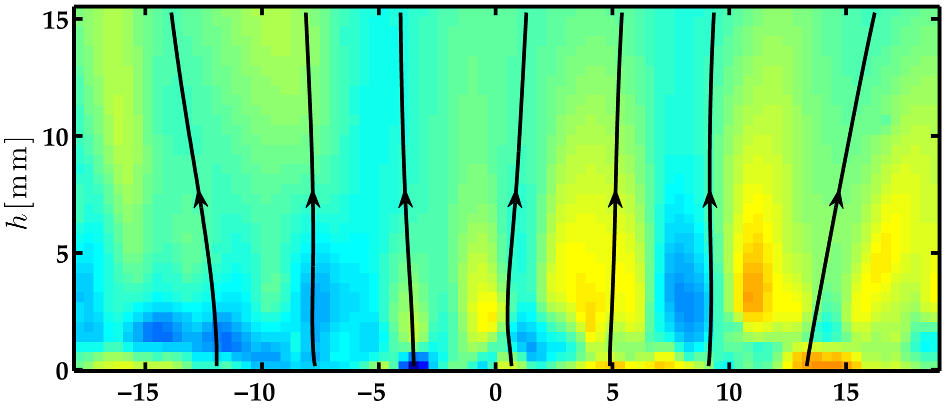

(a) WC-PIV

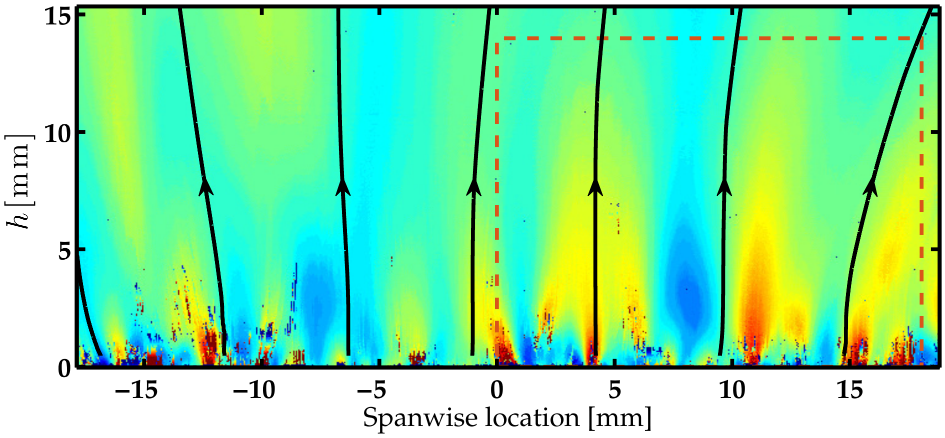

(b) SPEC-PIV

Figure 2.9. Velocity field obtained with the two techniques. The region surrounded by the dashed rectangle corresponds to the zoomed acquisition

from the porous material should be around 1 mm therefore this first measurement ensures two velocity vectors per jet. Despite a higher resolution analysis—presented hereafter—is desirable, the jet pattern is however appreciable also with this resolution (see Fig. 2.9). Once the jets pattern was observed, a second measurement with a higher image resolution, which has been obtained moving the camera closer to the test section, have been conducted. This new configuration yielded an image resolution of 52 pixel per mm and the region of interest is highlighted with the dashed rectangle in Fig. 2.9. An interesting result is that SPEC yields data with the same order of scales for both the configurations, whereas WC is comparable with the SPEC only for great distances from the injecting wall as shown in Fig. 2.10, where velocity profiles at five distances from the porous plate: $h = 8\,\mathrm{mm}$, $h = 4\,\mathrm{mm}$, $h = 2\,\mathrm{mm}$, $h = 0.5\,\mathrm{mm}$ and $h = 0.1\,\mathrm{mm}$; are reported. The following nomenclature has been adopted: WC-n stands for the Window cross-Correlation where the smallest window

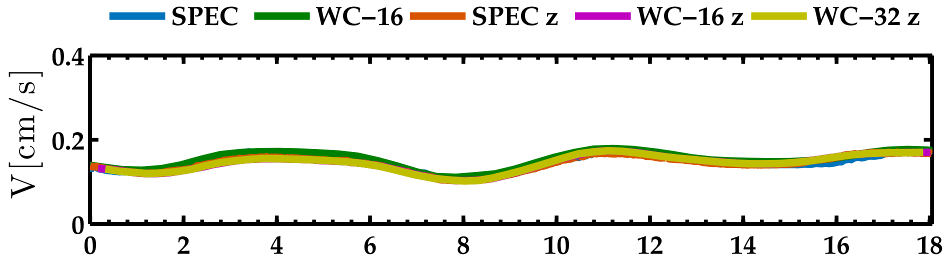

(a) $h = 8\,\mathrm{mm}$

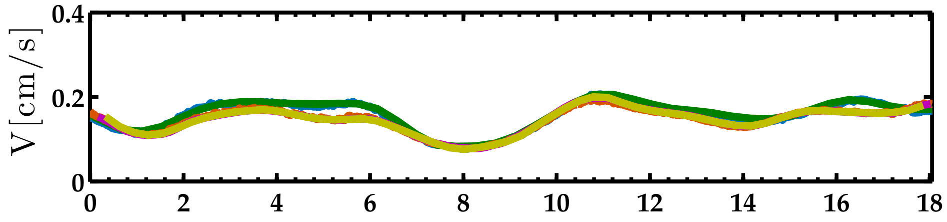

(b) $h = 4\,\mathrm{mm}$

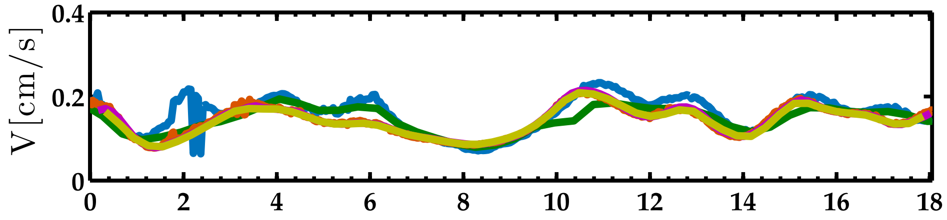

(c) $h = 2\,\mathrm{mm}$

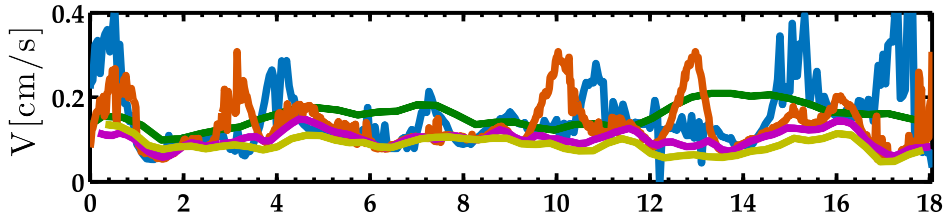

(d) $h = 0.5\,\mathrm{mm}$

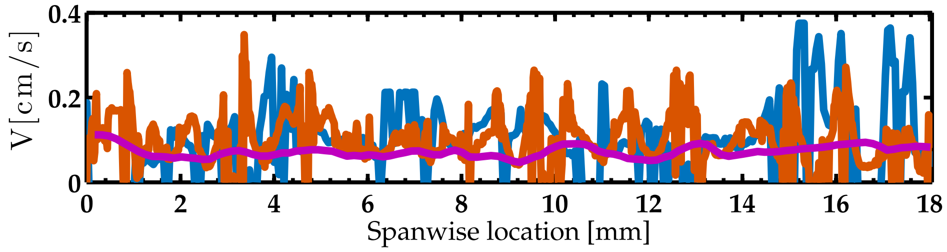

(e) $h = 0.1\,\mathrm{mm}$

Figure 2.10. Velocity profiles at several distances h from the porous plate. The "z" indicates the zoomed configuration

is $n \times n$ and the overlapping is of the 50%, the “z” means the zoomed acquisition. One should note that, due to the coarse data, “WC-16” and “WC-32 z” do not produce any velocity value at $h = 0.1\,\mathrm{mm}$ and “WC-16 z” is completely smeared even at $h = 0.5\,\mathrm{mm}$, albeit the oscillations obtained with the SPEC have a wavelength of about one millimeter and a correlation window is about $0.3\,\mathrm{mm}^2$. When the value of h does not coincide with one line of the discrete grid, but falls between two lines, the velocity profile has been linearly interpolated. Furthermore, in order to get rid of spurious values the following filter has been applied:

$$\mathcal{F}_b(v)_i = \begin{cases} v_i, & |v_i - v_{i-1}| > b \text{ and } |v_{i+1} - v_i| > b \\ \frac{v_{i+1}+v_{i-1}}{2}, & \text{otherwise} \end{cases} \tag{2.4}$$

for $i = 2, \dots, N-1$, where $v = \{v_i\}_{i=1}^N$ is the velocity profile and b is a parameter; that is every time a value v_i is out of the range of width $|v_{i+1} - v_{i-1}| + b$ with respect to the linear interpolation, $(v_{i+1} + v_{i-1})/2$, it is substituted with the linear interpolation itself.

As the two acquisitions: zoomed and non-zoomed; have been captured in two different moments, it is reasonable that the micro-structure of the jets is different as shown in Fig. 2.10e and 2.10d , due to the intrinsic random nature of a porous material, i.e. the natural arrays of micro-pores are different every time one shifts the plane of measurements. However, the two different profiles nearby the porous wall, which are qualitatively equal as will be shown in the following, produce the same velocity flow field in the farther region as shown in Fig. 2.10a and 2.10b, where the five profiles are superposed.

In order to analyze the jet structure in more detail, the two acquisitions with the two porosity rates are discussed. The higher resolution images have been used. Since the measurement technique adopted was PIV, every time a measurement has been carried out, part of the oil droplets deposits into the fibers of the porous material and gradually changes its properties. This led to a decreasing mean injection velocity during the measurements, until the porous material is replaced. The vertical velocity colormaps obtained with the SPEC and WC for both the two filtration rates are reported in Fig. 2.11, where the reader should note that the lowest velocity is equal for the two porosity and it should be correspondent to the region between two jets, while the jet cores for the 20 µm have higher centerline velocities than that relative to the smaller pore size material. In Fig. 2.11 it is clearly visible, in the regions highlighted with dashed boxes, how two jets merge together into a bigger one.

It is useful, in order to compare the four sets of data shown in Fig. 2.11, to consider normalized velocities with respect to the amplitude of oscillation of the considered profile, i.e. let $v_{\bar{h}}$ be the velocity profile at a given distance $\bar{h}$ from the plate, then

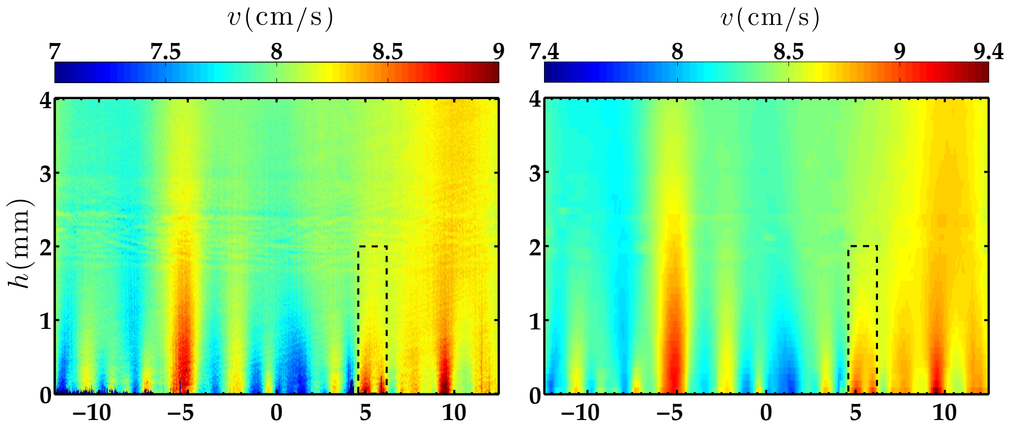

(a) SPEC 10 µm **(b)** WC-10 pixel 10 µm

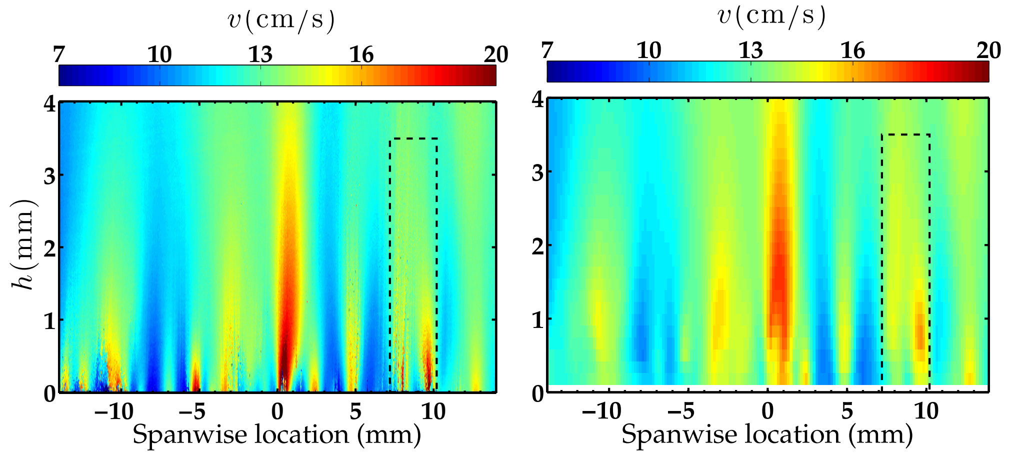

(c) SPEC 20 µm **(d)** WC-16 pixel 20 µm

Figure 2.11. Vertical velocity colormap

the normalization will be $\left(v_{\bar{h}} - \overline{v_{\bar{h}}}\right) / \left(\max v_{\bar{h}} - \min v_{\bar{h}}\right)$, where $\overline{v} = 1/(b-a)\int_a^b v\,dx$ is the mean value of v on the interval $[a, b]$. This procedure has been adopted for each h in Fig. 2.12, in which a detailed comparison of the region where the jets coalescence is more evident, i.e. the dashed rectangles, is shown. In addition, the spatial coordinates have been made dimensionless by means of the diameter, D of the big jet: $D = 1.6\,\mathrm{mm}$ for the 10 µm material and $D = 3\,\mathrm{mm}$ for the 20 µm. After normalization, the merging phenomena are directly comparable.

From the two-dimensional colormaps, only the large scale structures are distinguishable, whereas finer scales appear much clearly when profiles at given hs are taken into account. Since SPEC data shows odd-even oscillations, and this behavior could be ascribed to noise, two smoothed profiles have been computed by means of the Locally Weighted Linear Regression Method implemented into the Matlab Curve Fitting Toolbox. A first smoothing with a span of twenty-one points has been yielded,

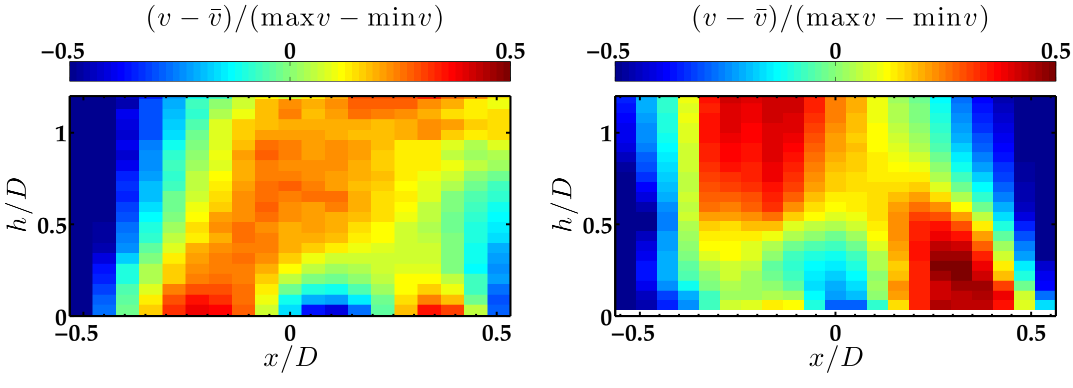

(a) WC-10 pixel 10 µm **(b)** WC-16 pixel 20 µm

Figure 2.12. Detailed view of the jets coalescence relative to Fig. 2.11

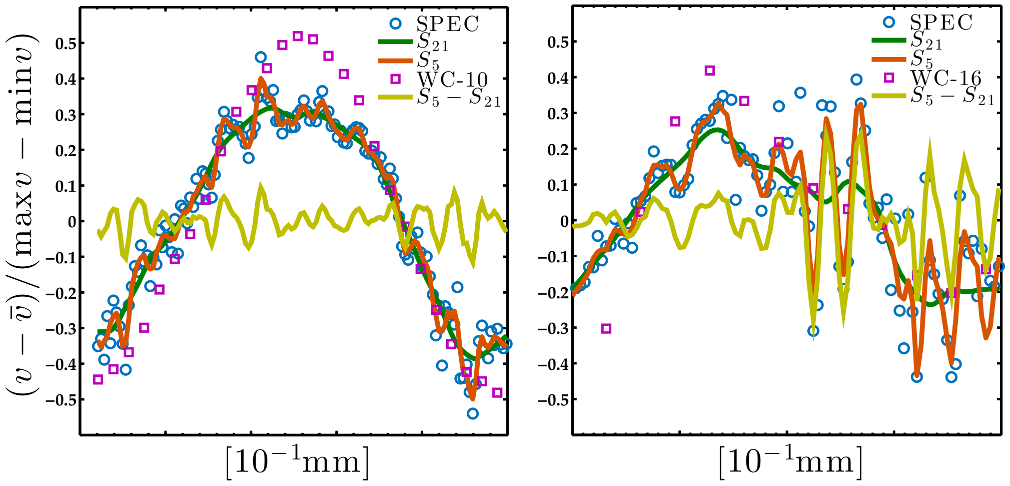

(a) 10 µm **(b)** 20 µm

Figure 2.13. Normalized velocity profiles at $h = 0.47\,\mathrm{mm}$

in order to extract the local mean profile, afterwards the span has been reduced to five points so that odd-even oscillations disappear, see Fig. 2.13a and 2.13b. Let be S_{21} the 21-points smoothed profile and S_5 the other one, then $S_5 - S_{21}$ represents the contribute of small structures to the whole profile S_5. Moreover, this structure does not change that much as reducing the distance from the plate. The profile S_5 is useful to analyze the dimensions of small jets that constitute the bigger one. In order to do that, in Fig. 2.14 the correlation function and Fourier Transform of the two S_5 profiles, respectively for the two filtration rates, are reported. Recall that

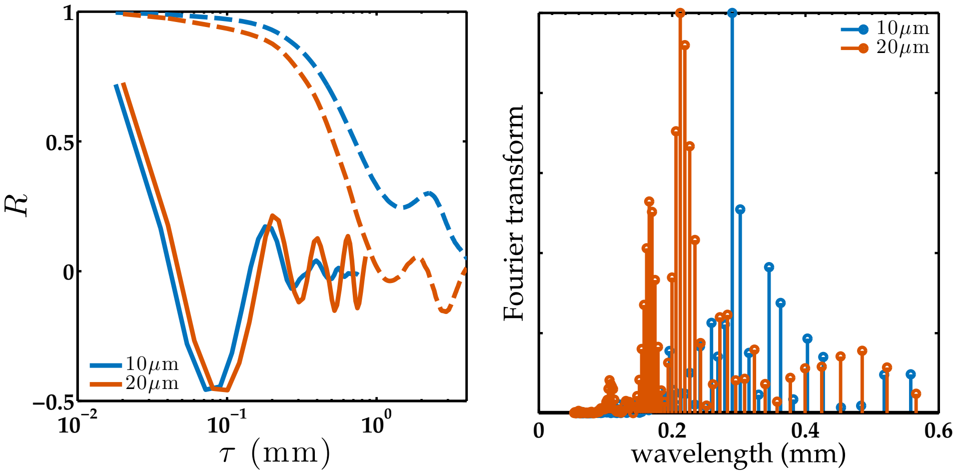

(a) Correlation **(b)** Fourier Transform

Figure 2.14. Correlation function and Fourier transform of the profiles $S_5 - S_{21}$ for the two filtration rates: 10 µm and 20 µm. Dashed lines refer to the correlation function of S_5 computed on the whole spanwise location

the correlation function is defined as follows for a discrete signal $\{v_i\}_{i=1}^{N}$

$$R_v(\tau) = \frac{1}{(N-\tau+1)\sigma_v^2} \sum_{k=1}^{N-\tau} (v_k - \bar{v})(v_{k+\tau-1} - \bar{v}), \tag{2.5}$$

where $\sigma_v = \sqrt{1/N \sum_{k=1}^{N} (v_i - \bar{v})^2}$ is the standard deviation and $\bar{v}$ is the mean of the signal. Both functions, correlation and Fourier transform, when applied to the fluctuations, indicates structures of a characteristic dimension between 0.2 mm and 0.4 mm. On the other hand, when the global profile S_5 is taken into account, the correlation function shows bigger structures with characteristic dimensions of around two millimeters for both plates and small oscillations completely disappear, likely because of their relative low intensity with respect to the large wavelength oscillations.

Since velocity profiles yielded by the SPEC technique are extremely jagged, the question if there could be a considerably contribute of noise is reasonable. Therefore a wavelet analysis have been conducted comparing the high frequency content of a velocity profile generated with the SPEC and two random signals: a white noise and a uniformly distributed process. All the three signals are normalized with respect to their mean value and standard deviation, i.e. let $v = \{v_i\}$ be a discrete signal then $(v - \bar{v})/\sigma_v$ will be its normalization. Recall that the wavelet analysis produces a set of coefficients defined as follows

$$\mathrm{WC}(s, x; v, \psi) = \int_{-\infty}^{\infty} v(t) \frac{1}{\sqrt{s}} \psi \left(\frac{t - x}{s} \right) dt, \tag{2.6}$$

where x is the spanwise variable, s a scale parameter and ψ the proper wavelet function, which in this case is the Morlet wavelet. The operator WC yields the "energy distribution", contained into the signal on which it is acting, for each dimensional scale that is directly connected to the parameter s. In order to obtain a percentage of energy the following values, strictly related to WC, will be shown

$$\mathrm{PE}(s, x; v, \psi) = 100 \times \frac{\mathrm{WC}(s, x; v, \psi)^2}{\int_a^b \int_{k=1}^{s_{\max}} \mathrm{WC}(s, x; v, \psi)\, ds\, dx}, \tag{2.7}$$

where $[a, b]$ is the spanwise extension of the signal. Small values of s are related to rapidly changing details of the signal, while high scales are related to coarse features. In Fig. 2.15, where the three signals are reported beside their PE maps, it is shown how noise spreads the energy content on a wide range of scale, while the SPEC data are more concentrated on a scale range $s \in [5, 15]$.

An interesting feature of the flowfield is its turbulent behavior. In particular, two quantities, already mentioned within the introduction of the section, should be analyzed: the Psuedo-Turbulence-Intensity and the classical Turbulence-Intensity; which are briefly recalled below. Let be $\{u_{ij}^k\}$ and $\{v_{ij}^k\}$ the two components of a velocity discrete signal, the subscript indices denote the spatial variability and the superscript, k, is the time index. Since the Turbulence-Intensity is an estimation of the time fluctuations of velocity in a given spatial point, it is defined as follows

$$\mathrm{TI}_{ij} = \frac{\sqrt{\frac{1}{N} \sum_{k=1}^{N} (u_{ij}^k - \bar{u}_{ij})^2 + (v_{ij} - \bar{v}_{ij})^2}}{\sqrt{\bar{u}_{ij}^2 + \bar{v}_{ij}^2}}, \tag{2.8}$$

where $\bar{u}_{ij} = \frac{1}{N} \sum_{k=1}^{N} u_{ij}^k$ with N the number of time instants and analogously for the other component. The Pseudo-Turbulence-Intensity is, instead, a global parameter of spatial variations for a given velocity profile at a given time, therefore the time index and the spatial index representing the distance from the porous plat drop out because they are constant,

$$\mathrm{PTI}_i^k = \frac{\sqrt{\frac{1}{n} \sum_{j=1}^{n} (u_j - \bar{u})^2 + (v_j - \bar{v})^2}}{\sqrt{\bar{u}^2 + \bar{v}^2}}, \tag{2.9}$$

where $\bar{u} = \frac{1}{n} \sum_{j=1}^{n} u_j$ with n the total number of spatial points and analogously for the other component. Essentially, TI and PTI are the same operator acting on

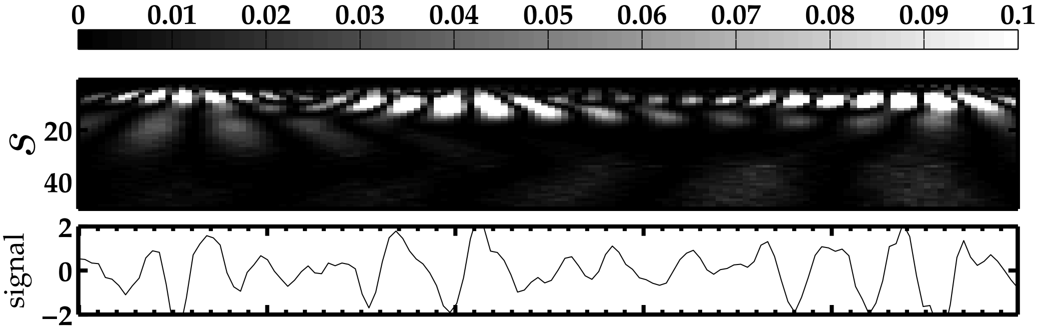

(a) $S_5 - S_{21}$

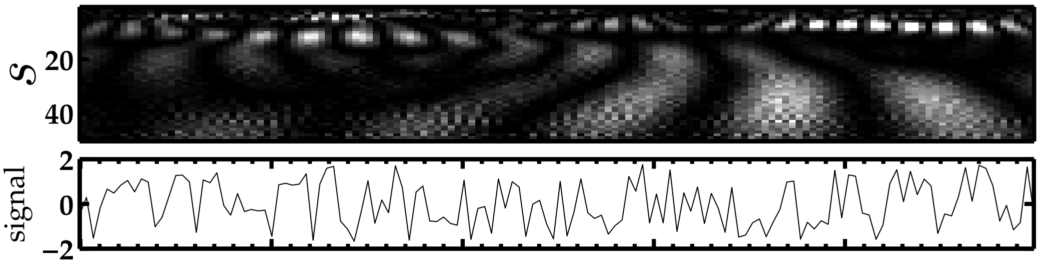

(b) Uniformly distributed random process

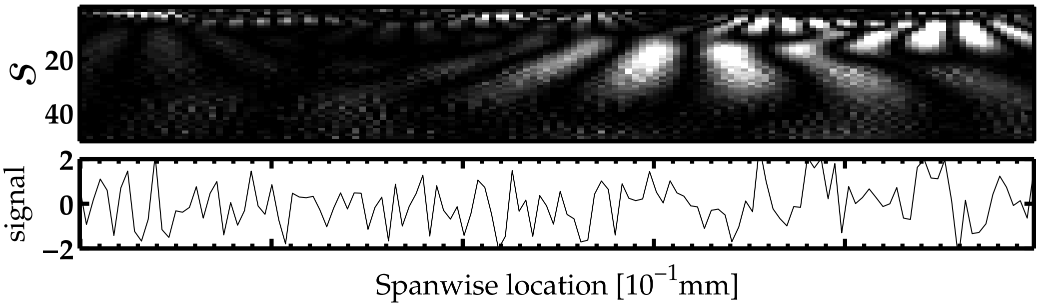

(c) White noise

Figure 2.15. Comparison of wavelet coefficients between the SPEC data **(a)** and two random processes **(b)**-**(c)**

different signals, the first one on time-series and the second one on spanwise profiles. In Fig. 2.16a the PTI variation with h is reported for the two filtration rates: 10 µm and 20 µm; note that the two filtration rates generate different levels of PTI, in particular a larger pore size yields a higher level of pseudo-turbulence-intensity, in accordance with both Pimenta and Moffat [107] and Ramachandran, Heaman, and Smith [109]. However, in both cases PTI decays as $h^{-0.4}$. Despite WC technique does not provide any additional information getting closer to the wall, SPEC shows an abrupt increasing of PTI for $h < 0.2$ mm with the 10 µm sample and $h < 0.08$ µm with the 20 µm, but there are a few data points in the latter case and maybe more accurate measurements should be carried out in order to make further conclusions.

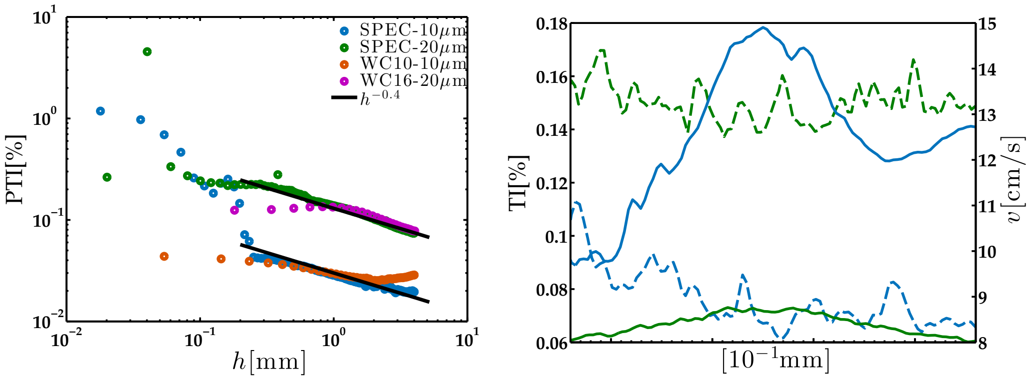

(a) **(b)**

Figure 2.16. Pseudo-turbulence-Intensity log-log variation with height from the porous plate for the two samples **(a)**; Turbulence-Intensity (dashed) and vertical velocity (solid) distributions at $h = 0.47$ mm for the two samples: 10 µm (green) and 20 µm (blue)

Turbulence-intensity, instead, shows an opposite behavior as reported in Fig 2.16b, where the TI distribution at $h = 0.47$ mm, for the two filtration rates, is compared with the vertical velocity component. In fact, the velocity profile relative to the 10 µm sample, which provides lower injection with respect to the other sample, shows an higher TI level. However, the TI level are only a small percentage of the velocity magnitude with respect to the findings of previous works [109], probably because of the small injection velocities. Moreover, it is not as easy as in [109] to find a direct correspondence between peaks of TI and valleys of velocity.

As a conclusion, although the injection velocity analyzed herein is much more lower than that produced by burning surface of a solid propellant, the statistical and topological characteristics are very similar to those obtained by numerical models of realistic propellants [112].

2.4 Closed-open camber measurement

Within this section, the experimental investigation of the two configurations sketched in Fig. 2.2 are reported. For both the geometries it has been used the 20 µm pore-size material. At first, the velocity field in the whole chamber will be analyzed for the straight configuration, afterwards the measurements of the cavity configuration flowfield will be focused on a region containing only the cavity itself.

2.4.1 Straight configuration

The flow generated from the injection into the closed-open configuration is intrinsically linked to the behavior of the injection itself. Beddini [108] found that a change

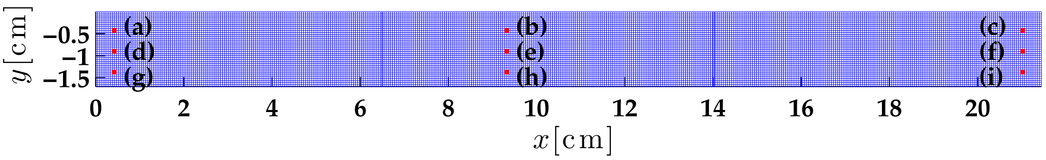

Figure 2.17. Mesh obtained with the PIV software where the nine points at which PDFs are calculated have been highlighted

in the shape of the mean velocity profile due to transition to turbulence is related either to the distance from the head end of the channel or to the pseudo-turbulence introduced by the injection. Moreover, the pseudo-turbulence level increases with increasing average injection velocity, as shown in the previous section (Fig. 2.16). This transition of the shape profile appears as a drop of the momentum-flux coefficient

$$\beta = \frac{\int_{-H}^{0} u^2 \, dy}{\left(\frac{1}{H} \int_{-H}^{0} u \, dy \right)^2 H} \tag{2.10}$$

at a given distance x or at a given $\mathrm{Re}_{\mathrm{inj}}$. Olson and Eckert [113] and Huesmann and Eckert [114], which were used as experimental references into the Beddini's work, observed a change in the shape of the horizontal velocity component for injection Reynolds numbers greater than 80 at a relative distance from the head end of 36. Within the same range of parameter, Yagodkin [115] did not observed any transition to turbulence. However, neither in [113, 114] nor in [115] the pseudo-turbulence level is mentioned. It is reasonable that into the Yagodkin's experiments the pseudo-turbulence is not high enough.

In this section, the measurements of the global velocity field inside a two-dimensional wall-injected channel is carried on. In addition, the specific pseudo-turbulence behavior is available because it has been described in Section 2.3.1 together with the injection velocity. The feeding system provides a volume flow rate of $\dot{m} = 1.117 \times 10^{-3}\,\mathrm{m}^3/\mathrm{s}$ at the feeding tube yielding an injection velocity $v_{\mathrm{w}} = \dot{m}/A = 9.30\,\mathrm{cm\,s}^{-1}$, where $A = 120\,\mathrm{cm}^2$ is the global injecting area of the porous plate. Therefore, the injection Reynolds number deriving from this estimation is $\mathrm{Re}_{\mathrm{w}} = 114$.

As already described in Section 2.2, the whole length of the channel has been covered with three partially overlapped sections. For each section, a sequence of 1000 images is analyzed with decreasing window size, i.e. from 128×128 pixels to 16×16 pixels with a 50% overlapping, thus giving a velocity vector resolution of one vector each 8 pixels, corresponding to one vector each 0.5 mm. A representation of the data grid is given in Fig. 2.17. Since the velocity magnitude increases along the distance from the head end, the acquisition of separate samples, one for each section, enables

Section	Δt [µs]	Error [mm/s]
1	3000	1.9
2	2000	2.9
3	1000	5.8

Table 2.2. Values of Δt and error on velocity for each section in the closed-open configuration

us to calibrate the time interval between two successive images, Δt, in order to optimize the local displacement in each section. The time intervals are summarized in Tab. 2.2 together with an estimation of the error computed as the equivalent velocity of a tenth of a pixel per frame. Note that if a unique measurement for the whole channel—assuming the same resolution—were conducted, in order to ensure an accurate measurement of the highest velocity, it would be necessary the smallest $\Delta t = 1000\,\mu\text{s}$ and hence also the small velocities would be affected by the greatest error.

In order to compare experimental data with analytical models, the former are made dimensionless with respect to the injection velocity. Since the v component of the experimental data shows near the injecting wall the non-uniform profile discussed in Section 2.3.1 and, in addition, being detected at a non-zero distance from the plate, then inevitably affected by the horizontal component, an indirectly estimation of v_w is preferred. Thanks to the mass conservation law between the plate, $\dot{m} = v_\text{w} L$, and the vertical line at the outlet section, $\int_{-H}^{0} u\,dy$, we have

$$v_\text{w} = \frac{1}{L}\int_{-H}^{0} u\,dy \approx 9.28\,\text{cm}\,\text{s}^{-1}. \tag{2.11}$$

Actually, due to light reflections, u is not available in a thin region near the upper and lower boundary, therefore in Eq. (2.11) the actual interval of integration is smaller than the whole height, but its contribute to the integral is negligible. From Eq. (2.11), the estimated value of v_w is $9.28\,\text{cm}\,\text{s}^{-1}$, whereas the injection velocity derived from direct measurements at the inlet tube was $9.30\,\text{cm}\,\text{s}^{-1}$. This value is very close to the one obtained by PIV data, thus the system seems to be well controlled and the input condition is fully established.

Mean values The behavior of the two velocity components in the whole chamber is reported in Fig. 2.18a and 2.18b. In the first one, it is clear as the horizontal velocity increases when moving towards the right, as a consequence of the air inlet from the bottom and of the deviation due to the upper wall. Regarding the vertical velocity components, reported in Fig. 2.18b, little structures due to the porosity of

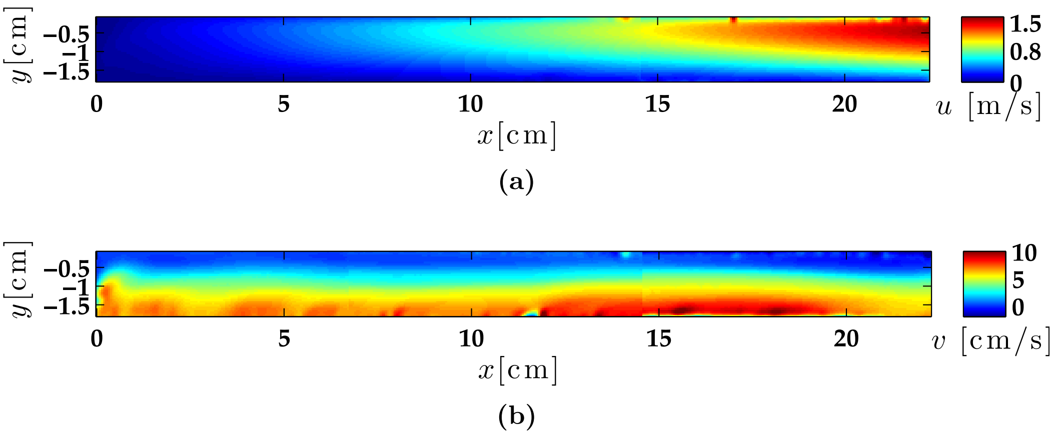

(a)

(b)

Figure 2.18. Mean velocity field in the closed-open configuration

the filter are still visible, even in this closed configuration. Note that the vertical velocity also increases when moving from left to right and that there is a lower layer in which the vertical component is predominant over the horizontal component and a upper layer where the opposite takes place. Note also that the order of magnitude is similar to the one obtained during the analysis of the inlet conditions in the previous section. We are not able to assess if the first previous observation is related to the drop of pressure, which is due to the high u velocity and hence the different pressure gradients across the filter experienced by the flow, or it is a consequence of the development of hydrodynamic instability as described in [81].

Once data are made dimensionless[2] with respect to v_w, which is equal approximately to $0.09\,\mathrm{m\,s^{-1}}$, we can compare them with the analytical models described in Section 1.2. In particular, with the TC's profile (1.24) and the numerical solution of (1.25) obtained with $\mathrm{Re}_\mathrm{inj} = 114$. In Fig. 2.19 we have reported some profiles of velocity at several x positions (blue lines): in Fig. 2.19a the horizontal component has been scaled with respect to $\max_y u$ so that we can also compare the turbulent profile proposed in [108], i.e. $u = (y+1)^{0.25}$, while in Fig. 2.19b the vertical component v is depicted. From Fig. 2.19a it is clearly visible how the measured horizontal velocity profiles approach the viscous numerical solution much better than the inviscid ones. Indeed, as the Reynolds number is low, the no-slip boundary condition at the upper wall is not negligible and a thick boundary layer is obtained. This means that in such kind of flow configurations, the effect of viscosity cannot be neglected due to the presence of the upper wall. As in Yagodkin's measurements, the present mean velocity profile does not seems to experience any transition to the turbulent shape, observed instead by Huesmann and Eckert and Olson and Eckert

---

[2] Also the error should be scaled by v_w. Then we obtain a maximum error, the one relative to the third section, of the order of 0.06.

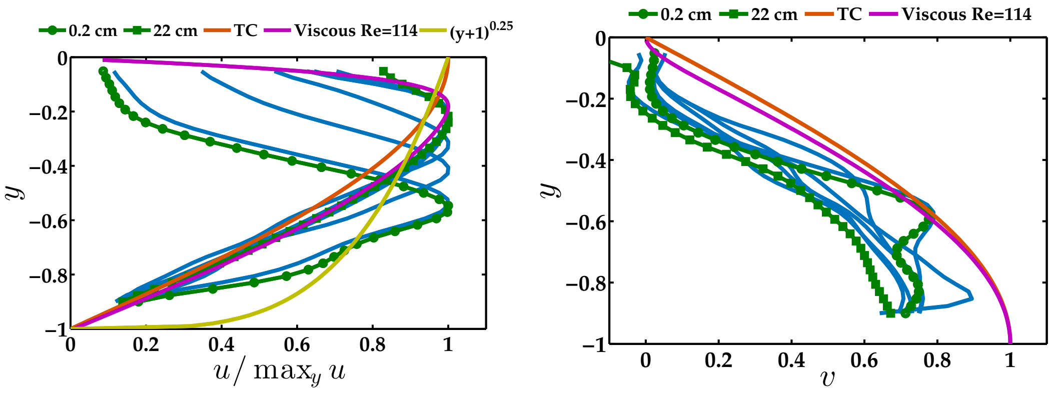

(a) (b)

Figure 2.19. Profiles of mean non-dimensional velocity at several positions along x-axis. Blue lines are the velocity profiles between the two green edges

at the present Reynolds number. A possible explanation can reside in the level of pseudo-turbulence injected from the porous wall and the relative length of the channel. In fact, Beddini's calculations with relative rms turbulence intensitites ranging up to 25% and zero PTI show transition beyond $x = 36$, while surface-generated pseudo-turbulence between 0.035 and 0.078 seems to activate the transition. Herein, instead, the pseudo-turbulence at the surface is around 0.003 and the relative length of the channel is 12.

Fluctuations Let us indicate for brevity the two normal Reynolds stresses as $\langle u'u'\rangle$ and $\langle v'v'\rangle$, where the operator $\langle \phi\psi\rangle$ applied to two signals $\phi = \{\phi_{ij}^n\}$ and $\psi = \{\psi_{ij}^n\}$, with subscripts denoting space variability and superscripts denoting time, is a temporal average

$$\langle \phi\psi\rangle = \frac{1}{N}\sum_{n=1}^{N} \phi_{ij}^n \psi_{ij}^n, \tag{2.12}$$

while $\phi' = \{\phi_{ij}^n - \bar{\phi}_{ij}\}$ with $\bar{\phi}$ the mean field. Therefore, the standard deviations $\sigma_u = \sqrt{\langle u'u'\rangle}$ and $\sigma_v = \sqrt{\langle v'v'\rangle}$, which are the square root of the normal Reynolds stresses, are a statistical indication of how much each component of velocity fluctuates with respect to the mean value. Here, fluctuations of the order of millimeters per second for the velocity component u and tenths of a millimeter per second for the v have been obtained, as reported in Fig. 2.20.

The amplitude of fluctuations in both directions increases when moving towards the right part of the field, i.e. the outlet section. This means that the mean flow configuration reported in Fig. 2.18 should fluctuate or vertically (flapping) or horizontally (pressure waves) or both. It is important to understand whether these fluctuations are related to vortices generated close to the plate and then

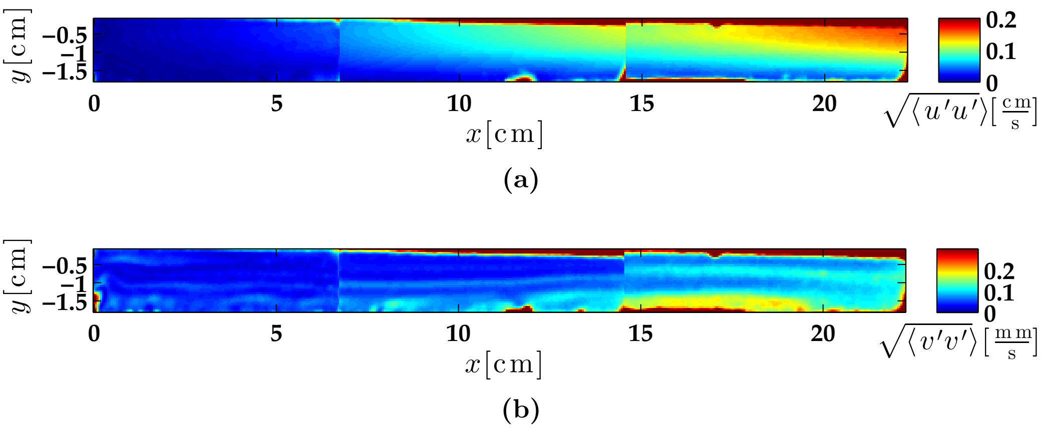

Figure 2.20. Standard deviations of u', (a), and v', (b)

convected towards the outlet. To this end, the detection of the mean vorticity field and of instantaneous flow structures is performed. In the mean vorticity field, reported in Fig. 2.21b, and furthermore in the Ω/x field reported in Fig. 2.21c, a spatially oscillating pattern, as an array of crossflow jets, due to the jet-like structures generated by the porous plate is clearly visible. These structures are bigger than the single jets observed earlier, as they merge together when they are bended by the horizontal flow. They also become narrower as we go far from the head end of the rectangular cylinder.

It is plausible that the relatively high amplitude oscillations of u are related to these large scale structures rather than to the small vortical ones reported in Fig. 2.22. These small structures have been detected with the Δ-criterion

$$\Delta = P^2 - 4Q < 0, \tag{2.13}$$

where

$$P = \frac{\partial u}{\partial x} + \frac{\partial v}{\partial y} \quad \text{and} \quad Q = \frac{\partial u}{\partial x}\frac{\partial v}{\partial y} - \frac{\partial u}{\partial y}\frac{\partial v}{\partial x}$$

as prescribed by Jeong and Hussain [116]. Looking at Fig. 2.22, it is clear that vortical structures are mainly generated at the lower porous plate, presumably due to the jet-like structures interactions. These vortices grow in number, size and intensity when moving towards the right outlet part and contribute to the increasing of fluctuations levels on the outlet part of the chamber.

In order to establish whether flow transition to turbulence appears, Yamada and Ishikawa [117] analyzed the turbulence intensity peak, i.e. $I_\mathrm{p} = \max_y \mathrm{TI}$ where the turbulence-intensity is relative to the given horizontal velocity profile that is $\mathrm{TI} = \sqrt{\langle u'u'\rangle + \langle v'v'\rangle} / \max_y \bar{u}$, and found that transitional regions are characterized by a bump in the TI profile nearby the injecting surface. Since they adopted

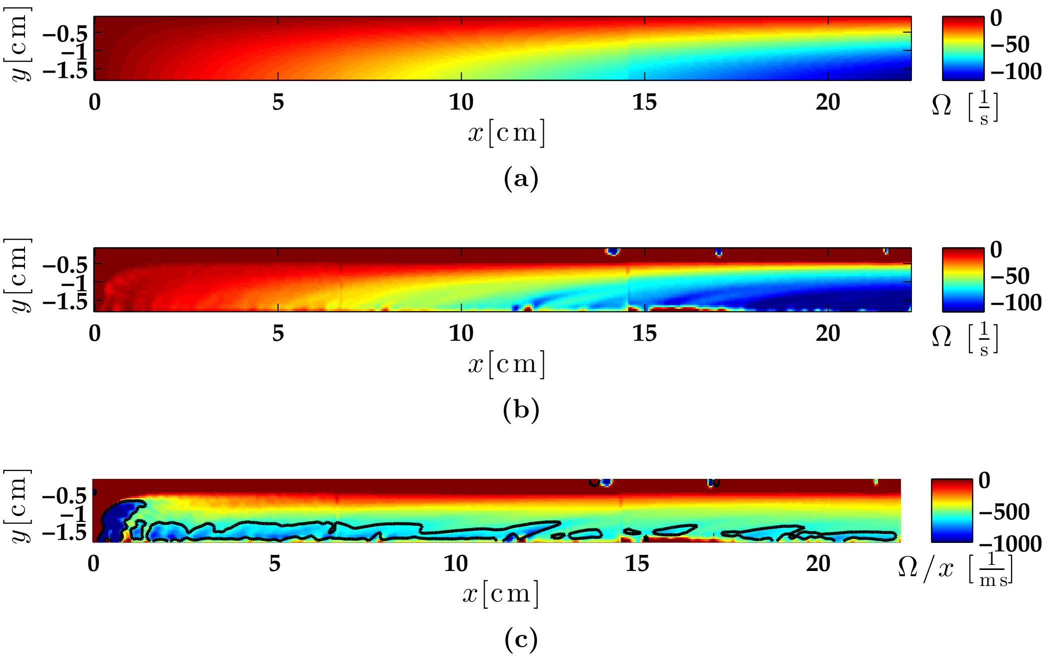

(a)

(b)

(c)

Figure 2.21. Vorticity field of: TC's solution **(a)**, experimental data **(b)**. Being Ω linear with x, spatial oscillations are highlighted by the Ω/x field in **(c)**. The black solid line is an isoline of $\Omega/x = -610$

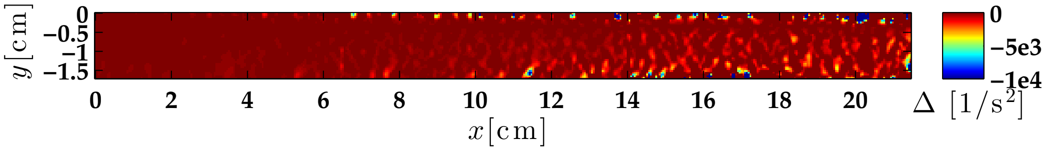

Figure 2.22. Instantaneous vortical structures highlighted with values of $\Delta < 0$. Dark red is greater than zero, while lighter colors are negative values

injection velocities higher than $0.5\,\mathrm{m\,s^{-1}}$, their results are not comparable with the one presented herein, where no significant intensity peak has been found. However, also Laboureur, Tóth, and Anthoine [118] did not find any peak of TI with a velocity injection comparable with the one in [117] and a $R_w > 2000$ for $x < 16$. The turbulent behavior appears when the height of the channel is decreased, and hence the relative distance from the head-end is elongated. Laboureur, Tóth, and Anthoine show also that the mean level of TI increases with increasing injection velocity, e.g. an injection velocity of $1\,\mathrm{m\,s^{-1}}$ yields a TI $\approx$ 10% while $v_w = 1.5\,\mathrm{m\,s^{-1}}$ yields a TI $\approx$ 15%. The turbulence intensity of the present data has the shape of the rms of u', $\sqrt{\langle u'u' \rangle}$, and is around 0.1%. Indeed, as it will be shown below with the analysis of u' and v', the main contribution to fluctuation is the linear increase of horizontal velocity that, as a consequence, enlarges its fluctuations too.

Given a time series $\{u'_n\}_{n=1}^{N_{\mathrm{im}}}$, where n denotes the n-th instantaneous field of

N_{im}, its Probability Density Function (PDF) is defined as

$$\mathrm{PDF}(u')_i = \frac{\mathrm{hist}(u')_i}{\frac{\max_n u' - \min_n u'}{N_{\mathrm{bin}}} \sum_{j=1}^{N_{\mathrm{bin}}} \mathrm{hist}(u')_j}, \quad \text{for } j = 1, \ldots, N_{\mathrm{bin}}, \tag{2.14}$$

where $\mathrm{hist}(u')_j = \#\{u'_i \in B_j \text{ for } i = 1, \ldots, N_{\mathrm{im}}\}$ is the number of velocity data that lies into the j-th bin and N_{bin} is the total number of bins. The PDF of both velocity components have been computed at different locations of the rectangular cylinder. For the horizontal component, u', the PDFs in the upper region of the chamber are barely comparable with a normal distribution, unlike in the region closer to the porous plate, as shown in Fig. 2.23. The vertical component, v', instead, follows the Gaussian law everywhere $\mathcal{N}(\mu, \sigma) \sim \frac{1}{\sigma\sqrt{2\pi}} e^{-\frac{1}{2}\left(\frac{x-\mu}{\sigma}\right)^2}$ represented with a red line, see Fig. 2.24. This indicates that where the velocity magnitude is small, fluctuations look like white noise on both velocity components. The vertical component fluctuations are everywhere of the same order of magnitude of the error ($\approx 5\,\mathrm{mm\,s^{-1}}$), therefore it is plausible that the observed gaussian distribution is the distribution of the error. However, the bimodal behavior of the u-component in the upper region shows, with longitudinal oscillations of one order of magnitude greater than transversal ones, that incoherent (Gaussian) fluctuations feed longitudinal, coherent fluctuations. Moreover, the spatial distributions of u' and v' have been reported in Fig. 2.25 and compared respectively with the first acoustic horizontal eigenmode, $h_1 = A_0 \sin(\frac{2\pi}{4L} x)$ and the fourth vertical eigenmode, $v_4 = A_0 \sin(4 \frac{2\pi}{2L} y)$, where A_0 is an amplitude comparable with the experimental data. The horizontal perturbation, even though it fluctuates periodically as stated by the PDF, has a linear profile along x instead of sinusoidal. Despite the vertical perturbations are of the order of the error, their envelope shows the oscillatory behavior of a combination of the first four modes even if it is not evident how many nodes it has.

Transversal planes In order to assess how much three-dimensionality can affect the PIV measurements on the two-dimensional plane, we have analyzed three transversal planes (z, y) at several abscissas: $x = 41\,\mathrm{mm}$, $90\,\mathrm{mm}$ and $144\,\mathrm{mm}$. Since the orthogonal velocity, u, is linear with the x, it had been impossible to measure planes for higher values of x, because particles escaped from the light sheet too fast.

The vertical component of velocity, v, except for the left and right extremities, has the same behavior obtained in the (x, y) plane, i.e. it shows jet-like structures, see Fig. 2.26a–2.26e. Note that because of particles easily escape from the measuring plane, we had been forced to reduce the delay between two consecutive images, consequently reducing the maximum displacement of each particle. This enlarged the uncertainty on the experimental data, which is inversely proportional to Δt.

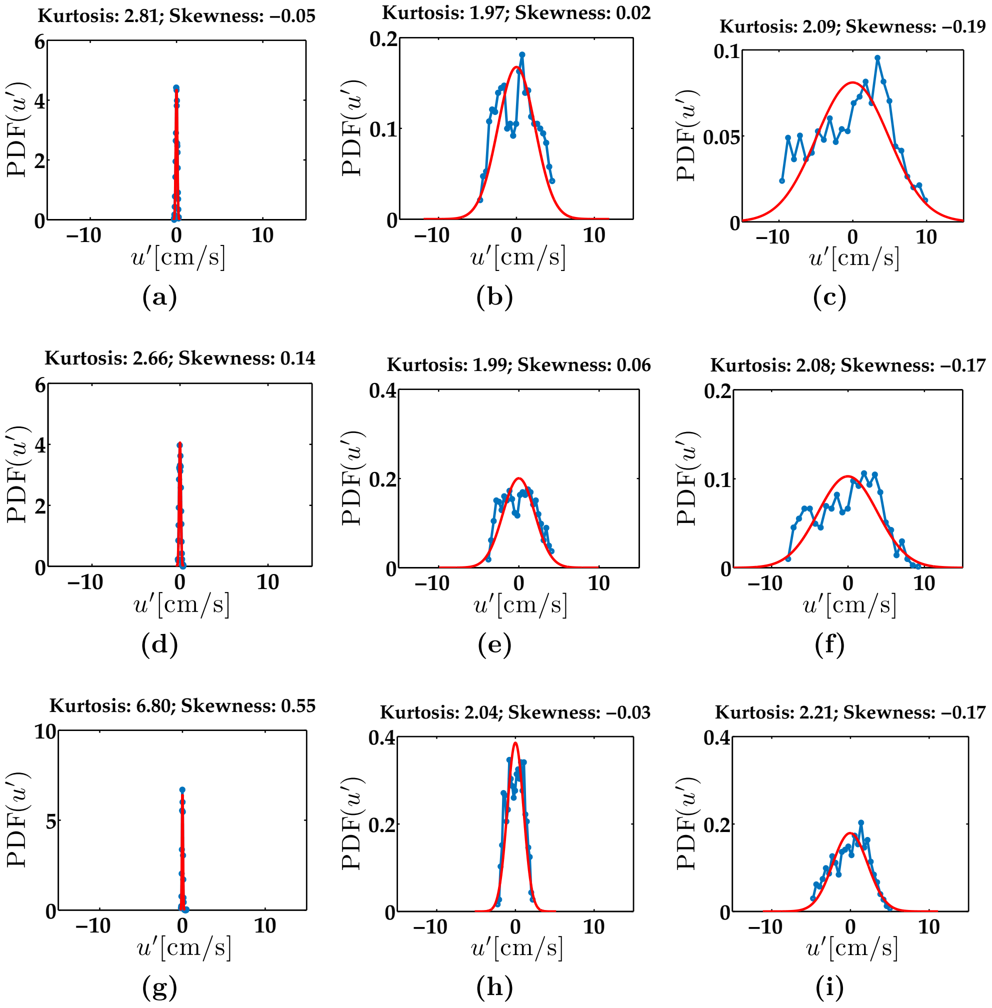

(a) (b) (c) (d) (e) (f) (g) (h) (i)

Figure 2.23. Probability density function of u' at the nine positions indicated by letters (a, b, c etc.) in Fig. 2.17. In particular, subfigure (a) corresponds to data at the point labels with (a) and so on

Fig. 2.26b, Fig. 2.26d and Fig. 2.26f show that the flow does not cross the main plane (x, y) at $z = 0$, but the contribution of w, which is due somehow to the two lateral boundaries, becomes larger as we go downstream.

As a conclusion the velocity field of a two-dimensional wall-injected channel, retrieved by means of PIV measurements, at a Reynolds number of 114 and relative distance from the head-end $x < 12$ does not show transition to turbulence being extremely distant from the Beddini's profile. The analytical model that best fits experimental data is the viscous version of the TC's profile, in fact the no-slip boundary condition at the upper wall is the most realistic one in this range of velocity. The increment of velocity magnitude, especially due to the horizontal component, as also the increasing values of fluctuations, when moving towards

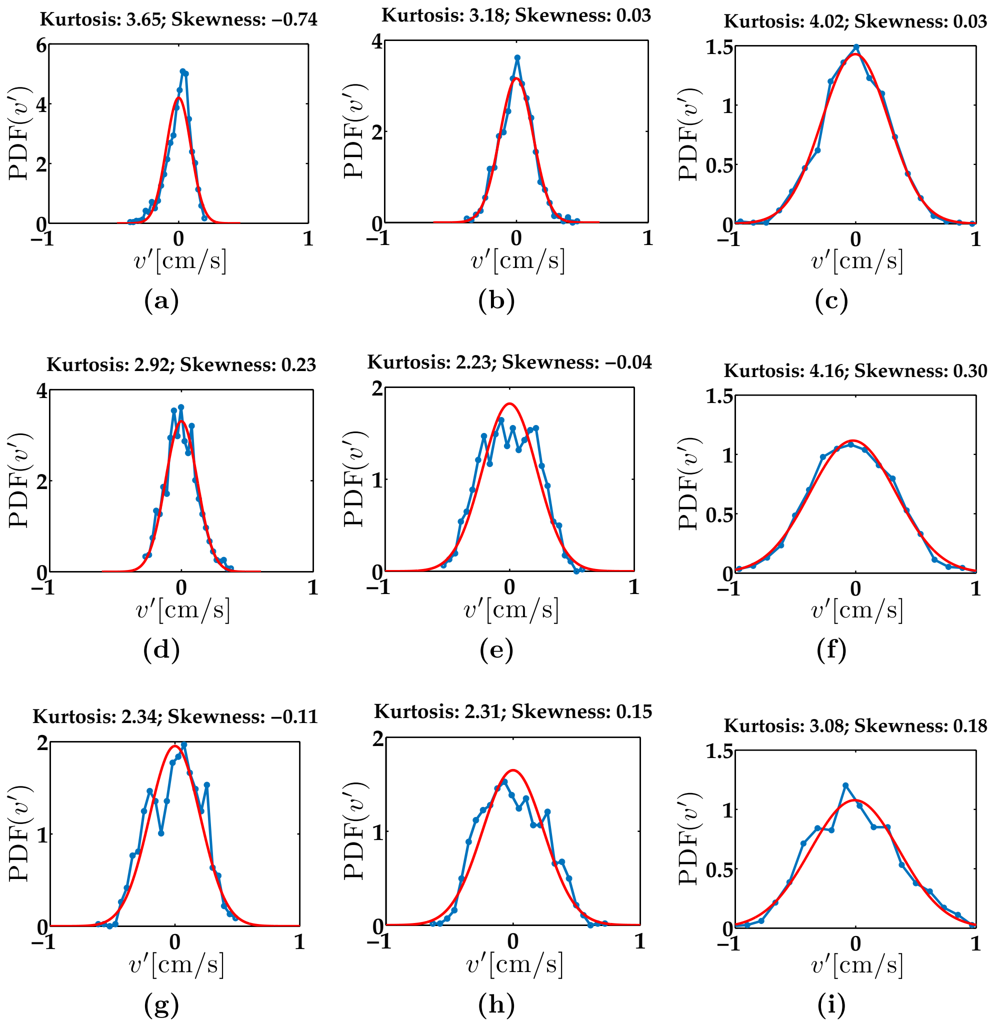

Kurtosis: 3.65; Skewness: −0.74

Kurtosis: 3.18; Skewness: 0.03

Kurtosis: 4.02; Skewness: 0.03

Kurtosis: 2.92; Skewness: 0.23

Kurtosis: 2.23; Skewness: −0.04

Kurtosis: 4.16; Skewness: 0.30

Kurtosis: 2.34; Skewness: −0.11

Kurtosis: 2.31; Skewness: 0.15

Kurtosis: 3.08; Skewness: 0.18

(a) (b) (c)

(d) (e) (f)

(g) (h) (i)

Figure 2.24. Probability density function of v' at the nine positions indicated by letters (a, b, c etc.) in Fig. 2.17. In particular, subfigure (a) corresponds to data at the point labels with (a) and so on

the outlet section, suggest that a relevant contribution to unsteadiness is due to turbulence generated by parallel jets and boundary layer, respectively on the lower and upper surfaces. Moreover we have shown a snapshot of vortical structures captured in one of the instantaneous field pointing out how these structures are growing in number, size and intensity when moving towards the outlet. These are the spatial traces of the developing turbulence on the lower and upper surfaces.

As a result of the analysis of the probability density functions of u' and v', we found two kind of oscillations, one on the u near the exit and another, similar to Gaussian noise, elsewhere. We do not believe that this Gaussian noise is due the to the sprouting of the little vortices observed, because it is present also beforehand the onset of vortices. It is more plausible that is due to the error, which is in addition of

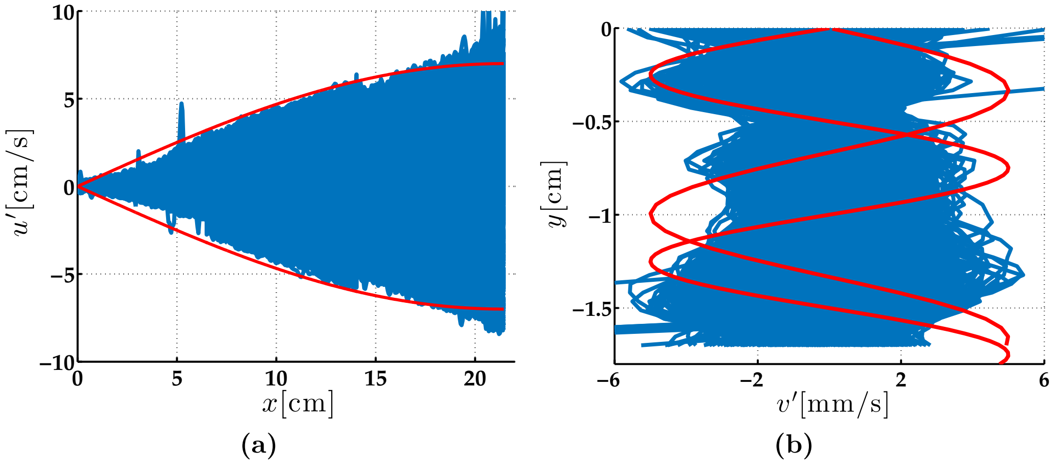

Figure 2.25. Superposition of the instantaneous $u'(x)$ at $y = -0.9\,\text{cm}$ (a) and of $v'(y)$ at $x = 0.4\,\text{cm}$ (b)

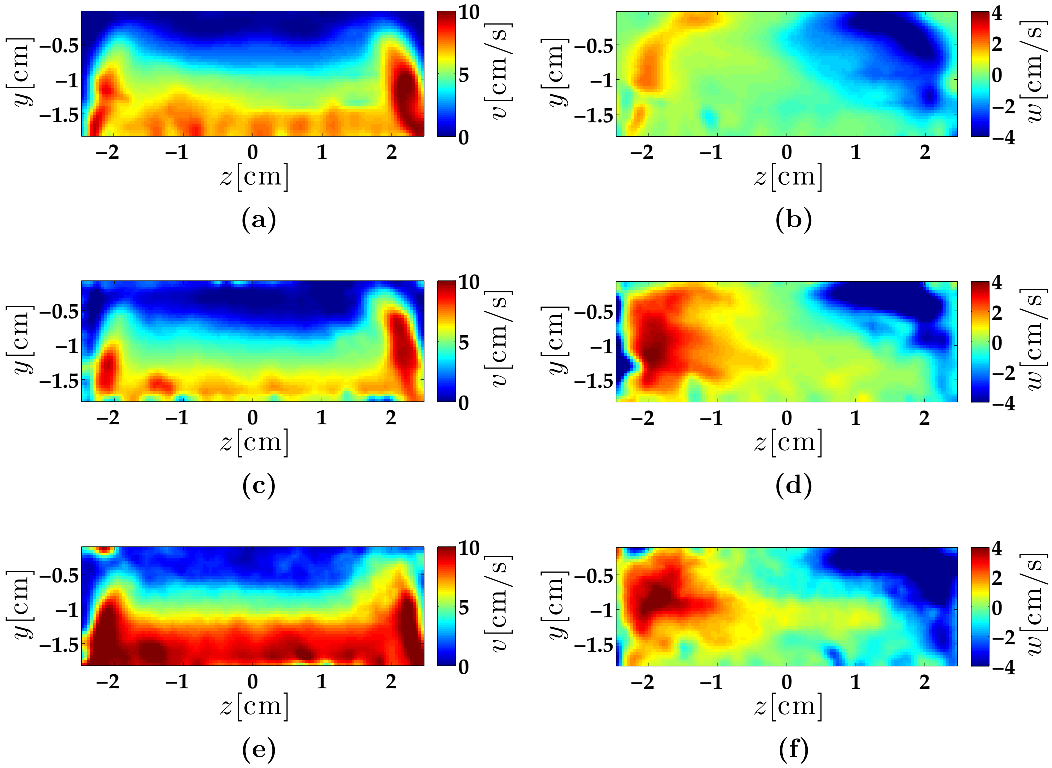

Figure 2.26. Velocity v (first column) and w (second column) on transversal planes at several positions along x: (a) and (b) at 4.1 cm, (c) and (d) at 9.0 cm and (e) and (f) at 14.4 cm

the same order of magnitude. We must observe that the primary obstacle of this kind of measurements is the extremely high difference between the order of magnitude of the vertical and horizontal component. In addition, if longer channels are taken into account, the three-dimensional effects due to the development of structures from the upper corner should not be neglected and the width of the channel should be chosen opportunely.

2.4.2 Cavity configuration

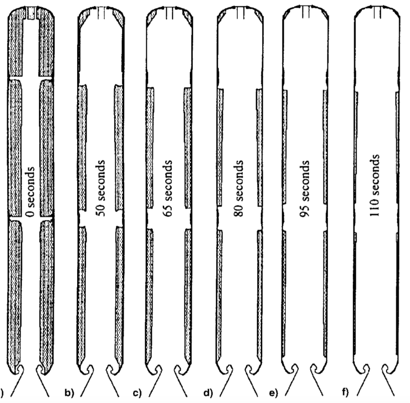

Figure 2.27. Segmented motor internal geometry (Ref. [119])

The presence of cavities along the propellant grain surface is recurrent, segmented geometries have several cavities as shown in Fig. 2.27, but also in aft-finocyl SRMs the nozzle generates a region comparable to a cavity. Moreover, the characteristic dimensions, i.e. depth D_c and length L_c, of these cavities vary during the burning process showing amplification of oscillations at well-defined temporal windows, hence at given geometrical configurations. Thus, only some of them are significant and should be investigated. In general, cavities are divided into open and closed cavities. Open cavities refer to flow over cavities where the boundary layer separates at the upstream corner and reattaches near the downstream corner. Cavities are closed when the separated layer reattaches at the cavity bottom and again separates ahead of the downstream wall. Another parameter that must be taken into account is the velocity of the flow over the cavity. In fact, Sarohia [120] states that the demarcation line between open and closed cavities is $L_\mathrm{c}/D_\mathrm{c} \approx 11$ for a supersonic flow and $L_\mathrm{c}/D_\mathrm{c} \approx$ 7-8 at low subsonic speeds. Open cavities may further be divided into deep and shallow cavities. Deep cavities act as resonators, whereas shallow cavities show oscillating phenomena which are not related to the standing longitudinal acoustic wave. For $L_\mathrm{c}/D_\mathrm{c} < 1$ the cavity may be considered deep and for $L_\mathrm{c}/D_\mathrm{c} > 1$ may be considered shallow.

The main source of disturbance in a shallow cavity resides in the transition of the boundary-layer, which is characterized by the upstream flow into the shear-layer at the upstream corner. The ability of the shear layer to roll-up into several vortices can determine the mode of oscillations at low-Reynolds number, according to the Rossiter's model [121]. This roll-up mechanism is governed by the ratio L_c/θ_0, with θ_0 the momentum thickness of the separating boundary layer, or equivalently L_c/δ_0, with δ_0 is the boundary displacement thickness[3]. Sarohia [120] found a

---

[3] θ_0 and δ_0 determines the shape factor δ_0/θ_0 of the boundary layer

L_c[cm]	D_c[cm]	Cavity injection	Injecting surface[cm^2]
1	1	yes	85
3	1	yes	95
3	1	no	80
6	1	yes	110
∞	1	yes	120

Table 2.3. Geometrical configurations of the measured cavities

minimum length $\bar{L}_\mathrm{c} \sim \delta_0^{3/2}$ for $D_\mathrm{c}/\delta_0 > 2$ and laminar boundary layers below which no oscillations occur. Gharib and Roshko [141] analyzed the behavior of the cavity shear layer and found a relationship between L_c/θ_0 and the oscillation modes: “self-sustained modes” characterized by the presence of a finite number of vortices and “wake mode” accompanied by a large increase of drag. In addition, they compared the cavity shear layer with the free shear layer highlighting the following differences: the maximum shear stress increases exponentially in contrast with the self-similarity of the free shear layer. Nevertheless, the momentum thickness of the latter increases linearly, like that in a turbulent free shear layer.

In the present study, the upstream flow is generated by wall-injection, hence the boundary layer at the upstream corner is blown off and all the considerations about the roll-up mechanism does not apply directly. Moreover, the injection from the bottom part of the cavity has been taken into account. The characteristic dimensions of the upstream, wall-injecting channel are: $H = 1\,\mathrm{cm}$ (height) and $L = 16\,\mathrm{cm}$ (length). The cavity is 1 cm deep, i.e. $D_\mathrm{c} = 1\,\mathrm{cm} = H$, and has variable length. All the considered configurations are reported in Tab. 2.3 where, in addition to the cavity dimensions, one can find whether the bottom wall of the cavity is porous, and hence there is injection within the cavity itself, or non-porous and the total injecting surface, i.e. the width of the channel times the length of the injecting surface, which is useful for computation of the flow rate.

The velocity profile at the upstream corner of the cavity depends on the aspect ratio of the upstream channel. In this configuration a maximum horizontal velocity of $2\,\mathrm{m\,s^{-1}}$ has been obtained. Little variations of this value are due to the different global injecting surface, for instance a higher velocity will be obtained when the cavity does not inject than when it does, see Fig. 2.28b and Fig. 2.28c.

In Fig. 2.28 the velocity magnitude fields with some streamlines of the five configurations are reported. Although the expansion slows the flow in all the configurations, in Fig. 2.28a-2.28b-2.28d the highest speed is obtained downstream because of both the injection and the restriction, while in Fig. 2.28c and Fig. 2.28e neither only restriction nor only injection are respectively narrow and long enough

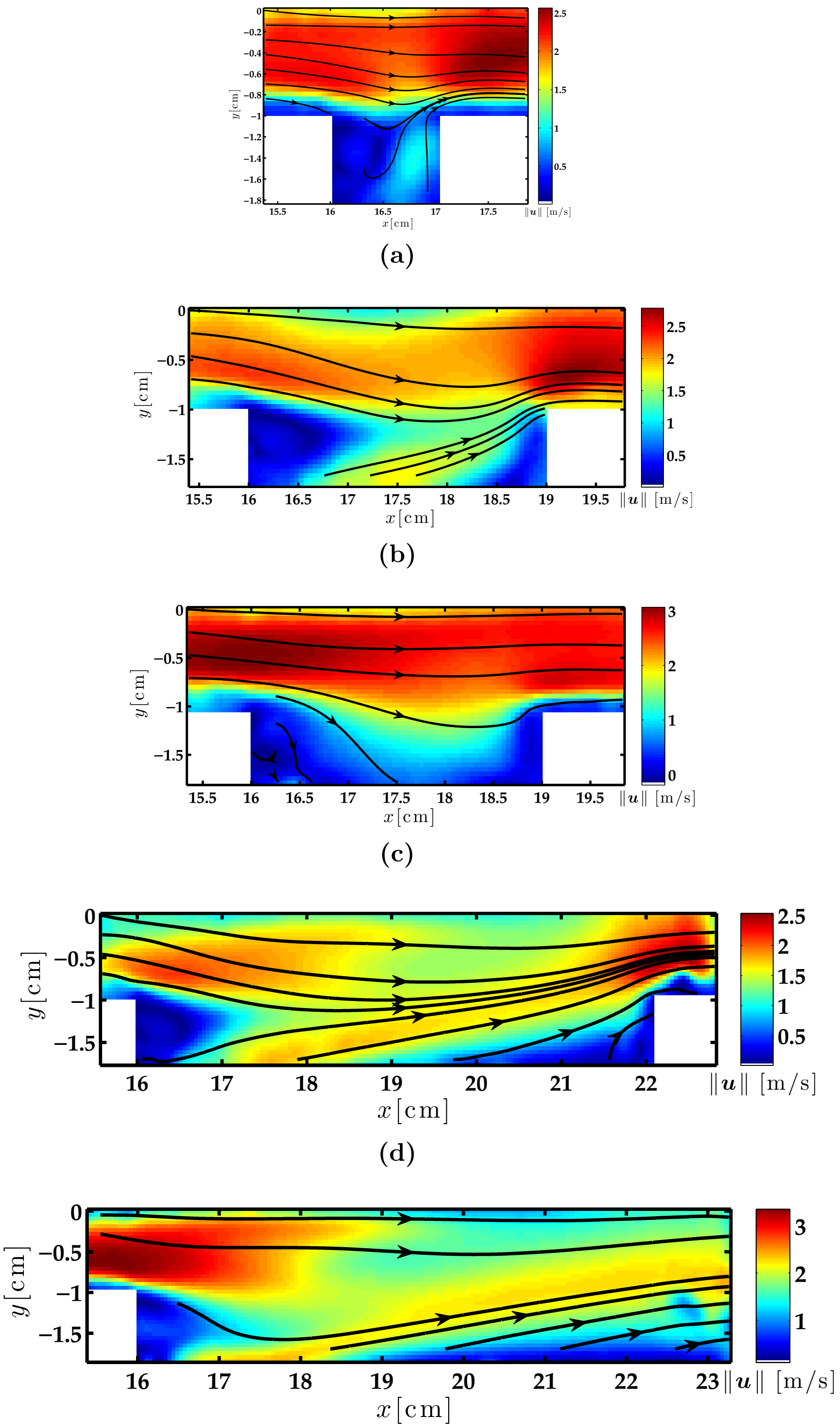

(a)

(b)

(c)

(d)

(e)

Figure 2.28. Velocity magnitude of all the five configurations reported in Tab. 2.3

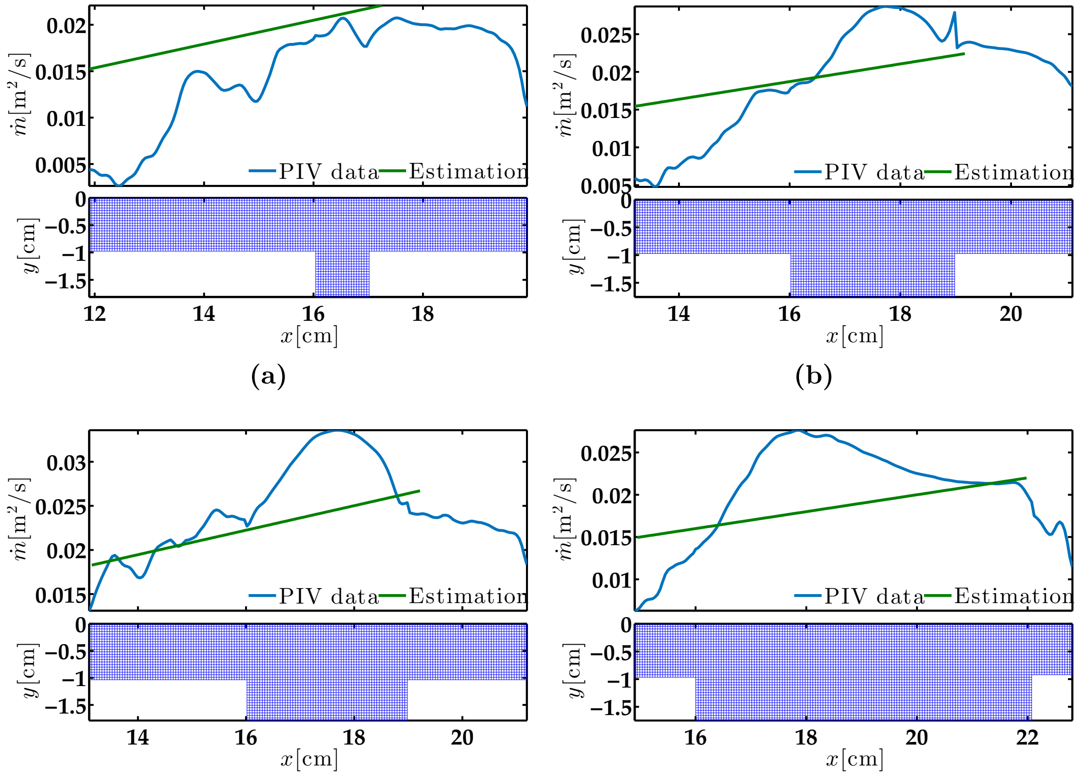

(a)

(b)

(c) non-injecting cavity

(d)

Figure 2.29. Variation of flow rate with distance from the head end of the channel

to re-accelerate the flow. When $L_\mathrm{c}/D_\mathrm{c} = 1$, i.e. the limiting case between deep and shallow cavity, the streamlines are more similar to the non-injected case than to the injected one.

In order to validate the measurements, a comparison between the measured flow rate, i.e. computed from integration of PIV data, and the estimation derived from the feeding tube flow rate has been carried on. The injecting surface changes for each configuration: from the downstream corner of the cavity to the aft end it does not inject, whereas it always inject from the head end to the upstream corner of the cavity. However, the injecting surfaces are reported in Tab. 2.3. Being the feeding tube flow rate always equal to $1.117 \times 10^{-3}\,\mathrm{m}^3/\mathrm{s}$, one can compute the estimated injecting velocity, $v_\mathrm{w} = \dot{m}/A$, and hence find the slope of the linear law $\dot{m} = v_\mathrm{w} x$, which has been represented in Fig. 2.29 together with the flow rate estimated by means of PIV data. This comparison shows a discordance between the linear growth and the PIV data in the first fourth of the plot, which is likely due to a non-correct illumination of the images and hence to lack of accuracy of the result. Anyhow, at the downstream corner of the cavity the PIV data yield the correct value of flow rate and remain constant because there is no injection anymore. Within the cavity,

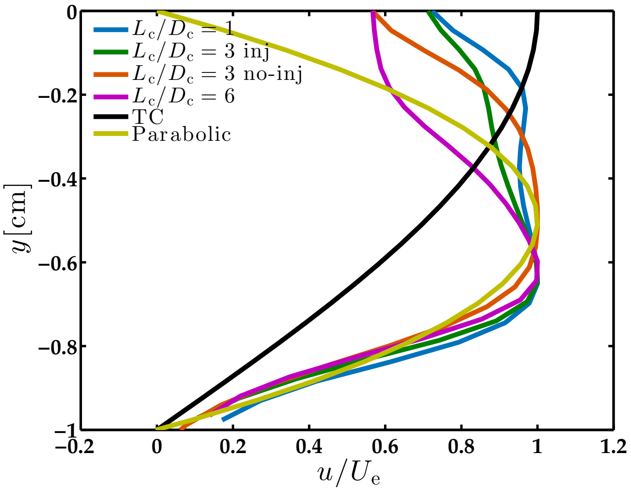

Figure 2.30. Horizontal velocity profile above the upstream corner of the cavity

the linear growth is not satisfied because of the abrupt change in geometry, except for the case $L_c/D_c = 1$ where the effect is not perceivable, instead a likely parabolic behavior is observed for $L_c/D_c = 3$, whereas for the longer cavity, $L_c/D_c = 6$, after the sudden increase, $\dot{m}$ smoothly decreases towards the constant value.

As pointed out at the beginning of this section, the behavior of the cavity shear layer is strictly related to the properties of the velocity profile upstream the cavity. Let be U_e the maximum value of the velocity at the upstream corner, i.e. $U_e = \max_y u(y, 16)$. Noting that the presence of the cavity deflects the streamlines downward, see Fig. 2.28, the upper wall boundary layer is warped. Despite the parameters of the channel upward the cavity are $\mathrm{Re}_{\mathrm{inj}} \gtrsim 200$ and relative distance $0 \leq x \leq 16$, the velocity profiles, shown in Fig. 2.30, are quite parabolic rather than similar to TC. It seems that the presence of the cavity yields a suction process that bends the velocity peak downward. In addition the upper wall boundary layer thickness increases as the cavity length increases because, as shown by the flow rate, the horizontal velocity decreases. However, even though nominally the boundary layer at the injecting wall does not exist, from Fig. 2.30 the boundary layer thickness δ_0 is around 2 mm. Hence, being $D_c/\delta_0 > 2$, the minimum length $\bar{L}_c \approx 2.8$ mm, which is much more smaller than the present lengths.

In order to analyze the behavior of the cavity shear layer, the shear stress $\langle u'v' \rangle$ and the momentum thickness

$$\theta(x) = \int_{\infty}^{-\infty} \frac{u}{U_e}\left(1 - \frac{u}{U_e}\right) dy, \tag{2.15}$$

where the actual range of integration is between two ys such that $du/dy = 0$, are reported. The cavity $L_c/D_c = 1$ presents a fluctuating behavior similar to a jet

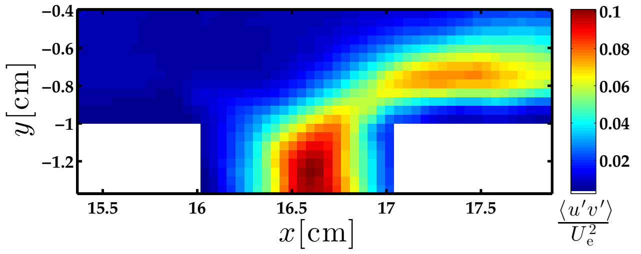

Figure 2.31. Shear stress of the cavity $L_\mathrm{c}/D_\mathrm{c} = 1$

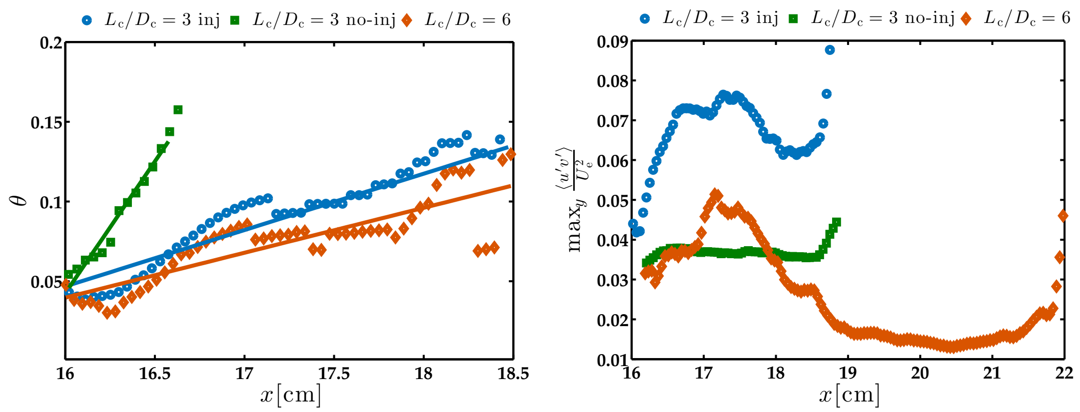

(a) **(b)**

Figure 2.32. Variations of θ **(a)** and $\max_y \frac{\langle u'v'\rangle}{U_\mathrm{e}^2}$ **(b)** with streamwise distance

cross-flow rather than a cavity shear layer, as shown in Fig. 2.31. Therefore, a comparison between the other three configurations is more interesting.

Fig. 2.32a shows the linear growth of the momentum thickness but, in contrast with the Sarohia [120] results, the growth rate decreases with increasing cavity lengths. Moreover, for the same cavity length we have found $d\theta/dx = 0.035$ with the injecting cavity and $d\theta/dx = 0.162$ with the inert cavity. Hence, the injection seems to reverse the behavior observed by Sarohia. Nevertheless, the maxima of the shear stress profiles result constant for the inert cavity, as in a self-similar free turbulent shear layer, and increasing for $16 < x < 17.5$ for the two injecting cavities. It is noteworthy that $\max_y \frac{\langle u'v'\rangle}{U_\mathrm{e}^2}$, for injected cavities, grows in a range that is independent from the length of the cavity. A more stable region is present within the injected cavities, clearly visible in the longer cavity (see Fig. 2.33c), and characterized by the downward slope of the maxima of the shear stress profiles.

Despite the relative shear stresses are higher for injected cavities than for the inert one, they appear more concentrated in the region where the shear layer merges with the injection of the cavity. It is reasonable to localize this point, which is moreover independent from L_c, as the point where $\max_y \frac{\langle u'v'\rangle}{U_\mathrm{e}}$ reaches its maximum value, i.e.

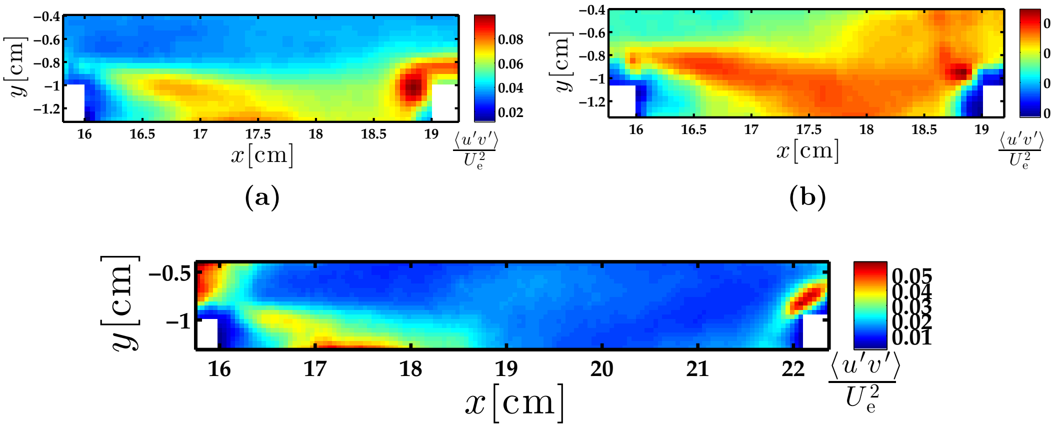

(a) **(b)**

(c)

Figure 2.33. Shear stress $\frac{\langle u'v'\rangle}{U_\mathrm{e}^2}$ field: $L_\mathrm{c}/D_\mathrm{c} = 1$ injected **(a)**, non-injected **(b)** and $L_\mathrm{c}/D_\mathrm{c} = 6$ **(c)**

$x_\mathrm{m} = 17.5\,\mathrm{cm}$. Probably, x_m would not be independent neither from v_w nor from the abscissa of the upstream corner x_c, which lastly determines $U_\mathrm{e} = U_\mathrm{e}(x_\mathrm{c}, v_\mathrm{w})$.

Although the present study is based on statistical tools, hence instantaneous fields does not provide much information, and moreover the sample rate is low, hence no frequency analysis can be carried on, the fact that the non-injected cavity shows a constant profile of $\max_y \frac{\langle u'v'\rangle}{U_\mathrm{e}^2}$ suggests that no self-sustained oscillating mechanism is present. This is probably due to the small value of $\mathrm{Re}_{\delta_0} = U_\mathrm{e}\delta_0/\nu \approx 250$ with respect to the range adopted in [120], i.e. 500-2000, where instead oscillating phenomena were observed.

Chapter 3

Numerical simulations

In this chapter, the numerical scheme adopted to simulate the experimental configuration analyzed in the previous chapter is presented and validated. Being a confined geometry, the boundary conditions play a crucial role and in addition several types of boundaries are involved. Since the target of the numerical code is a low-speed channel, the Navier-Stokes equation have been directly solved by means of a high-order, Finite-Difference (FD) method. Moreover, as the considered geometries, i.e. straight channel and cavities, do not require curvilinear transformation, hence the numerical discretization is implemented on cartesian meshes.

The Chapter is organized as follows. At first, the technique of discretization of the Navier-Stokes equation is presented and its features are discussed. Then, the implementation of the boundary conditions by means of the Navier-Stokes Characteristic Boundary Conditions (NSCBC) is reported and adapted to the present calculation. Afterwards, some test are presented in order to explore the potential of the code and to validate it. Finally, the numerical simulations of the closed-open chamber are discussed.

3.1 Numerical scheme

It is useful in this framework to consider the compact, conservative form of the Navier-Stokes equation in two-dimensional Cartesian coordinates

$$\frac{\partial \boldsymbol{U}}{\partial t} + \frac{\partial (\boldsymbol{F} - \boldsymbol{F}_\mu)}{\partial x} + \frac{\partial (\boldsymbol{G} - \boldsymbol{G}_\mu)}{\partial y} = \boldsymbol{0}, \tag{3.1}$$

with $\boldsymbol{U} = (\rho, \rho u, \rho v, \rho E)^T$ the conserved variables, $\boldsymbol{F}$ and $\boldsymbol{G}$ the inviscid flux vectors, which can be expressed as

$$\boldsymbol{F} = \begin{bmatrix} \rho u \\ \rho u u + p \\ \rho u v \\ \rho u h \end{bmatrix}, \quad \boldsymbol{G} = \begin{bmatrix} \rho v \\ \rho u v \\ \rho v v + p \\ \rho v h \end{bmatrix}, \tag{3.2}$$

$\boldsymbol{F_\mu}$ and $\boldsymbol{G_\mu}$ the viscous flux vectors, which can be expressed as

$$\begin{aligned} \boldsymbol{F}_\mu &= \begin{bmatrix} 0 \\ \mu\left(\frac{4}{3}\frac{\partial u}{\partial x} - \frac{2}{3}\frac{\partial v}{\partial y}\right) \\ \mu\left(\frac{\partial u}{\partial x} + \frac{\partial v}{\partial y}\right) \\ \mu\left(\frac{4}{3}\frac{\partial u}{\partial x} - \frac{2}{3}\frac{\partial v}{\partial y}\right) u + \mu\left(\frac{\partial v}{\partial x} + \frac{\partial u}{\partial y}\right) v \end{bmatrix}, \\ \boldsymbol{G}_\mu &= \begin{bmatrix} 0 \\ \mu\left(\frac{\partial v}{\partial x} + \frac{\partial u}{\partial y}\right) \\ \mu\left(\frac{4}{3}\frac{\partial u}{\partial x} - \frac{2}{3}\frac{\partial v}{\partial y}\right) \\ \mu\left(\frac{\partial u}{\partial x} + \frac{\partial v}{\partial y}\right) u + \mu\left(\frac{4}{3}\frac{\partial u}{\partial x} - \frac{2}{3}\frac{\partial v}{\partial y}\right) v \end{bmatrix}. \end{aligned} \tag{3.3}$$

The numerical discretization of Eq. 3.1 proposed by Daude et al. [122] splits the time integration from the spatial discretization, hence yielding a semi-discrete problem

$$\frac{d\boldsymbol{U}_{ij}}{dt} + \boldsymbol{R}_{ij} = \boldsymbol{0}, \tag{3.4}$$

where $\boldsymbol{R}_{ij}$ is the residual of the discretized flux vectors. Here, i and j individuate the spatial position on the discrete two-dimensional grid.

Spatial discretization On a uniform grid $\{x_i\}$, the first spatial derivative of a function f can be approximated using a finite-difference scheme by

$$\left(\frac{\partial f}{\partial x}\right)_i \approx \mathrm{FD}[f](x_i) = \frac{1}{\Delta x} \sum_{j=-P}^{Q} a_j f(x_i + j\Delta x), \tag{3.5}$$

with Δx the mesh spacing and a_j the stencil coefficients. The stencil is composed by P points left to x_i and Q points right to x_i. When $P = Q = N$, the finite-difference scheme is centered. In the present work we use a 7-point stencil: for interior points, the scheme is centered, whereas for points near the boundary, a non-centered scheme has been adopted as illustrated in Fig. 3.1. The coefficients a_i of standard finite-difference schemes are determined to cancel the terms of the Taylor series of (3.5),

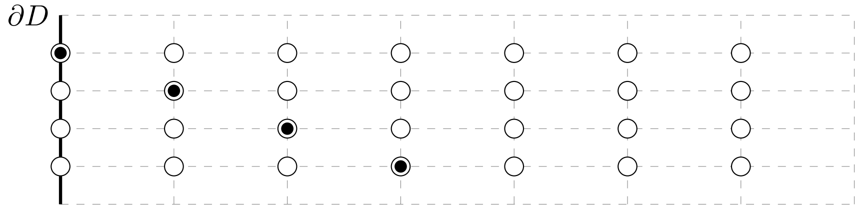

Figure 3.1. Stencils of the 7-point finite-difference scheme adopted to approximate the first x derivative of a function at the black dots

i.e.

$$f_i' \approx \frac{1}{\Delta x}\sum_{j=-P}^{Q} a_j f(x_i + j\Delta x) = \sum_{j=-P}^{Q} a_j \sum_{k=0}^{P+Q} \frac{1}{k!} f_i^{(k)} j^k (\Delta x)^{k-1} + \mathcal{O}(\Delta x)^{P+Q} \tag{3.6}$$

that yields the following system of $P+Q+1$ equations

$$\sum_{j=-P}^{Q} a_j j^k = \begin{cases} 1, & \text{if } k = 1 \\ 0, & \text{otherwise} \end{cases} \tag{3.7}$$

and provides a $(P+Q)^{\text{th}}$-order accurate scheme. However, in this work, a scheme proposed by Tam and Webb [123] has been adopted. This kind of schemes is knowns as Dispersion-Relation-Preserving (DRP) finite-difference schemes, because the coefficients are defined to minimize the dispersion error. In order to find the dispersion error, the spatial Fourier transform is applied to (3.5). For the sake of simplicity, let us consider the centered case, hence

$$k^* \Delta x = 2 \sum_{j=1}^{N} a_j \sin(jk\Delta x) \tag{3.8}$$

is the expression of the effective wavenumber yielded by the numerical scheme. Since the dispersion error is the difference between the effective and the exact wave numbers: $E(k\Delta x) = |k^*\Delta x - k\Delta x|/\pi$; in order to have a small value of E over the range of wavenumbers $|k\Delta x| < \pi/2$, i.e. waves with wave length longer than four Δx, a_j are required to satisfy the minimum condition of the integral error

$$\begin{aligned} E &= \int_{-\pi/2}^{\pi/2} |k^*\Delta x - k\Delta x|^2 \, d(k\Delta x), \\ \frac{\partial E}{\partial a_j} &= 0, \end{aligned} \tag{3.9}$$

which provides a system of linear algebraic equations.

A common practice to find high-order schemes with optimized coefficients that reduce the dispersion error is to combine Eq. (3.7) (traditional FD) with Eq. (3.9) (optimized FD). Tam and Webb imposed an order of accuracy of $(\Delta x)^4$ with a 7-point stencil, hence five parameter are fixed. In addition, they assumed $a_0 = 0$ implying $a_j = -a_{-j}$, therefore this leaves one of the coefficients as a free parameter. This parameter has been chosen according to Eq. (3.9) leading to the following coefficients

$$\begin{aligned} a_0 &= 0 \\ a_1 &= -a_{-1} = 0.79926643 \\ a_2 &= -a_{-2} = -0.18941314 \\ a_3 &= -a_{-3} = 0.02651995. \end{aligned} \tag{3.10}$$

Starting from the fourth-order conditions, Bogey and Bailly [124] developed optimized schemes with nine, eleven and thirteen-point stencils that on the one hand further improve the dispersion relation preserving property, but on the other enlarge the stencil and, as a consequence, the computational cost without any improvement of the accuracy.

The centered scheme (3.10) cannot be used at the boundary points, i.e. those points that lie on the boundary and on the two next columns or rows as depicted in Fig. 3.1. In order to determine an optimized scheme, in the sense of DRP, suitable for boundary points, Berland et al. [125] proposed the same procedure adopted by Tam and Webb for non-centered finite difference schemes, i.e. $P \neq Q$. While centered-schemes are dissipation-free and, indeed, the effective wavenumber is real, in this case the effective wavenumber is complex and reads

$$k^* \Delta x = -i \sum_{j=-P}^{Q} a_j e^{ijk\Delta x}. \tag{3.11}$$

In order to take into account both dispersion and dissipation, a parameter α has been introduced into the integral error

$$\int_{\pi/16}^{\pi/2} \left[(1-\alpha)|k\Delta x - \Re(k^*\Delta x)| + \alpha |k\Delta x - \Im(k^*\Delta x)|\right] \frac{d(k\Delta x)}{k\Delta x}. \tag{3.12}$$

The schemes, denoted by FD_{PQ} are summarized in Tab. 3.1. A comparison of the dispersion and dissipation error of the non-centered schemes with the centered ones cited above can be found in [125].

Temporal integration The spatial discretization of both the two flux-vectors, $\boldsymbol{F} - \boldsymbol{F}_\mu$ and $\boldsymbol{G} - \boldsymbol{G}_\mu$, respectively in the x and y direction, yields the residual $\boldsymbol{R}_{ij}$. It is noteworthy that before the discretization of the global flux-vectors, a

	FD_{33}	$\mathrm{FD}_{24}(\alpha=0.5)$	$\mathrm{FD}_{15}(\alpha=0.5)$	$\mathrm{FD}_{06}(\alpha=0.25)$
a_{-3}	-0.02651995			
a_{-2}	0.18941314	0.04826409410		
a_{-1}	-0.79926643	-0.48825583084	-0.21293272195	
a_0	0	-0.36601559072	-1.06032039077	-2.22583396327
a_1	0.79926643	1.04800545585	2.07892611643	4.82777958057
a_2	-0.18941314	-0.28932592639	-1.28717945238	-5.00138845383
a_3	0.02651995	0.05039243769	0.68517639547	3.91110394164
a_4		-0.00306463969	-0.24532061399	-2.11526745863
a_5			0.04165066718	0.71888278441
a_6				-0.11527643089

Table 3.1. Coefficients of the seven-point optimized schemes

α_1	α_2	α_3	α_4
1/4	1/3	1/2	1

Table 3.2. Coefficients of standard four-stage Runge-Kutta (RK4)

preliminary discretization has been made in order to compute the stress tensor components. In order to integrate the semi-discrete problem (3.4), the four-stage explicit Runge-Kutta method (RK4) has been adopted, as in [122]. Hence

$$\begin{cases} \boldsymbol{U}_{ij}^{(k)} = \boldsymbol{U}_{ij}^{n} + \alpha_k \Delta t \boldsymbol{R}_{ij}^{(k-1)}, \quad \text{for all } i, j \text{ and } k = 1, \ldots, 4 \\ \boldsymbol{U}_{ij}^{(0)} = \boldsymbol{U}_{ij}^{n}, \end{cases} \tag{3.13}$$

where α_k are reported in Tab. 3.2 and superscript n denotes the solution at the discrete time $t_n = t_{n-1} + \Delta t$. The time step Δt is limited by explicit stability requirement linked to the CFL value

$$\mathrm{CFL} = \max\left\{ \max_{ij}(|u_{ij}| + a_{ij})\Delta t/\Delta x, \max_{ij}(|v_{ij}| + a_{ij})\Delta t/\Delta y \right\} \tag{3.14}$$

with $a = \sqrt{\gamma p/\rho}$ the speed of sound.

Filtering process Since grid-to-grid oscillations are not resolved by centered, finite-difference schemes, an additional operation to remove them must be considered. It is common practice to introduce artificial damping terms [126] or to filter the solution [127]. The filtering procedure can be expressed as

$$\mathrm{SF}[f](x_i) = f(x_i) - \sigma \sum_{j=-P}^{Q} d_j f(x_i + j\Delta x), \tag{3.15}$$

	SF_{33}	$\mathrm{SF}_{24}(\alpha = 1)$	$\mathrm{SF}_{15}(\alpha = 0.9)$	$\mathrm{SF}_{03}(\alpha = 0)$
d_{-3}	-0.007175683			
d_{-2}	0.074469480	0.032649010764		
d_{-1}	-0.242824317	-0.143339502575	-0.085777408970	
d_0	0.351061040	0.273321177980	0.277628171524	0.320882352941
d_1	-0.242824317	-0.294622121167	-0.356848072173	-0.465000000000
d_2	0.074469480	0.186711738069	0.223119093072	0.179117647059
d_3	-0.007175683	-0.062038376258	-0.057347064865	-0.035000000000
d_4		0.007318073189	-0.000747264596	
d_5			-0.000027453993	

Table 3.3. Coefficients of the seven-point optimized selective filters

where σ is a damping constant and d_j are the filter coefficients. It is possible to find coefficients that reduce spurious oscillations following the same procedure used to define the spatial derivatives [128], that is in the Fourier space. Moreover, standard explicit non-centered selective filters are unstable [129], therefore we have adopted the coefficients proposed by Berland et al. [125], which are reported in Tab. 3.3 with the same notation of the finite-difference scheme: SF_{PQ}. Despite a 7-point completely off-centered filter is provided by the optimization procedure, it shows excessive damping. A 4-point filter, denoted by SF_{03}, has nevertheless been designed with $\alpha = 0$, i.e. by putting emphasis only on the amplitude. However, for small wave numbers the amount of dissipation is one order of magnitude larger with respect to the other boundary filters and should be used with a σ ten times lower than the other filters.

The complete algorithm can be thus summarized as follows:

$$\begin{cases} \Delta t = \Delta t(\mathrm{CFL}), & \text{(CFL condition)} \\ \boldsymbol{U}_{ij}^{(0)} = \boldsymbol{U}_{ij}^{n}, & \text{(initialization)} \\ \mathrm{FD}[\boldsymbol{U}^{(k-1)}] \rightarrow \boldsymbol{R}_{ij}^{(k)}, \quad k = 1, \dots, 4 & \text{(space discretization)} \\ \boldsymbol{U}_{ij}^{(k)} = \boldsymbol{U}_{ij}^{n} + \Delta t \alpha_k \boldsymbol{R}_{ij}^{(k)}, \quad k = 1, \dots, 4 & \text{(time discretization)} \\ \boldsymbol{U}_{ij}^{n+1} = \boldsymbol{U}_{ij}^{(4)} - \sigma \left[\sum_{n=1}^{3} \sum_{m=-3}^{3} d_m \boldsymbol{U}_{i+\delta_{n1}, j+\delta_{n2}, k+\delta_{n3}}^{(4)} \right], & \text{(filtering)} \end{cases} \tag{3.16}$$

The global stability of the scheme depends on the choice of CFL and σ. Daude et al. showed that the algorithm is stable with $\sigma = 0.2$ and CFL < 1. It should be pointed out that unsymmetrical schemes adopted on the boundary points are inclined to be unstable, in fact Tam and Webb stated that such an unsymmetrical schemes when are used over a large region generally lead to spatially growing wave. However, they may be employed in limited regions, such as the boundary regions of the computation domain, without leading to accumulated numerical instability.

3.2 Boundary conditions

In order to define boundary conditions, the strategy proposed by Thompson [130] based on the characteristic wave relations through boundaries has been employed. As stated by Thompson, the hyperbolic nature of the inviscid terms of the Navier-Stokes equations governs the propagation of waves. Every point of the domain is perturbed by waves that comes from all the directions. For boundary points, there must be, in subsonic regime, some wave that comes from outside the domain. These waves define the behavior of the boundary and must be treated appropriately. However, Navier-Stokes equations are not hyperbolic and dissipative terms certainly change the nature of the waves that, nevertheless, are still propagated. Poinsot and Lele [131], suggest that Euler boundary conditions are the first order candidates to treat the Navier-Stokes boundary conditions. In the present work, where boundaries are always aligned with the axis, the splitting of the convective terms is straightforward and therefore waves are directly identified.

Let us consider a boundary normal to the x-direction, i.e. $x = L$, and for brevity let be $m = \rho u$ and $q = \rho v$. Hence, the Riemann invariants along the x-direction characteristics are

$$\frac{\partial p}{\partial t} - \rho a \frac{\partial u}{\partial t} + \mathcal{L}_1 = 0 \tag{3.17}$$

$$\frac{\partial p}{\partial t} - a^2 \frac{\partial \rho}{\partial t} + \mathcal{L}_2 = 0 \tag{3.18}$$

$$\frac{\partial v}{\partial t} + \mathcal{L}_3 = 0 \tag{3.19}$$

$$\frac{\partial p}{\partial t} + \rho a \frac{\partial u}{\partial t} + \mathcal{L}_4 = 0, \tag{3.20}$$

where

$$\mathcal{L}_1 = \lambda_1 \left(\frac{\partial p}{\partial x} - \rho a \frac{\partial u}{\partial x} \right) \tag{3.21}$$

$$\mathcal{L}_2 = -\lambda_2 \left(\frac{\partial p}{\partial x} - a^2 \frac{\partial \rho}{\partial x} \right) \tag{3.22}$$

$$\mathcal{L}_3 = \lambda_3 \frac{\partial v}{\partial x} \tag{3.23}$$

$$\mathcal{L}_4 = \lambda_4 \left(\frac{\partial p}{\partial x} + \rho a \frac{\partial u}{\partial x} \right), \tag{3.24}$$

with $\lambda_1 = u - a$, $\lambda_2 = \lambda_3 = u$ and $\lambda_4 = u + a$, are the wave strengths. Eqs. (3.17)–(3.20) are called Local One Dimensional Inviscid (LODI) system [131] and may be

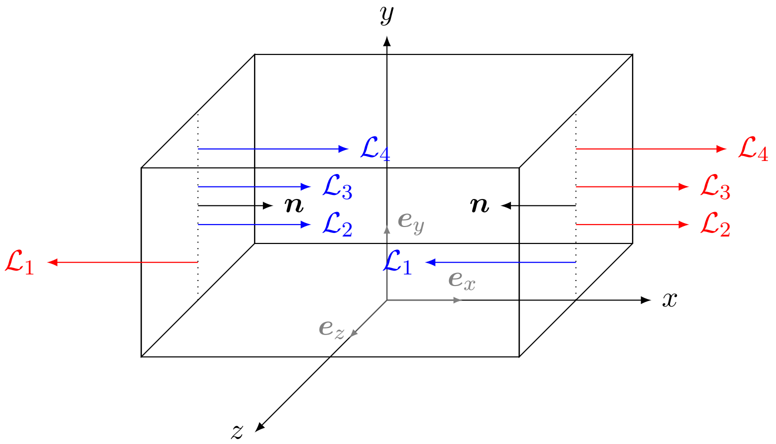

Figure 3.2. Sketch of the incoming (blue) and outgoing (red) waves in the case of a subsonic flow with $u > 0$

rearranged in several ways, for instance with time derivatives of primitive variables expressed as functions of wave strengths, $\mathcal{L}_i$:

$$\frac{\partial p}{\partial t} + \frac{1}{2}(\mathcal{L}_1 + \mathcal{L}_4) = 0 \tag{3.25}$$

$$\frac{\partial u}{\partial t} + \frac{1}{2\rho a}(\mathcal{L}_4 - \mathcal{L}_1) = 0 \tag{3.26}$$

$$\frac{\partial v}{\partial t} + \mathcal{L}_3 = 0 \tag{3.27}$$

$$\frac{\partial \rho}{\partial t} + \frac{1}{a^2}\left(\frac{1}{2}(\mathcal{L}_4 + \mathcal{L}_1) - \mathcal{L}_2\right) = 0 \tag{3.28}$$

Eqs. (3.25)–(3.28) are useful when at the boundary we want to impose a time variation of a quantity, for example constant pressure implies $\mathcal{L}_4 = -\mathcal{L}_1$. Analogous equations, reported in Appendix B, are valid for $y = L$ boundaries.

The values $\mathcal{L}_i$ for $i = 1, \dots, 4$ are imposed for incoming waves, whereas they depend only on information at and within the boundary for outgoing, therefore in this case $\mathcal{L}_i$ are computed by means of off-centered finite-difference schemes. A wave is incoming if $\lambda \boldsymbol{e}_x \cdot \boldsymbol{n} > 0$ and outgoing if $\lambda \boldsymbol{e}_x \cdot \boldsymbol{n} < 0$, with $\boldsymbol{e}_x$ the x-versor and $\boldsymbol{n}$ the inward normal of the boundary, as depicted in Fig. 3.2. Once each $\mathcal{L}_i$ has been determined (we will see in the following some implementations of several boundary conditions), Eqs. (3.21)–(3.24) reduce to a system of four linear equations for the following unknowns: $\partial\rho/\partial x$, $\partial u/\partial x$, $\partial v/\partial x$ and $\partial p/\partial x$. These derivatives of the primitive variables can be used to compute $\partial(\boldsymbol{F} - \boldsymbol{F}_\mu)/\partial x$.

While the analytical expression of $\partial \boldsymbol{F}_\mu/\partial x$ depends on the specific boundary conditions, as shown in [131], the dependence of the inviscid flux-vector is through the waves strengths $\mathcal{L}_i$. Thus,

$$\frac{\partial m}{\partial x} = d_1 \tag{3.29}$$

$$\frac{\partial (mu + p)}{\partial x} = ud_1 + \rho d_2 \tag{3.30}$$

$$\frac{\partial (qu)}{\partial x} = \rho d_3 + vd_1 \tag{3.31}$$

$$\frac{\partial (\rho u h)}{\partial x} = md_2 + \frac{1}{\gamma - 1} d_4 + qd_3 + \frac{1}{2}(u^2 + v^2) d_1 \tag{3.32}$$

where

$$d_1 = \frac{1}{a^2}\left[\mathcal{L}_2 + \frac{1}{2}(\mathcal{L}_1 + \mathcal{L}_4)\right] \tag{3.33}$$

$$d_2 = \frac{1}{2\rho a}(\mathcal{L}_4 - \mathcal{L}_1) \tag{3.34}$$

$$d_3 = \mathcal{L}_3 \tag{3.35}$$

$$d_4 = \frac{1}{2}(\mathcal{L}_4 + \mathcal{L}_1). \tag{3.36}$$

Substitution of Eqs. (3.29)–(3.32) into (3.1) enables to evolve the solution taking into account the presence of the boundary.

However, the flow has been assumed to be one-dimensional at the boundaries. The amplitude of the characteristic waves, $\mathcal{L}_i$, are instead affected by the transverse motion [132]. In fact, Eqs. (3.25)–(3.28) are the first two terms of the complete Euler equations written in primitive variables $\boldsymbol{W} = (\rho, u, v, p)^T$

$$\frac{\partial \boldsymbol{W}}{\partial t} + \boldsymbol{d} + \boldsymbol{F}\frac{\partial \boldsymbol{W}}{\partial y} = 0. \tag{3.37}$$

Hence, the transverse terms

$$\boldsymbol{F}\frac{\partial \boldsymbol{W}}{\partial y} = \begin{bmatrix} \frac{\partial(\rho v)}{\partial y} \\ v\frac{\partial u}{\partial y} \\ v\frac{\partial v}{\partial y} + \frac{1}{\rho}\frac{\partial p}{\partial y} \\ v\frac{\partial p}{\partial y} + \gamma p \frac{\partial v}{\partial y}, \end{bmatrix} \tag{3.38}$$

can be taken into account when the Riemann invariants amplitude are calculated. For instance, if the boundary condition imposes a constant pressure $\partial p/\partial t = 0$, then from the fourth component of Eq. (3.37) it follows

$$\mathcal{L}_1 = -\mathcal{L}_4 - v\frac{\partial p}{\partial y} - \gamma p \frac{\partial v}{\partial y}. \tag{3.39}$$

At the corner, $\boldsymbol{F}\partial \boldsymbol{W}/\partial y$ is influenced by the next boundary condition and its waves, incoming and outgoing waves, must be taken into account exactly as for the x-direction.

In the following, all the implemented boundary conditions are described. Moreover, several numerical test have been conducted in order to validate them and have been reported in the next section. Moreover, for the sake of simplicity, we will assume a positive boundary normal versor in the x-direction.

Adiabatic slip wall Slip walls are characterized by one inviscid condition: the normal velocity at the wall is zero. This implies that $\mathcal{L}_2 = \mathcal{L}_3 = 0$ because $\lambda_2 = \lambda_3 = 0$. Moreover, thanks to Eq. (3.26) $\mathcal{L}_4 = \mathcal{L}_1$, i.e. to the acoustic wave entering into the wall corresponds an equal acoustic wave coming from the wall. However, if transverse terms are considered, then the relation between the two acoustic waves is $\mathcal{L}_4 = \mathcal{L}_1 + 2\rho a v \partial u/\partial y$ and $\mathcal{L}_1$ is computed from interior points. The tangential viscous term is $\tau_{12} = 0$ [131].

Adiabatic no-slip wall At an adiabatic wall all the velocity components are zero. Hence, as in the slip wall $\mathcal{L}_2 = \mathcal{L}_3 = 0$ and $\tau_{12} = 0$. In addition, $\mathcal{L}_4 = \mathcal{L}_1$ even when transverse terms are taken into account. The outgoing acoustic wave is computed from the interior points. A more sophisticated condition has been proposed by Cuif Sjöstrand, D'Angelo, and Albin [133] but it improves only stability, therefore it is not discussed and implemented in this work.

Vibrating isothermal wall Imposing the two velocity components and the temperature at the wall, $u = u(x,t)$, $v = v(x,t)$ and $T = T(x,t)$, only density must be evolved in time according to the Navier-Stokes equations. Thanks to Eq. (3.26), we obtain $\mathcal{L}_4 = \mathcal{L}_1 - 2\rho a du/dt$. If $u < 0$ then $\mathcal{L}_2$ and $\mathcal{L}_3$ are outgoing waves and are computed from the interior points, whereas if $u > 0$ then

$$\mathcal{L}_2 = \rho a^2 \frac{\partial T}{\partial t}\frac{1}{T} + \frac{1}{2}(\gamma - 1)(\mathcal{L}_4 + \mathcal{L}_1) \quad \text{and} \quad \mathcal{L}_3 = \frac{\partial v}{\partial t}.$$

Isothermal inflow Inflow conditions are widely used in numerical computational, for instance they are at basis of jets simulations. In the present work, we have experimentally characterized the injection from a porous material and the most appropriate inflow condition to simulate this phenomenon is to impose mass flow and temperature. As we have shown in Sec. 2.3.1 that the inflow from a porous plate is far from being constant in time and space, we assume $m = m(x,t)$, $q = q(x,t)$ and $T = T(x,t)$. The only variable that must be computed is the density and hence no viscous relation is needed. Being an inflow, the only outgoing wave is $\mathcal{L}_1$, the others must be imposed by means of LODI relations. Combining Eqs. (3.25)–(3.28), the following relations can be obtained

$$\begin{cases} \frac{\partial m}{\partial t} + \frac{1}{a}\left\{M\mathcal{L}_2 + \frac{1}{2}\left[(M-1)\mathcal{L}_1 + (M+1)\mathcal{L}_4\right]\right\} = 0 \\ \frac{\partial q}{\partial t} + \frac{v}{a^2}\left[\frac{1}{2}(\mathcal{L}_4 + \mathcal{L}_1) - \mathcal{L}_2 - \rho\mathcal{L}_3\right]\frac{\partial T}{\partial t} + \frac{T}{\rho a^2}\left[-\mathcal{L}_2 + \frac{1}{2}(\gamma - 1)(\mathcal{L}_4 + \mathcal{L}_1\right] = 0, \end{cases} \tag{3.40}$$

thus

$$\begin{cases} \mathcal{L}_4 = -\frac{2a}{M\gamma+1}\frac{\partial m}{\partial t} - \frac{2M\rho a^2}{M\gamma+1}\frac{1}{T}\frac{\partial T}{\partial t} - \frac{M\gamma-1}{M\gamma+1}\mathcal{L}_1 \\ \mathcal{L}_2 = \frac{\rho a^2}{T}\frac{\partial T}{\partial t} + \frac{1}{2}(\gamma - 1)(\mathcal{L}_4 + \mathcal{L}_1) \\ \mathcal{L}_3 = -\frac{1}{\rho}\frac{\partial q}{\partial t} - \frac{v}{\rho a^2}\left[\frac{1}{2}(\mathcal{L}_4 + \mathcal{L}_1) - \mathcal{L}_2\right] \end{cases} \tag{3.41}$$

Analogously, if u and v are imposed, instead of m and q, from Eq. (3.26) and (3.27) we have

$$\begin{cases} \mathcal{L}_4 = \mathcal{L}_1 - 2\rho a\frac{\partial u}{\partial t} \\ \mathcal{L}_3 = -\frac{\partial v}{\partial t} \end{cases} \tag{3.42}$$

and $\mathcal{L}_2$ remains the same of Eq. (3.41).

Adiabatic outflow Being an outflow condition, the two waves of velocity $\lambda_2 = \lambda_3$ and the acoustic one with velocity λ_1 are outgoing waves and are computed from interior points. As $p \equiv p_{\text{out}}$, thanks to Eq. (3.25) the incoming wave is $\mathcal{L}_4 = -\mathcal{L}_1$ or $\mathcal{L}_4 = -\mathcal{L}_1 - v\frac{\partial p}{\partial y} - \gamma p\frac{\partial v}{\partial y}$.

Non-reflecting outflow Outflow conditions are crucial in numerical computations, especially when the boundary of the computational domain is near the region of interest. It is important that an outflow condition does not influence the flow within the domain, in particular it is desirable that waves going through this kind of boundaries are completely absorbed and that boundary constraints do not emit waves too. Being an outflow, three of the four waves are outgoing waves, hence can be computed from interior points. A perfectly non-reflecting boundary condition should have incoming waves of zero amplitude, hence Thompson [130] proposed

$$\mathcal{L}_4 = 0. \tag{3.43}$$

However, perfectly non-reflecting boundaries may lead to ill-posed problems as pointed out by Rudy and Strikwerda [134] and shown in the next section. In fact, while in real problems the mean pressure information is contained in the surrounding space far from the region of interest, using Eq. (3.43) this information is absent. Rudy and Strikwerda [134] proposed a relaxed condition emphasizing the convergence to the steady-state solution of the problem

$$\mathcal{L}_4 = \alpha(p - p_{\text{out}}), \tag{3.44}$$

where $\alpha = \beta(1 - M^2)a/L$, with β a constant and L the characteristic size of the domain, is the coefficient so that the transient solution decays most rapidly. This linear relaxation term, RHS of Eq. (3.44), results in a non-zero reflection for acoustic waves [135]. Polifke, Wall, and Moin [135] showed how to correct Eq. (3.44) in order to provide a nearly non-reflecting—for plane acoustic waves with normal incidence—for low frequencies. The principle is to identify the acoustic wave that is approaching the boundary and subtract its contribute to the incoming wave $\mathcal{L}_4$, i.e.

$$\mathcal{L}_4 = \alpha(p - \rho a g - p_{\text{out}}), \tag{3.45}$$

where g is the approaching acoustic wave amplitude. In order to estimate this amplitude, Polifke, Wall, and Moin [135] and Kopitz, Bröcker, and Polifke [136] proposed the following equation

$$g = \frac{1}{2}\left(\frac{\delta p}{\rho c} - \delta u\right) \tag{3.46}$$

with $\delta p = p - \bar{p}$, $\delta u = u - \bar{u}$ and overbar quantities are averaged over a sample plane near the boundary.

Periodic A useful condition for preliminary test is the periodic boundary condition. It is extremely easy to implement and does not require any characteristic direction because it is a purely geometrical constraint. Hence, the variables required at the boundary are picked from the associated edge.

3.3 Validation

In this section several test are presented in order to analyze separately all the implemented features, in particular the boundary conditions. Some of them utilize the geometrical configuration of the experimental apparatus, i.e. a nearly closed rectangular channel.

Two preliminary test to check that no blunders have been done during the implementation of the numerical code are presented. The computational domain is a rectangle $D = [-7.5, 7.5] \times [-1, 1]$ with slip wall condition on the two long sides and periodic condition on the other two sides. The initial state is a pressure pulse

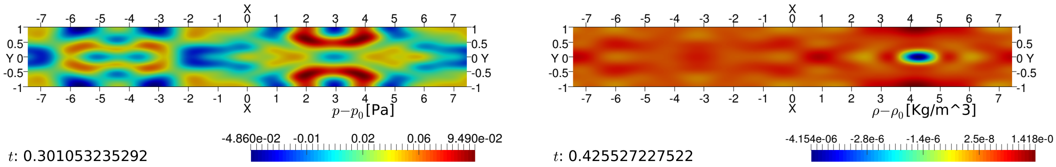

(a) **(b)**

Figure 3.3. Acoustic pattern **(a)** and density spot **(b)** for the preliminary test computation

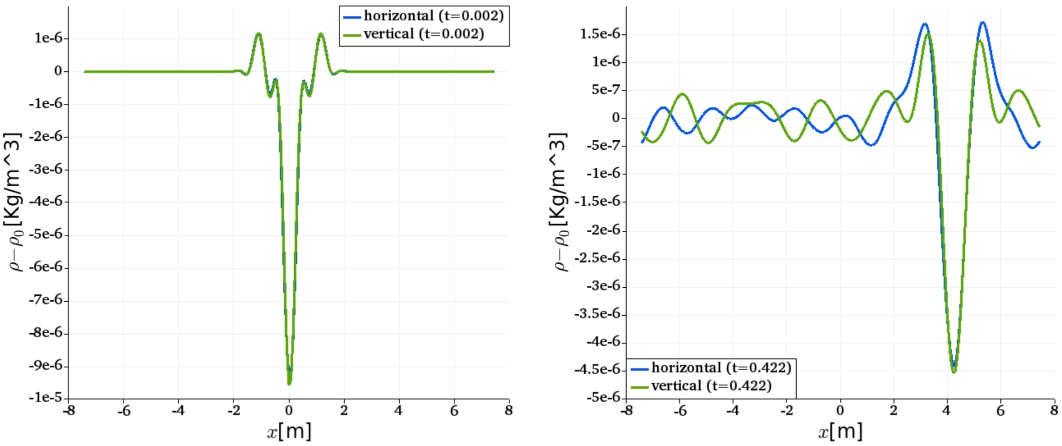

(a) **(b)**

Figure 3.4. Density perturbation along the axis of D in the two computations: $D = [-7.5, 7.5] \times [-1, 1]$ (horizontal) and $D = [-1, 1] \times [-7.5, 7.5]$ (vertical); at two successive times: $t = 0.002\,\mathrm{s}$ **(a)** and $t = 0.422\,\mathrm{s}$ **(b)**

into a constant velocity field:

$$\begin{bmatrix} \rho_0 \\ u_0 \\ v_0 \\ p_0 \end{bmatrix} = \begin{bmatrix} 1 \\ 10 \\ 0 \\ 86100 + 1.3e^{-\frac{x^2+y^2}{0.045}} \end{bmatrix}. \tag{3.47}$$

The computation is inviscid and the mesh is elongated in the x-direction because a grid of 200 × 200 points has been adopted. The pressure peak generates a round acoustic wave that is soon reflected by the two close walls and a typical acoustical pattern has been found in the whole domain, see Fig. 3.3a. Moreover, a rarefied round region is generated at the origin and convected by the velocity field (Fig. 3.3b). This density spot has been used to compare the same computation in the y-direction: $D = [-1, 1] \times [-7.5, 7.5]$, $u = 0$ and $v = 10$; in order to verify that the implementation is the same in the two directions. The two peaks in Fig. 3.4 are equivalently advected

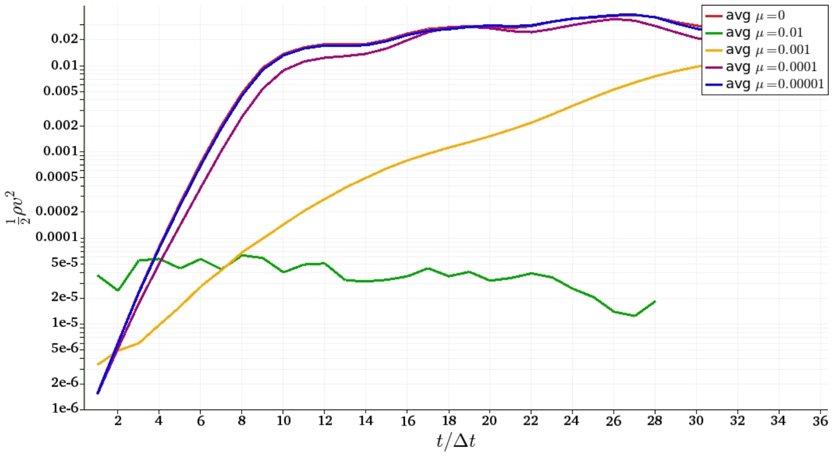

Figure 3.5. Evolution of kinetic energy of the transverse velocity component averaged over the computational domain

in both the two computations. The small oscillations in Fig. 3.4b differ between the two computations likely because, being due to high-frequency oscillations, they are much more sensible to dispersion error.

In order to asses the capability to simulate the shear layer, several test of the Kelvin-Helmholtz instability have been conducted [137]. The computational domain is the unitary square $D = [0, 1]^2$ with periodic boundary conditions on each opposite side, therefore topologically equivalent to a torus. The initial state has constant pressure in D, while two layers of different density streams with opposite velocity:

$$\begin{bmatrix} \rho_1 \\ u_1 \\ v_1 \\ p_1 \end{bmatrix} = \begin{bmatrix} 1 \\ 5 \\ 0 \\ 2.5 \end{bmatrix} \quad \text{and} \quad \begin{bmatrix} \rho_2 \\ u_2 \\ v_2 \\ p_2 \end{bmatrix} = \begin{bmatrix} 2 \\ -5 \\ 0 \\ 2.5 \end{bmatrix}. \tag{3.48}$$

A study for different viscosity has been carried on: $\mu = 0.01$, 0.001, 0.0001, 0.00001 and 0. The evolution of kinetic energy of the transverse velocity $\frac{1}{2}\rho v^2$ is analyzed, see Fig. 3.5, and it is comparable with the result obtained by Harang et al. [138]. A computational grid of 128×128 has been adopted. Also the density distributions over the computational domain D are reported in Fig. 3.6. For a given viscosity, $\mu = 0.0001$, we have also reported the density distribution for increasing resolution: 128×128, 256×256, 512×512 and 1024×1024; see Fig. 3.7. For the sake of completeness a three-dimensional simulation has been reported in Fig. 3.8, where density and Q-contours colored with vorticity are reported for two successive times in order to show the evolution of the shear.

A further test involving the shear layer is presented. In particular the wake of

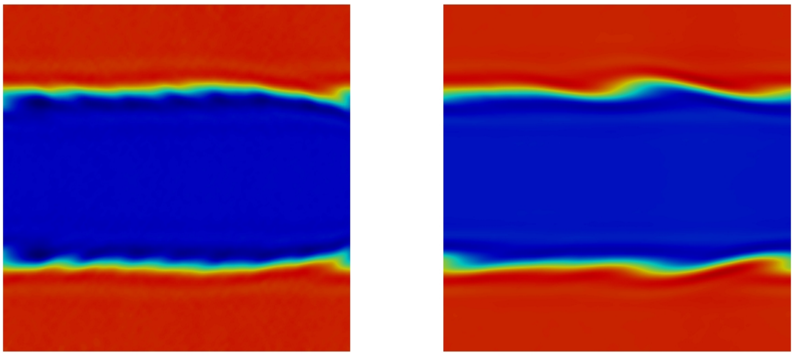

(a) $\mu = 0.01$ **(b)** $\mu = 0.001$

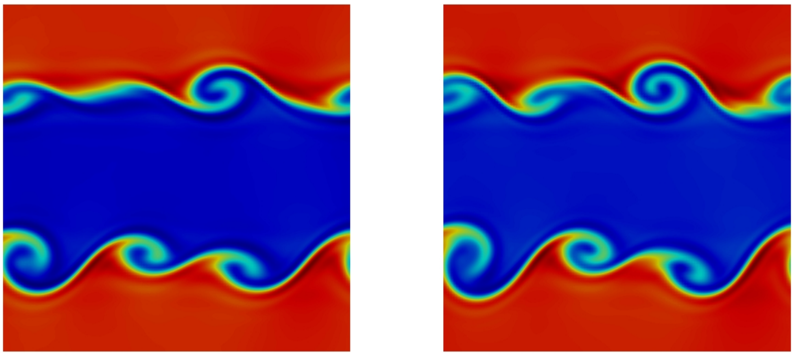

(c) $\mu = 0.0001$ **(d)** $\mu = 0.00001$

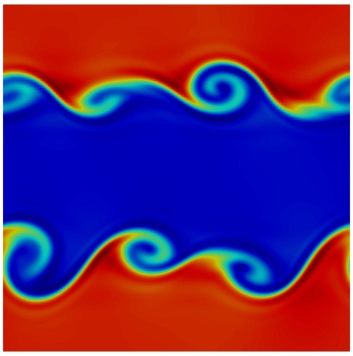

(e) $\mu = 0$

Figure 3.6. Density distribution at $t/\Delta t = 10$, which corresponds to $t \approx 1.44\,\mathrm{s}$, of the Kelvin-Helmholtz distribution for different viscosity

a bluff-body is analyzed. The computational domain is $D = [-0.5, L] \times [-1, 1] - [-0.1, 0.1]^2$, where $L = 2.5$ or 4. and the square of side 0.1 is the body with slip wall condition on each side. The upstream edge of D is an isothermal inflow and

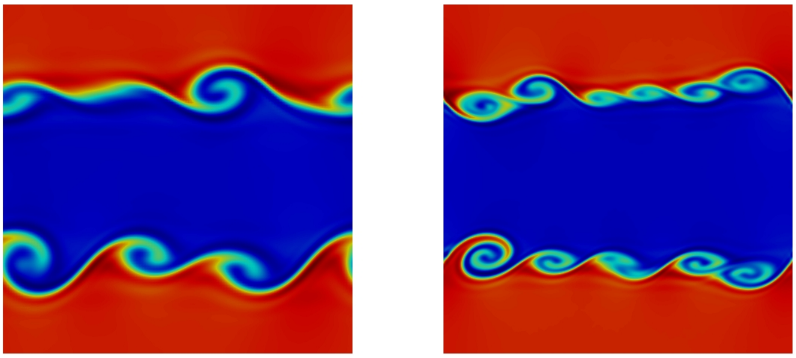

(a) 128×128 **(b)** 256×256

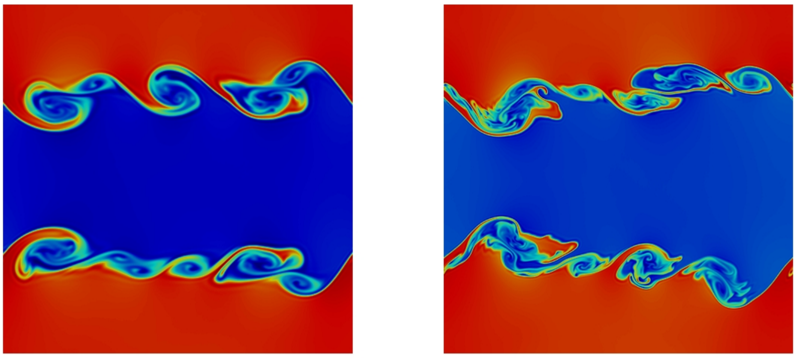

(c) 512×512 **(d)** 1024×1024

Figure 3.7. Density distribution at $t \approx 1.44\,\mathrm{s}$, of the Kelvin-Helmholtz distribution for different resolutions

the other three external sides are non-reflecting outflow with Eq. (3.45). With the inflow condition a free stream of velocity $\bar{u} = 30\,\mathrm{m\,s^{-1}}$ is obtained, therefore the initial state in D is

$$\begin{bmatrix} \rho_0 \\ u_0 \\ v_0 \\ p_0 \end{bmatrix} = \begin{bmatrix} 1 \\ 30 \\ 0 \\ 86100 \end{bmatrix}. \tag{3.49}$$

Both viscosity and grid resolution have been varied and summarized in Tab. 3.4 It should be pointed out that, when viscosity is taken into account, the Reynolds number based on the stream velocity, $\bar{u}$, and the width of the body, W, is $\mathrm{Re} \approx 850$, hence the adequate grid resolution would be such that the grid Reynolds number, i.e. $\mathrm{Re}_h = uh/\mu$ with h the characteristic dimensions of the computational cell, is around the unity. In the present case $\mathrm{Re}_h \approx 60$, hence the computation is under-resolved in a DNS sense. However, the shedding of vortices in the wake of a bluff-body is not

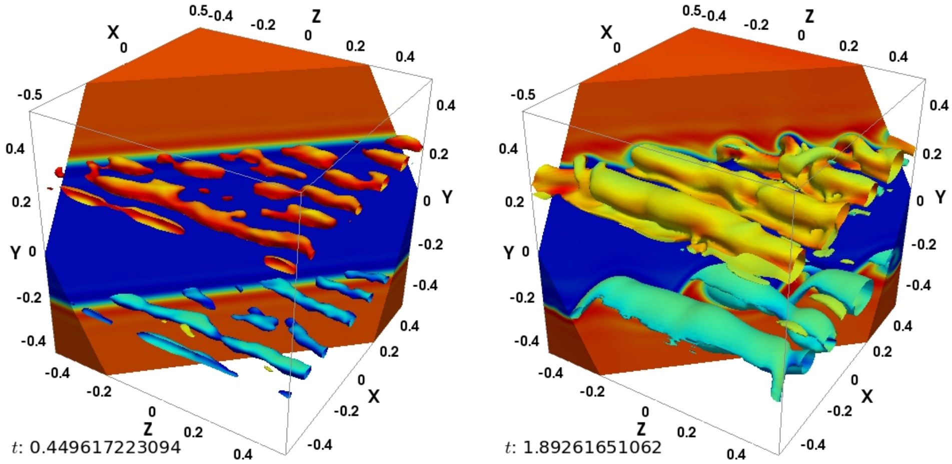

(a) (b)

Figure 3.8. Three-dimensional Kelvin-Helmholtz instability. Density and Q-contours colored with vorticity at two successive times

Test	μ	Resolution	L
1	0	128×256	2.5
2	0	64×128	2.5
3	0.007	64×128	2.5
4	0.007	64×152	4.5

Table 3.4. Description of bluff-body simulations

related to small-scale phenomena and hence is well-resolved in all the simulations presented here. In addition the physical diffusion, related to the parameter μ does not play any role due to the large grid Reynolds number, but the resolution changes a bit the results nonetheless. In fact, the distance between the vortices is slightly smaller when the finer grid is adopted, i.e. $\delta = 0.41\,\mathrm{m}$ and $0.46\,\mathrm{m}$ respectively for Test 1 and Test 2, see Fig. 3.9 and Fig. 3.10. However this leads to a Strouhal number

$$\mathrm{St} = \frac{fW}{\bar{u}} = \frac{\tilde{u}}{2\delta}\frac{W}{\bar{u}} = \begin{cases} \dfrac{30.81\,[\mathrm{m/s}]}{0.82\,[\mathrm{m}]}\dfrac{0.2\,[\mathrm{m}]}{30\,[\mathrm{m/s}]} = 0.25, & \text{Test 1} \\ \dfrac{29.21\,[\mathrm{m/s}]}{0.92\,[\mathrm{m}]}\dfrac{0.2\,[\mathrm{m}]}{30\,[\mathrm{m/s}]} = 0.21, & \text{Test 2} \end{cases} \tag{3.50}$$

where $\tilde{u} = \frac{1}{2.5-0.3}\int_{0.3}^{0.5} dx \left(\lim_{T\to\infty} \frac{1}{T}\int_0^T dt\, u(x,0,t)\right)$ is an estimation of the advection velocity of the vortices behind the body, which is in the range 0.16–0.27 for $250 < \mathrm{Re} < 10^6$, [139, 140].

In order to verify the implementation of the wall boundary conditions: slip and no-slip; a channel $D = [0, 0.24] \times [-0.02, 0]$ has been discretized with a 33×257 points grid. The flow is imposed with an isothermal inflow condition with imposed

(a) Test 1 **(b)** Test 2

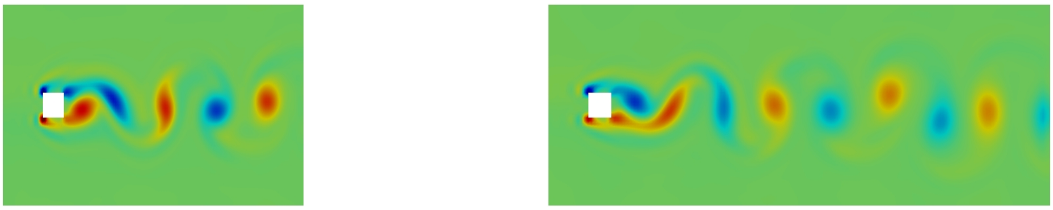

(c) Test 3 **(d)** Test 4

Figure 3.9. Wake behind a bluff-body for the four test reported in Tab. 3.4

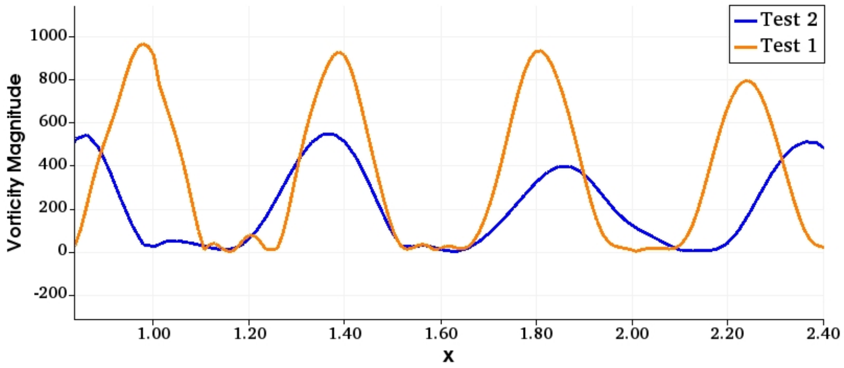

Figure 3.10. Vorticity magnitude variation with spanwise location

velocity, as in the previous test of the bluff-body, at the head end of the channel ($x = 0$) and the non-reflecting outflow condition with Eq (3.44) is imposed at the aft end ($x = 0.24$). The wall condition is applied on the two other sides. In Fig. 3.11 an instantaneous profile and a time averaged profile of u has been compared for the two boundary conditions. Note that the instantaneous profile with no-slip wall is coincident with the Poiseuille solution. As the outflow is partially reflecting, as explained in the previous section, the velocity field is actually unsteady and all the contributes of acoustic oscillations deforms the time-averaged profile.

Let us consider the outflow boundary conditions and, for brevity, let us name the three conditions given by Eqs. (3.43), (3.44) and (3.45) respectively as Non-reflective, Strikwerda and Polifke. The domain of computation is the square $D = [-5, 5]^2$ and

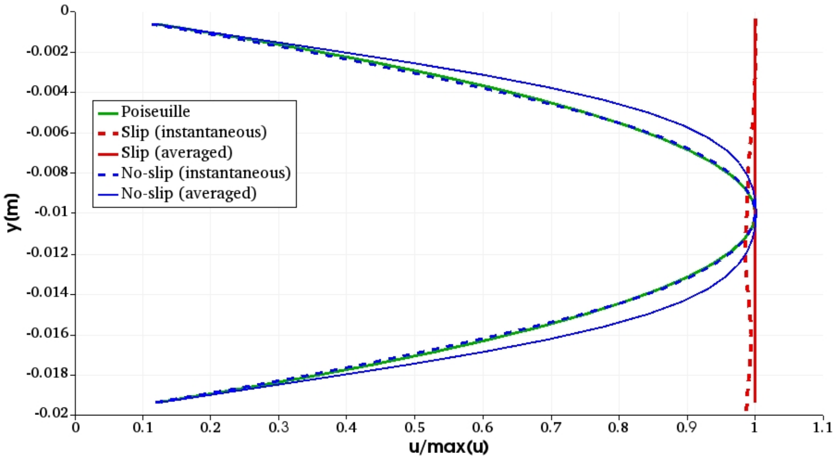

Figure 3.11. Horizontal velocity profile normalized with respect to the maximum value, $u/\max_y u$

an acoustic wave is generated with a gaussian pressure peak

$$\begin{bmatrix}\rho_0\\ u_0\\ v_0\\ p_0\end{bmatrix} = \begin{bmatrix}1\\ 0\\ 0\\ 86100 + 10e^{-10(x^2+y^2)}\end{bmatrix} \tag{3.51}$$

as shown in Fig. 3.12. This simulation has been repeated with the three outflow boundary conditions listed above and the pressure captured by a probe located at $(3.75, 0) \in D$ is reported in Fig. 3.13a. After a high peak generated by the traveling wave, which is present in all the three computations, we observe three different behaviors. The non-reflective condition profile does not present any oscillation because no waves come back but the predicted ill-posedness of the problem leads to a linear pressure drift. Both Strikwerda and Polifke methods are well-posed: the former presents small oscillations caused by partially reflected waves on the four sides of D that goes back and forth, whereas the latter completely absorbs the wave and hence shows a constant level of pressure. It is noteworthy that the pressure drift does depend on the grid resolution, as shown in Fig. 3.13b, therefore it is plausible that the numerical viscosity plays a role in this phenomenon.

Geometrical configurations that are confined by rigid walls are more susceptible to acoustic perturbations than open computational domains where, in spite of the difficulties due to non-reflective boundary conditions, acoustical waves can leave the domain and do not provide energy to the system that, instead, may lead to resonance and amplification. In order to assess the behavior of the present computational code treating acoustical waves in confined regions, an investigation of a small

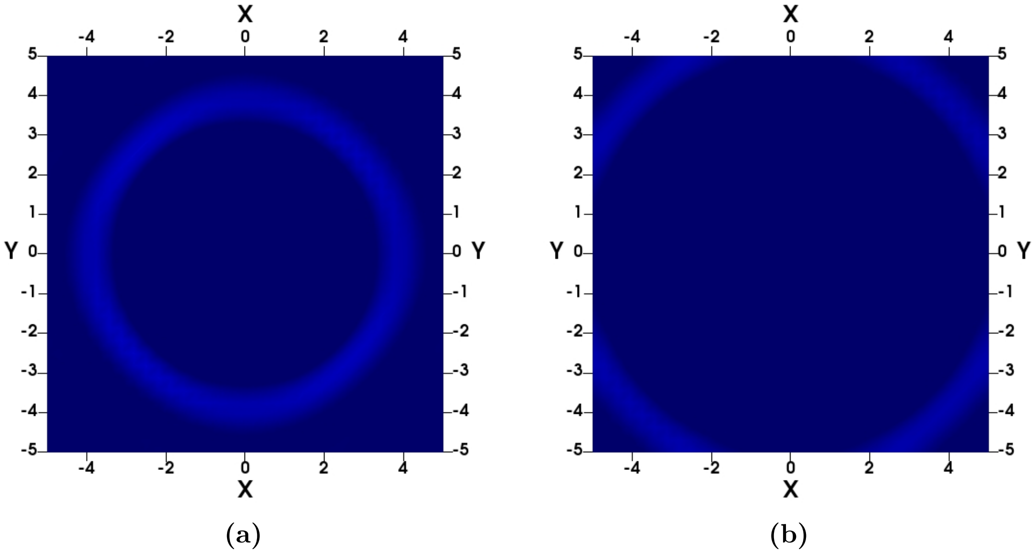

(a) (b)

Figure 3.12. Pressure perturbation at two successive time generated by the initial state in (3.51) with non reflective boundary conditions

perturbed closed tube has been carried on. Let us consider a two-dimensional tube $D = [-0.5, 0.5] \times [-0.05, 0.05]$ with slip wall boundary condition everywhere except for $x = -0.5$ where vibrating wall condition is employed with $u(x, t) = \sin(2\pi f_{\mathrm{w}} t)$. Since the initial pressure and density are respectively $p_0 = 86100$ and $\rho_0 = 1$, then the speed of sound is $a_0 = \sqrt{\gamma p_0/\rho_0} \approx 347\,\mathrm{m\,s^{-1}}$ with $\gamma = 1.4$. Hence, the proper longitudinal acoustic frequencies of the tube are

$$f_n = n f_1 = n\frac{a_0}{2L} = n175, \tag{3.52}$$

where $L = 1$ is the length of the channel. When $f_{\mathrm{w}} = f_1$, then resonance occurs and non-linear phenomena appear, see Fig. 3.14 where the spectrum is reported and Fig. 3.15a where the time evolution of pressure is plotted. If $f_{\mathrm{w}} = 200 = 1.14 f_1$, the beating phenomenon is observed (Fig. 3.15b), whereas if $f_7 < f_{\mathrm{w}} < f_8$ the nearest natural frequencies are amplified (Fig. 3.14) but the energy is not enough to generate resonance, in fact oscillations are of the order of the 0.6% of the total pressure as shown in Fig. 3.15c. This proves that the numerical code is able to deal with acoustical phenomena in bounded regions.

The next step to assess the capability of the code to well approximate acoustical phenomena within a geometry like the one of the experimental apparatus is to consider a closed-open channel. Therefore, let be D the same domain of the previous test but with the aft end side open, where the Polifke condition has been employed.

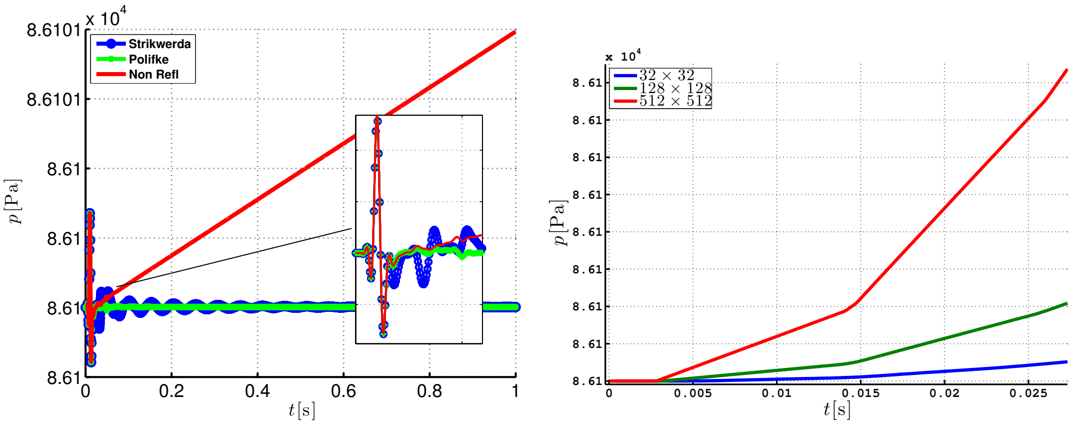

(a) **(b)**

Figure 3.13. Pressure variations with time for three different outflow boundary conditions hit by an acoustic wave **(a)** and pressure drift for different grid resolutions **(b)**

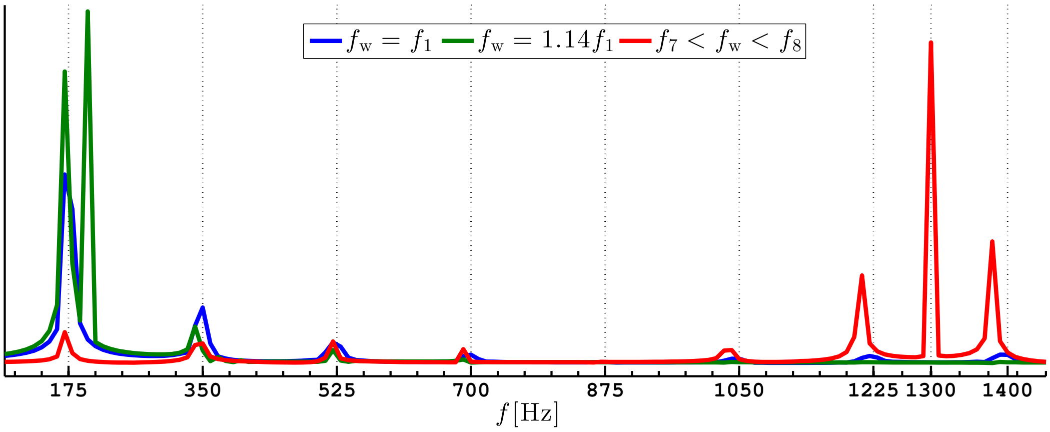

Figure 3.14. Normalized spectrum of pressure in a perturbed tube with frequency f_w

Note that in closed-open tube, the natural frequencies are halved, i.e.

$$f_n = nf_1 = n\frac{a_0}{4L} = n86, \qquad \text{for } n \text{ odd.} \tag{3.53}$$

Analogously to the closed tube, several frequencies have been tested: $f_w = 2f_1$, $f_w = f_1$ and $f_w = f_3$. Again when the wall frequency matches a natural frequency, resonance occurs. Since the resonance phenomenon is a redistribution of energy into the frequency space, i.e. the natural frequencies drain energy from the whole system, it may be used to study the effect of (numerical and physical) dissipation on the system. It should be noted that the numerical dissipation is governed by two parameters: the grid spacing, h, and the filter strength, σ. In Tab. 3.5 we have summarized all the parameters adopted. In Fig. 3.17a, for the resonant frequency $f_w = f_1$, Test 1 and Test 2 are superposed, hence the filtering process dominates with

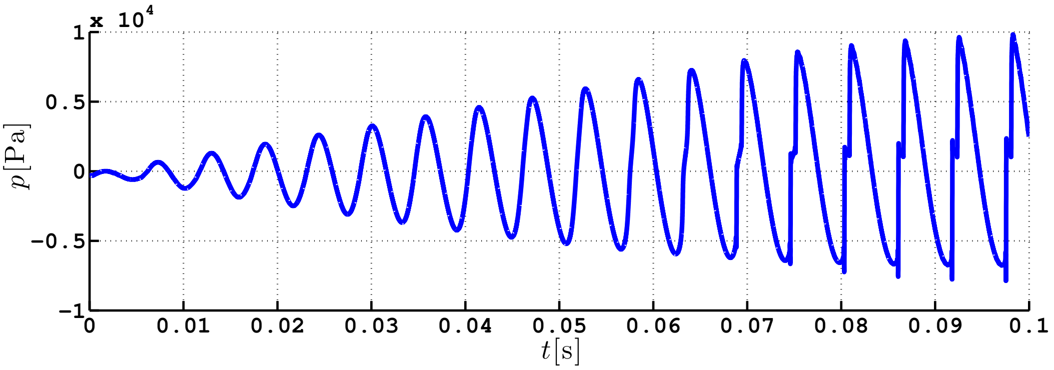

(a) $f_{\mathrm{w}} = f_1$

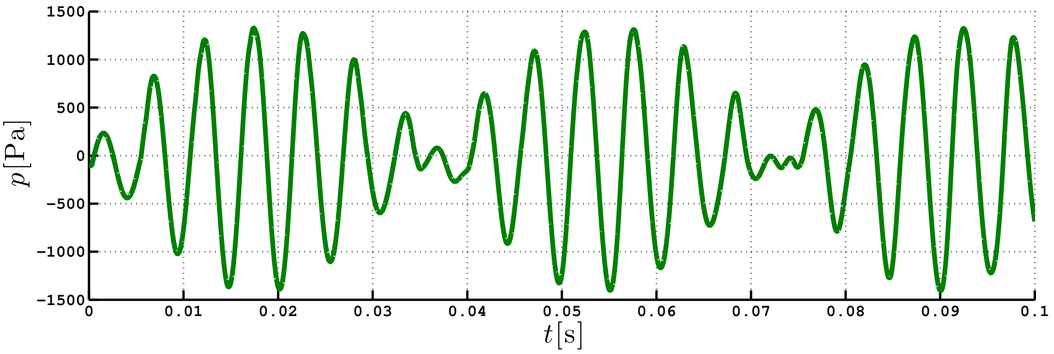

(b) $f_{\mathrm{w}} = 200 = 1.14 f_1$

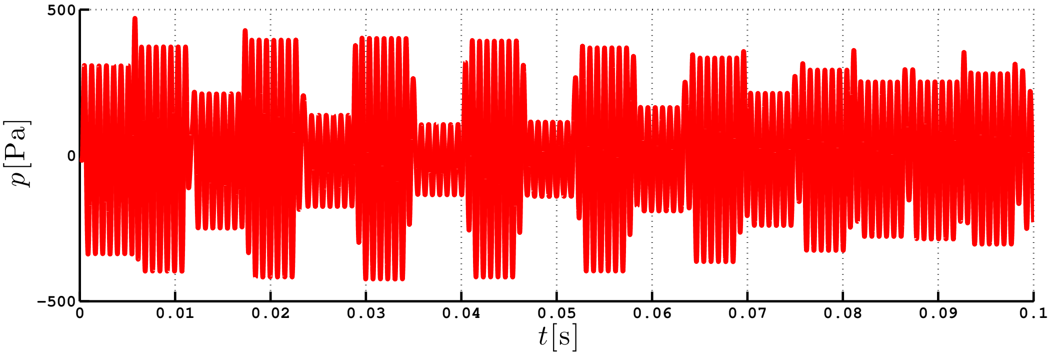

(c) $f_7 < f_{\mathrm{w}} < f_8$

Figure 3.15. Pressure variations with time in a perturbed closed tube with frequency f_w

respect to the physical viscosity. Reducing the filter strength, Test 3, the oscillation amplitude drastically increases so $\sigma = 0.6$ introduces an excessive damping and should not be used. However, with such a low dissipation the numerical instability yields a jagged profile that becomes instead smooth rising μ in Test 4 (see Fig. 3.17b). In order to get the correct result for small viscosity, it is necessary to increase the grid resolution as in Test 5. As a consequence of a smaller viscosity the amplitude of resonance is higher because less energy is drained by dissipation. It should be

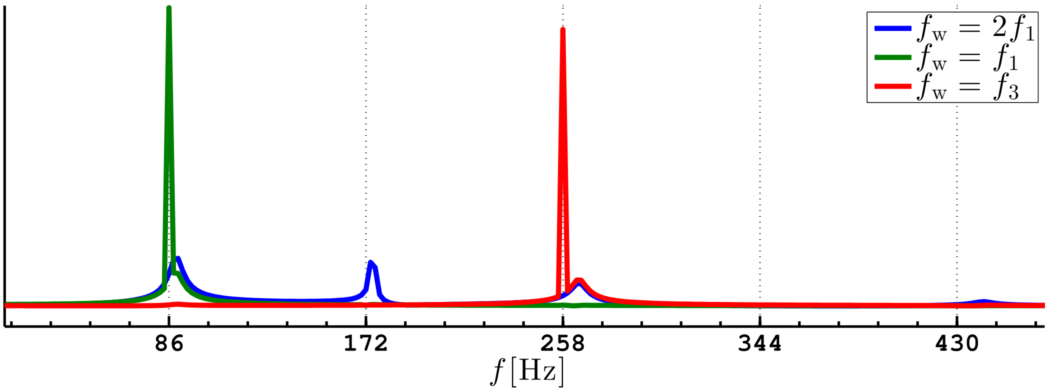

Figure 3.16. Normalized spectrum of pressure in a perturbed closed-open tube with frequency f_w

Test	μ	σ	$h \approx$	Outflow BC
1	10^{-4}	0.6	0.004	Polifke
2	10^{-2}	0.6	0.004	Polifke
3	10^{-4}	0.1	0.004	Polifke
4	10^{-2}	0.1	0.004	Polifke
5	10^{-4}	0.1	0.0004	Polifke
6	10^{-4}	0.05	0.0004	Polifke
7	10^{-4}	0.6	0.004	Strikwerda
8	10^{-4}	0.6	0.004	$p = p_{\mathrm{out}}$

Table 3.5. Parameters adopted in the study of the closed-open tube

pointed out that an even smaller filter strength can be used as in Test 6 leading to an even smaller damping but this is not safe for more complex simulations. A further interesting comparison is between outflow conditions. In Fig. 3.18 the pressure evolution has been reported for three different outflow conditions. The different amplitude is due to the different level of energy provided to the system. In fact, Test 7 contains the energy provided by small reflections due to a non perfect absorbing boundary condition, as shown before, and Test 8 has an even higher amplitude because imposing the pressure at the outlet is not actually a non-reflecting boundary but only and outflow condition.

3.4 Close-open simulations

In the present section, simulations of the experimental apparatus presented in Chapter 2, by means of the numerical code validated in the previous section, are presented.

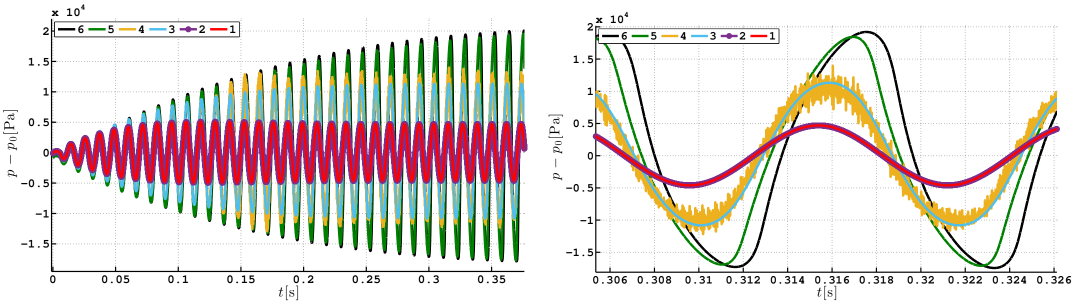

(a) **(b)**

Figure 3.17. Pressure oscillations in resonance phenomena with varying parameters

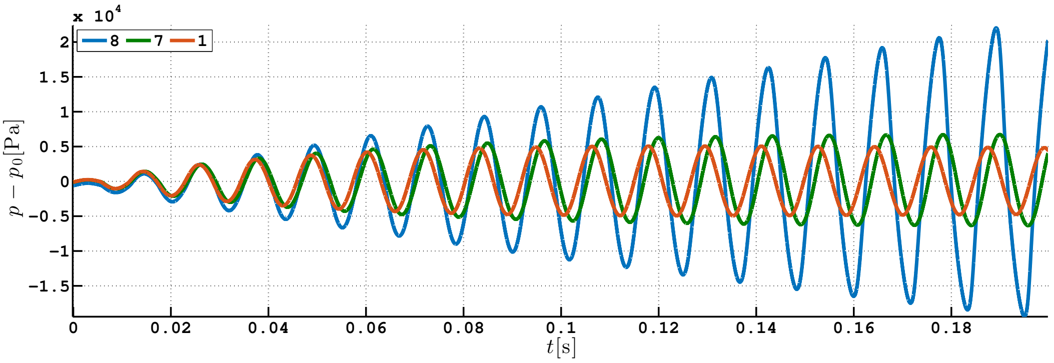

Figure 3.18. Pressure oscillations in resonance phenomena with varying outflow conditions

3.4.1 Straight configuration

The computational domain is the channel $D = [0, 0.24] \times [-0.02, 0]$, which corresponds to the two-dimensional plane of measurements. At first, a test of convergence has been carried on. The following grid resolutions are considered: 16×128, 32×256 and 64×512 with slip wall condition on the head end and on the top wall, isothermal inflow with mass flow imposed to $\rho v = 0.075\,\mathrm{kg/m^2s}$ and $T = 300\,\mathrm{K}$ on the bottom wall and Polifke outflow with $p_{\mathrm{out}} = 86\,100\,\mathrm{Pa}$ on the aft end. In Fig. 3.19a–3.19b the convergence of the velocity profile of u and v to the Taylor-Culick solution is shown. In addition, the pressure profile along the centerline, normalized with respect to its value at the head end is shown in Fig. 3.19c. It is noteworthy that the steady state pressure levels, visible after a transient initial phase characterized by non linear phenomena, are different for different resolutions and decrease towards the given value $p_{\mathrm{out}} = 86100$ increasing the resolution, see Fig. 3.20.

Analogously, a convergence test has been reported with the adiabatic outflow and no-slip wall condition. In this case, the coarsest grid (16×128) shows beating (see Fig. 3.21a) on the vertical natural frequencies (see Fig. 3.21b), i.e. $f_n = a_0/(2H)$ with H the height of the channel, probably because of stability problems at the early

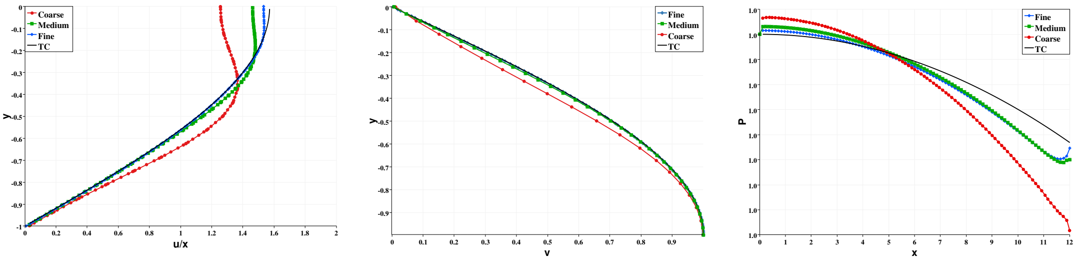

(a) (b) (c)

Figure 3.19. Velocity and pressure profiles for different grid resolutions compared with the Taylor-Culick profile

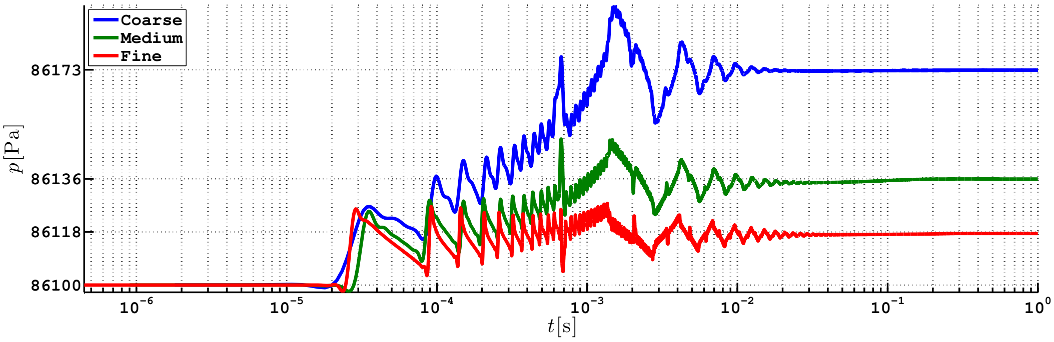

Figure 3.20. Aft end pressure evolution for different grid resolution with Polifke outflow condition

times of the simulation when a transient non-linear phase occurs exciting higher frequencies. The unsteady behavior of the coarse grid solution is also evident looking at the time averaged vertical velocity profile and the pressure profile along the axis of the channel (Fig. 3.22b-3.22c). The time history of pressure for the medium and fine grids, instead, shows decaying oscillations (Fig. 3.21a) on the natural horizontal frequencies (Fig. 3.21b). As shown by the velocity profiles reported in Fig. 3.22a-3.22b, despite convergence to the analytical viscous solution of the steady Navier-Stokes is evident, the numerical solutions are still grid dependent. This is reasonable because the cell Reynolds number for the fine grid is $\mathrm{Re}_h \approx 2$.

After these preliminary test, the objective of this section is to reproduce numerically the experimental measurements described in the previous chapter. In order to do this, the following simulation has been performed: a jet-like inflow condition. A grid of 100×1200 points has been adopted leading to a cell Reynolds number $\mathrm{Re}_h \approx 1$. The no-slip wall and adiabatic outflow condition have been employed on the other three sides of the computational domain.

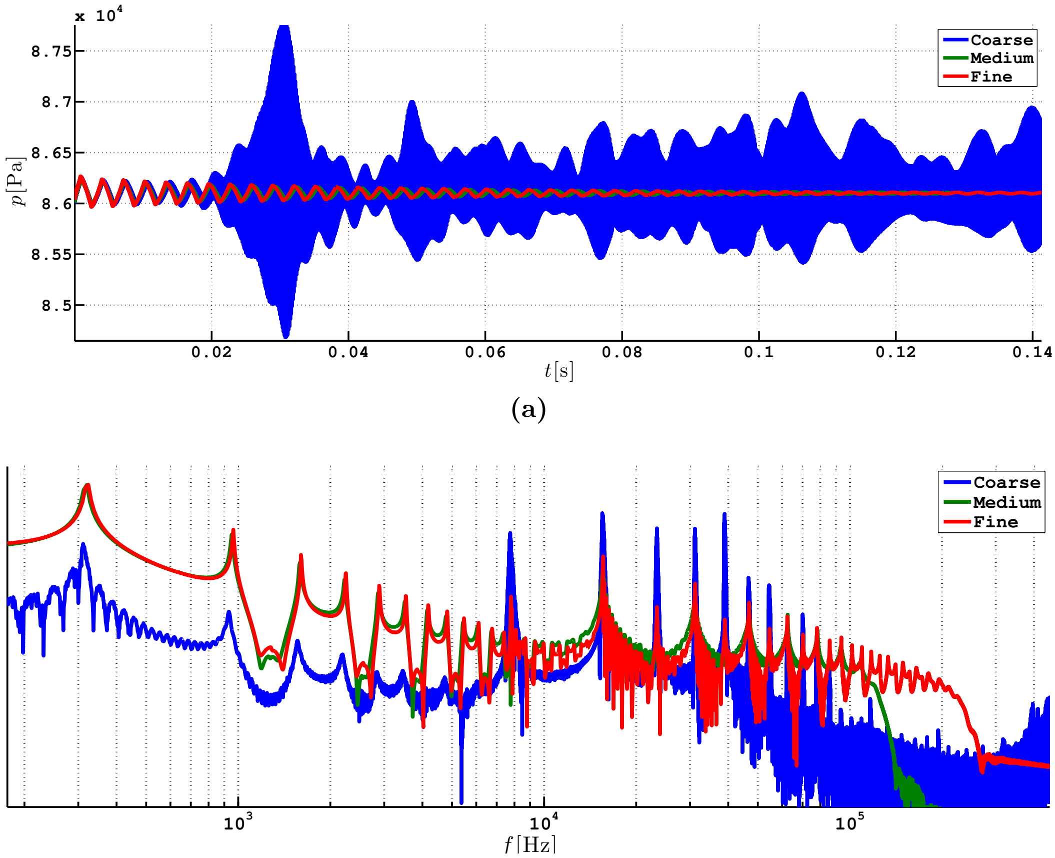

(a)

(b)

Figure 3.21. Head end pressure evolution for different grid resolution with adiabatic outflow condition

The jet-like pattern at the inflow condition has been simulated imposing

$$\rho u = 0.08(1 + \sin(kx)\cos(\omega t)) \tag{3.54}$$

with $k = 400 \times 2\pi/L$ in order to obtain a spatial pattern similar to that in Fig. 2.10e, which provides an injection velocity equal to $0.08\,\mathrm{m\,s^{-1}}$. Moreover, the perturbation is modulated in time ensuring constant addiction, i.e.

$$\frac{d}{dt}\int_0^L \rho u \, dx \equiv 0. \tag{3.55}$$

The time averaged velocity profiles of u and v, reported in Fig. 3.23, match the steady state solution of the Navier-Stokes equations and does not show any shape modification due to turbulent transition. Nevertheless, the turbulence intensity profile, TI, has a pronounced peak in a region near the injecting wall (Fig. 3.24a), according to the results obtained by Laboureur, Tóth, and Anthoine [118] and Ya-

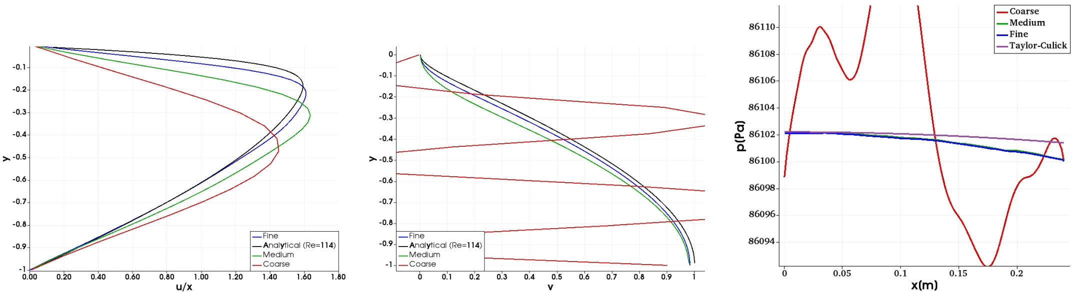

(a) **(b)** **(c)**

Figure 3.22. Velocity and pressure profiles for different grid resolutions compared with the steady state solution of the Navier-Stokes equations and the Taylor-Culick profile respectively

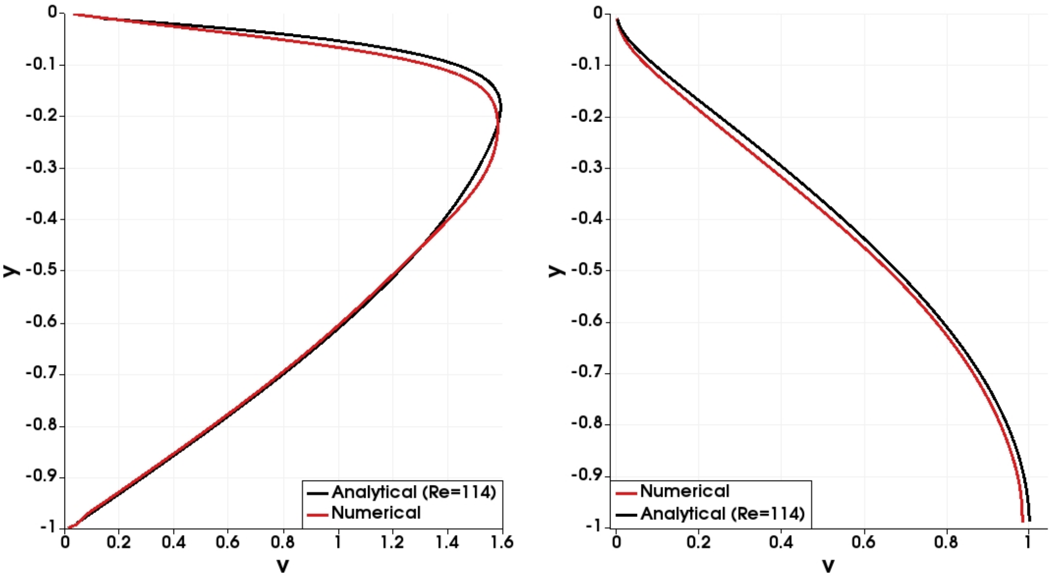

(a) **(b)**

Figure 3.23. Time averaged velocity profile for the wall-injection perturbed simulation

mada and Ishikawa [117], but it does not increase with the distance from the head end. This means that no turbulent instability is growing, as already suggested by the velocity profile, but it is rather related to the perturbed injection. In fact, when the injection is not perturbed, the turbulence intensity peaks in the lower region disappear (see Fig. 3.24b).

3.4.2 Cavity configuration

Since from the experimental data the cavity with ratio $L_\mathrm{c}/D_\mathrm{c} = 1$ resulted the less interesting, in the present section the simulation of the following three cavity

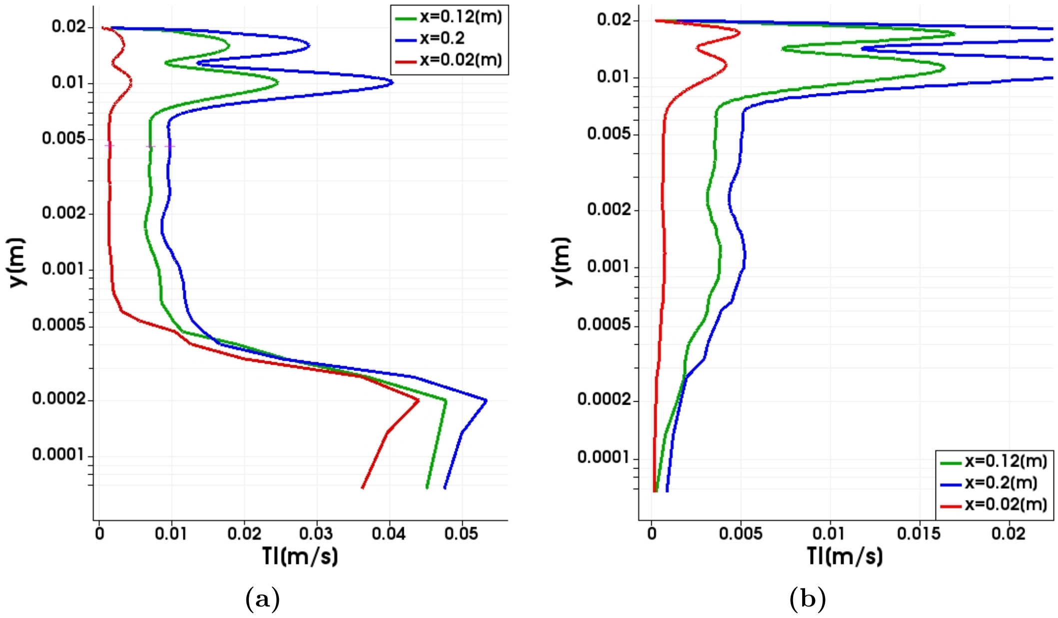

Figure 3.24. Turbulence intensity at three distances from the head end with perturbed injection **(a)** and non-perturbed injection **(b)**

configurations is discussed: $L_c/D_c = 3$ with and without injection from the lower part of the cavity and $L_c/D_c = 6$ with injection from the lower part of the cavity. The time averaged velocity field with streamlines of the three cases is reported in Fig. 3.25. The non-injected cavity behaves like a big recirculating bubble which does not allow the flow to enter in it. In fact, the two profiles of u and v of the non-injected configuration at the abscissa of the upstream corner of the cavity are much more similar to the straight configuration rather than the two injected cases (Fig. 3.26). However, the horizontal velocity profiles, which was the only feature of the flow taken into account by studies about cavity shear layer [120, 141] are almost coincident. Nevertheless, the statistical behaviors are somewhat different each other, as shown by the turbulence intensity in Fig 3.27. If fact, even though in the first half of the longer cavity, the turbulence intensity has a similar behavior for the two injected cases, oscillations at the beginning of the restriction of the longer one are one order of magnitude higher. In the non-injected case, it seems that oscillations are due exclusively to the round motion of the two recirculating zones.

Since these numerical computations solve the compressible Navier-Stokes equations, it is possible to analyze the acoustic field within the computational domain. In particular, acoustic waves can be identified by means of $\|\nabla p\|$. In Fig. 3.28 this quantity has been reported at a given time during the computation for the two injecting cases. It is clearly visible that the two corners of the cavity are two

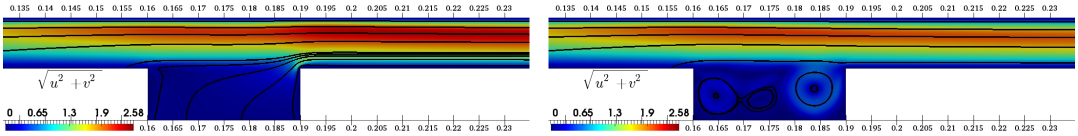

(a) (injecting cavity) **(b)** (non-injecting cavity)

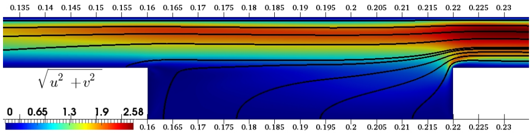

(c) (injecting cavity)

Figure 3.25. Velocity magnitude with streamlines of the three configurations simulated

acoustical quadrupoles and both emit acoustical waves. When the longer cavity is considered, acoustical waves are a little bit more intense and it is possible to observe also the standing waves in the two different aspect ratio regions. Despite the presence of two acoustical sources, they do not provide enough energy disturbance to the shear in order to activate the self-sustained cavity oscillation. In fact, an onset of velocity oscillations—probably due to the initial transition distrurbances—is damped during the evolution, as clearly visible in Fig. 3.29 where the time history of horizontal velocity at three positions along the opening of the cavity is depicted.

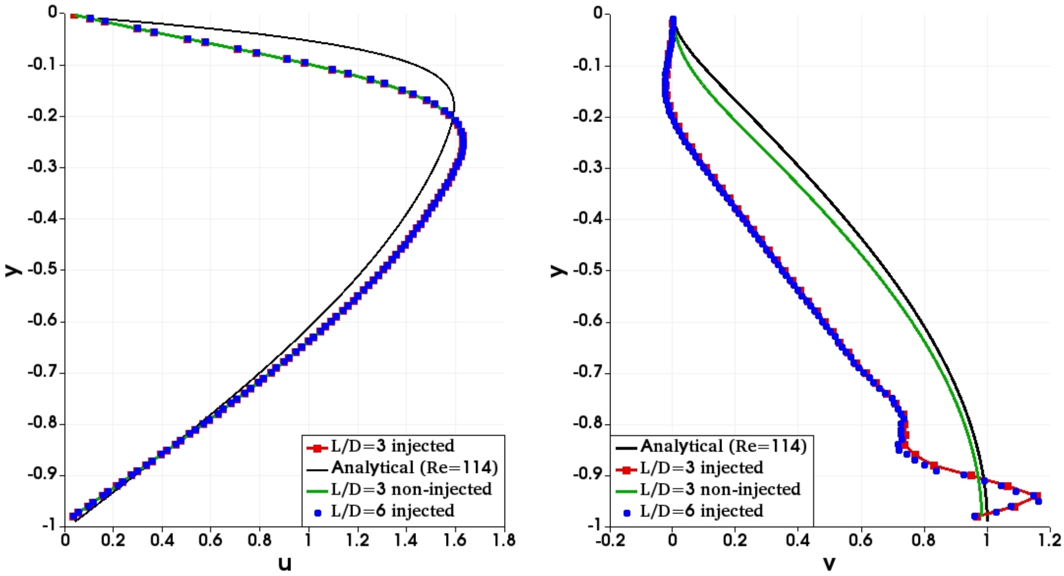

(a) **(b)**

Figure 3.26. Velocity profile at the upstream corner $x = 0.16\,\mathrm{m}$. The maxima of these horizontal velocity profiles is U_e

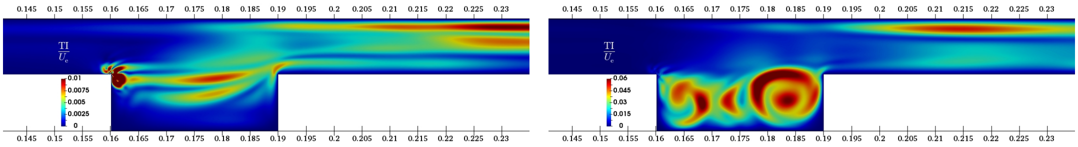

(a) (injecting cavity) **(b)** (non-injecting cavity)

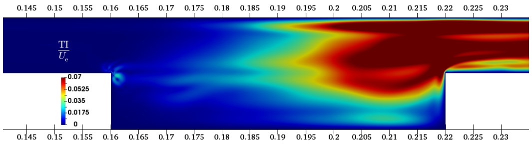

(c) (injecting cavity)

Figure 3.27. Turbulence intensity normalized with respect to the maximum velocity at the upstream corner, U_e, of the three configurations simulated

(a)

(b)

Figure 3.28. Snapshot of $\|\nabla p\|$ for the two injecting cavity configurations

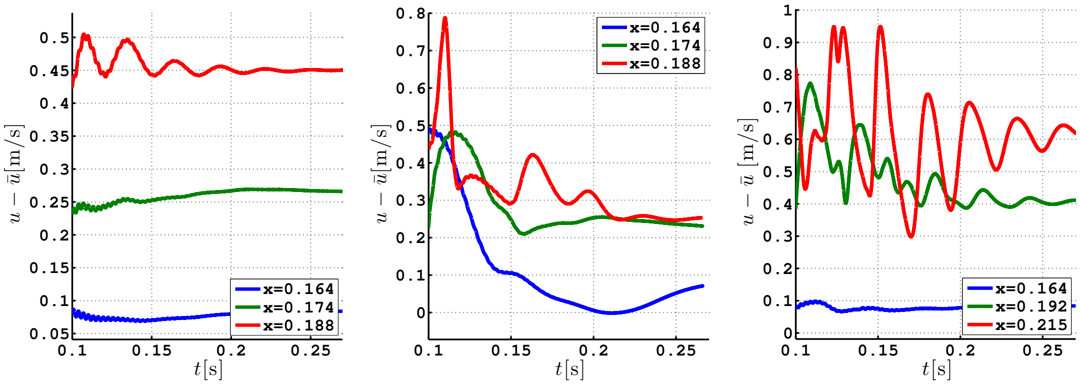

(a) $L_\mathrm{c}/D_\mathrm{c} = 3$ injecting **(b)** $L_\mathrm{c}/D_\mathrm{c} = 3$ non-injecting **(c)** $L_\mathrm{c}/D_\mathrm{c} = 6$ injecting

Figure 3.29. Time history of three velocity probes per configuration along the opening $y = -0.01$

Chapter 4

Concluding remarks

In this work the wall-injected flow within a two-dimensional channel has been studied by means of Particle Image Velocimetry measurements and numerical simulations. Two geometrical configurations have been taken into account. First, a straight channel which is strictly related to film-cooling or transpiration-cooling and propulsive applications has been considered. Then, the presence of a cavity along the channel has been studied. A first phase concerned the design and realization of the experimental apparatus. It was carried on almost in parallel with the development of the in-house numerical code. After that, experimental measurements and numerical simulations have been conducted and compared.

Preliminarily, the experimental apparatus has been tested and the injection has been characterized. The characterization of the inflow condition generated by the injection of air through a porous material revealed the extremely interesting phenomenon of jet-coalescence, which in my opinion should be further investigated for instance taking into account either the three-dimensional effects or its temporal behavior. Anyhow, a sufficiently in-depth description of the flow downward a porous material has been reported and has yielded the input for the numerical description of the inflow boundary condition that would have to be used during a simulation. In particular, an oscillating space profile of injection velocity with a wavelength of the order of the tenth of a millimeter has been found. This spatial non-uniformity, referred to as pseudo-turbulence intensity, seems to increase with the mean velocity magnitude of injection according to previous results of Pimenta and Moffat, Ramachandran, Heaman, and Smith [107, 109], whereas the temporal fluctuations increase with decreasing velocity and porosity.

Analogously, the numerical code has been tested in order to assess its capability to solve the Navier-Stokes equations within a bounded computational domain with strong influencing boundary conditions, such as inflow and outflow conditions. Moreover, being the considered geometry almost closed, acoustical phenomena inside

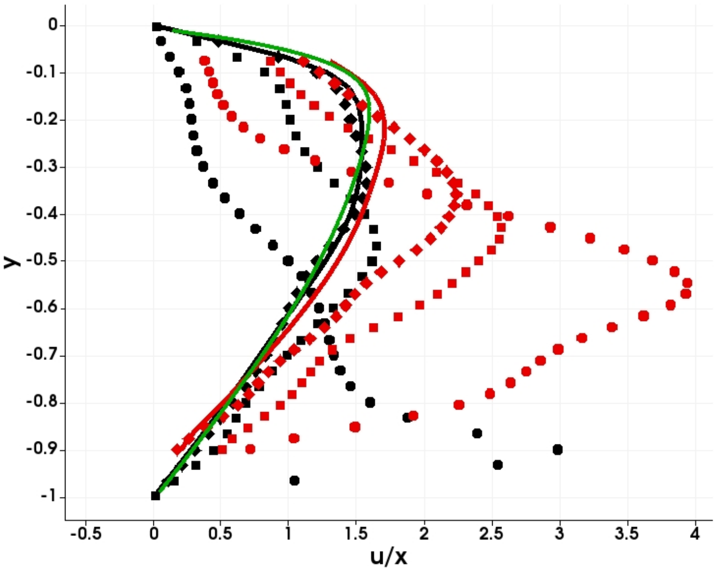

Figure 4.1. Normalized velocity profiles with respect to the horizontal position: experimental (red symbols) and numerical (black symbols). Each symbols represents a different position: $x = 1.9\,\mathrm{mm}$ (circle), $x = 4.7\,\mathrm{mm}$ (square), $x = 7.1\,\mathrm{mm}$ (diamond) and $x = 46\,\mathrm{mm}$ (solid line); green solid line is the steady Navier-Stokes solution

closed and closed-open tube have been simulated.

4.1 Straight configuration comparison

The experimental measurements of the straight configuration shows good accordance with the numerical computation and the analytical model, except for a region close to the head end where the vertical wall influences the computation in a different way from the experimental data (see Fig. 4.1). However, despite the injection non-uniformity observed with the preliminary experimental characterization has been taken into account in the numerical computation, the mean numerical velocity field is not affected by this effect, rather than the experimental one. In fact, in Fig. 4.2, where the mean vertical velocity fields are depicted, the jet-like pattern is still visible in the experimental field and completely disappeared in the numerical one.

The analysis of velocity oscillations by means of Probability Density Function, performed in Sec. 2.4, suggested that fluctuations of u near the aft end of around $10\,\mathrm{cm\,s^{-1}}$ can be led back to acoustics. The numerical results have confirmed that these oscillations are exactly on the natural acoustic frequencies as shown in Fig. 4.3. At the head end, the level of random oscillations is, instead, higher. Nevertheless, the numerical code captured acoustical frequencies also there.

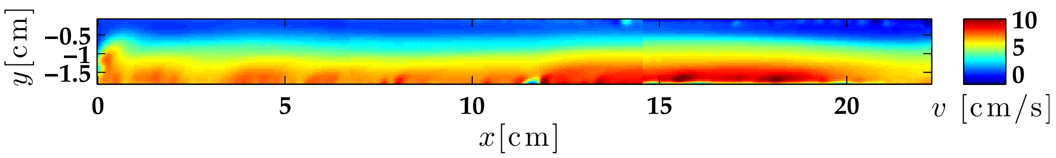

(a) experimental

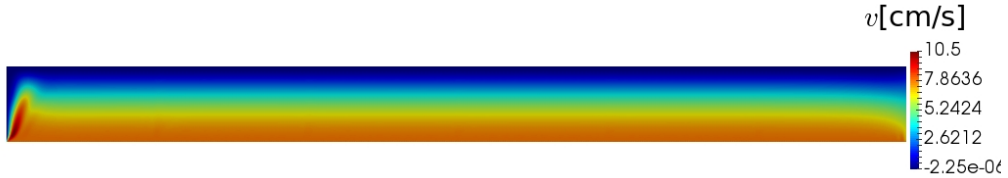

(b) numerical

Figure 4.2. Comparison between experimental and numerical time averaged vertical velocity fields

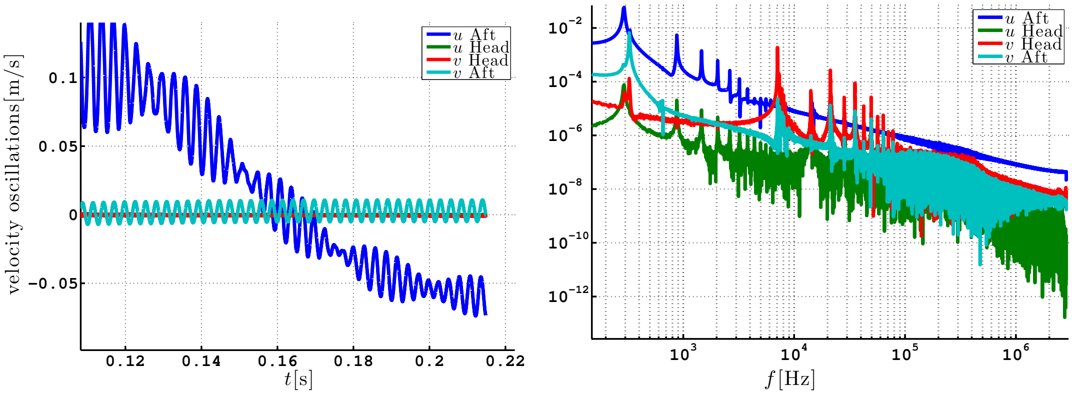

(a) experimental **(b)** numerical

Figure 4.3. Velocity oscillations of the numerical computation at the head end and aft end **(a)** and their spectra in log-log scale **(b)**

4.2 Cavity configuration comparison

The flow over cavities is a fully explored fluid dynamics problem. It was showed that the ratio L_c/D_c together with the characteristic parameters of the upstream velocity profile, i.e. maximum velocity and shape factor, determine the behavior of the cavity flow [120]. However, to the best of the author's knowledge a wall-injected flow has never considered as upstream flow in a cavity study. It is widely shown in the present thesis that the laminar velocity profile generated by means of wall-injection within a channel is different from the classical Poiseuille flow and that, despite the horizontal velocity is zero at the wall, actually the boundary layer is blown off by the vertical

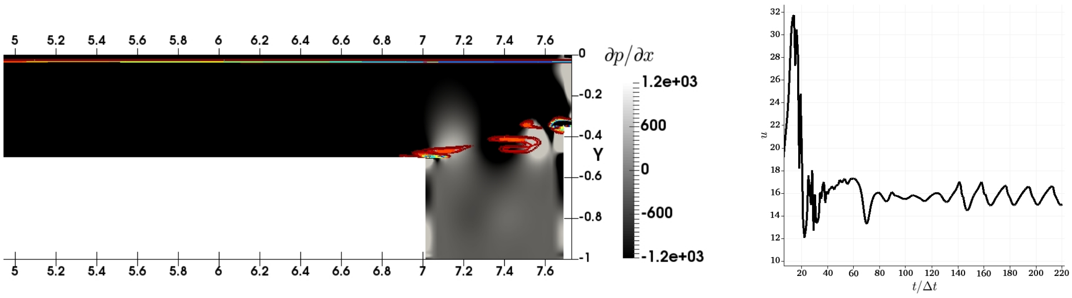

(a) **(b)**

Figure 4.4. Vortex shedding at the cavity shear layer **(a)** and velocity oscillations at a probe located in $(7.5, -0.4)$ **(b)**

injection.

The experimental results presented in this work are an attempt to yield this typical profile at the upstream corner of a cavity. Moreover, the influence of the injection from the bottom of the cavity itself has been analyzed. Unfortunately, it was nearly impossible to provide injection through the corner, hence the flow reattached to the tiny non-injecting region of the corner and the classical parabolic profile has been obtained, see Fig. 2.30. It is possible, instead, to obtain such a profile with the numerical simulation, see Fig. 3.26. This is likely the reason why the experimental results and the numerical one are rather discordant. It should be pointed out that, in particular in the non-injected cavity case, this substantial difference between the upstream velocity profiles is the cause, in the experimental case, of the fact that interaction between the two flows, the one coming from the upstream channel and that within the cavity, takes place inside the cavity, whereas in the numerical conditions the upstream flow never enters into the hollow. It is also plausible that this behavior of the latter case is stressed by the two-dimensionality of the simulation. Although the two approaches provide different results, both are characterized by the absence of self-sustained oscillations.

The most plausible conclusion is that the Reynolds number based on the upstream maximum velocity and the boundary layer thickness is too small. In fact, increasing this parameter, although a slightly different geometry has been considered, the typical vortex shedding [121, 141] appears (see Fig. 4.4). Here the Reynolds number is approximately 10^5, whereas in the previous cases were ≈ 250. It is noteworthy the coupling between vortices and the “global” (of the whole hollow region) pressure field.

4.3 Future work

Shape and level of disturbance injected by the propellant is a challenging and still an open problem. Further investigations on the jet-coalescence phenomenon observed downstream an injecting porous material and, in general, on which is the minimum level of disturbance necessary to trigger the instability of a wall-injected flow are mandatory. Moreover, an effective implementation of perturbations of the inflow condition capable to generate this spatial instability phenomenon should be inspected.

The main limitation of the experimental apparatus presented herein was the small maximum injection provided, nonetheless the results presented herein are in good agreement with analytical and numerical results. It is hence desirable to widen these measurements to higher flow rates.

On the one hand, acoustical phenomena should be investigated experimentally, in order to have a direct comparison with the numerical one. But, on the other a fully compressible formulation, like the one used in the present work, may be relaxed in order to reduce the computational cost. Moreover, three-dimensional computations are mandatory, in particular when cavities are taken into account

Appendix A

BVP solution

In order to solve the following, one–dimensional Boundary Value Problem

$$\begin{cases} FF''' - F'F'' = 0 \\ F(-1) = -1 \\ F(0) = 0 \\ F'(-1) = 0 \end{cases} \tag{A.1}$$

we have to find a solution of the ODE that, at the same time, fulfills the given boundary conditions. Re–writing the ODE as follows

$$\frac{F'}{F} = \frac{F'''}{F''}, \tag{A.2}$$

an integration yields

$$F'' - CF = 0, \tag{A.3}$$

where C is a constant. The sign of C chooses the character of the solution, in fact we have three types of solution

$$F = \begin{cases} Ae^{ky} + Be^{-ky}, & \text{if } C = k^2 > 0; \\ A + By, & \text{if } C = 0; \\ A\cos(ky) + B\sin(ky), & \text{if } C = -k^2 < 0. \end{cases} \tag{A.4}$$

For each case we have to impose the boundary conditions and check whether a solution exists or not.

Exponential solution From the second and the third boundary condition we have

$$\begin{cases} A + B = 0 \\ Ake^{-k} - Bke^{k} = 0 \end{cases} \implies Ak = 0, \tag{A.5}$$

hence, either $A = 0$ or $k = 0$, that is $F \equiv 0$, is in contrast with the first boundary condition.

Linear solution The only linear solution that is equal to 0 at 0 and to 1 at 1 is $F = y$. However, it does not satisfy the vanishing first derivative condition at $y = 1$.

Harmonic solution From the second boundary condition, A is equal to zero and the solution will be sinusoidal. The other two conditions lead to

$$\begin{cases} B \sin(k) = 1 \\ Bk \cos(k) = 0 \end{cases} \tag{A.6}$$

which are satisfied when $B = k = 0$, hence $F \equiv 0$ that is not a solution, but also when

$$\begin{cases} B \sin(k) = 1 \\ Bk \cos(k) = 0 \end{cases} \implies F = (-1)^n \sin\left[\left(\frac{\pi}{2} + n\pi\right) y\right]. \tag{A.7}$$

The unique function that fulfills all the required conditions is the sinusoidal one given in (A.7).

Appendix B

LODI system in y-direction

From conservations of the Riemann invariants along the y-direction characteristics we have

$$\frac{\partial p}{\partial t} - \rho a \frac{\partial v}{\partial t} + \mathcal{M}_1 = 0 \tag{B.1}$$

$$\frac{\partial p}{\partial t} - a^2 \frac{\partial \rho}{\partial t} + \mathcal{M}_2 = 0 \tag{B.2}$$

$$\frac{\partial u}{\partial t} + \mathcal{M}_3 = 0 \tag{B.3}$$

$$\frac{\partial p}{\partial t} + \rho a \frac{\partial v}{\partial t} + \mathcal{M}_4 = 0, \tag{B.4}$$

where

$$\mathcal{M}_1 = \mu_1 \left(\frac{\partial p}{\partial y} - \rho a \frac{\partial v}{\partial y} \right) \tag{B.5}$$

$$\mathcal{M}_2 = -\mu_2 \left(\frac{\partial p}{\partial y} - a^2 \frac{\partial \rho}{\partial y} \right) \tag{B.6}$$

$$\mathcal{M}_3 = \mu_3 \frac{\partial u}{\partial y} \tag{B.7}$$

$$\mathcal{M}_4 = \mu_4 \left(\frac{\partial p}{\partial y} + \rho a \frac{\partial v}{\partial y} \right), \tag{B.8}$$

with $\mu_1 = v - a$, $\mu_2 = \mu_3 = v$ and $\mu_4 = v + a$, are the wave strengths. A possible re-arrangement of Eqs. (B.1)–(B.4) is

$$\frac{\partial p}{\partial t} + \frac{1}{2}(\mathcal{M}_1 + \mathcal{M}_4) = 0 \tag{B.9}$$

$$\frac{\partial u}{\partial t} + \frac{1}{2\rho a}(\mathcal{M}_4 - \mathcal{M}_1) = 0 \tag{B.10}$$

$$\frac{\partial v}{\partial t} + \mathcal{M}_3 = 0 \tag{B.11}$$

$$\frac{\partial \rho}{\partial t} + \frac{1}{a^2}\left(\frac{1}{2}(\mathcal{M}_4 + \mathcal{M}_1) - \mathcal{M}_2\right) = 0. \tag{B.12}$$

The inviscid flux-vector expression as a function of $\mathcal{M}_i$ is

$$\frac{\partial q}{\partial y} = e_1 \tag{B.13}$$

$$\frac{\partial (mv)}{\partial y} = ue_1 + \rho e_2 \tag{B.14}$$

$$\frac{\partial (qu + p)}{\partial y} = \rho e_3 + ve_1 \tag{B.15}$$

$$\frac{\partial (\rho v h)}{\partial y} = qe_3 + \frac{1}{\gamma - 1}e_4 + me_2 + \frac{1}{2}(u^2 + v^2)e_1 \tag{B.16}$$

where

$$e_1 = \frac{1}{a^2}\left[\mathcal{M}_2 + \frac{1}{2}(\mathcal{M}_1 + \mathcal{M}_4)\right] \tag{B.17}$$

$$e_2 = \mathcal{M}_3 \tag{B.18}$$

$$e_3 = \frac{1}{2\rho a}(\mathcal{M}_4 - \mathcal{M}_1) \tag{B.19}$$

$$e_4 = \frac{1}{2}(\mathcal{M}_4 + \mathcal{M}_1). \tag{B.20}$$

Bibliography

[1] J. Hijlkema, M. Prévost, and G. Casalis. “On the importance of reduced scale Ariane 5 P230 solid rocket motor models in the comprehension and prevention of thrust oscillations”. In: *CEAS Space Journal* 1.1 (2011), p. 99. URL: `https://doi.org/10.1007/s12567-011-0008-8`.

[2] J. Majdalani and A. Fist. “Improved Mean Flow Solution for Solid Rocket Motors with a Naturally Developing Swirling Motion”. In: *50th AIAA/ASME/SAE/ASEE Joint Propulsion Conference*. American Institute of Aeronautics and Astronautics, July 2014. URL: `https://doi.org/10.2514/6.2014-4016`.

[3] Ronald S Fry. *Solid propellant test motor scaling*. Tech. rep. 2001.

[4] Stany Gallier and Franck Godfroy. “Aluminum Combustion Driven Instabilities in Solid Rocket Motors”. In: *Journal of Propulsion and Power* 25.2 (Mar. 2009), pp. 509–521. URL: `https://doi.org/10.2514/1.37664`.

[5] Stany Gallier, Emmanuel Radenac, and Franck Godfroy. “Thermoacoustic Instabilities in Solid Rocket Motors”. In: *45th AIAA/ASME/SAE/ASEE Joint Propulsion Conference & Exhibit*. American Institute of Aeronautics and Astronautics, 2009. URL: `https://doi.org/10.2514/6.2009-5252`.

[6] G. Avalon et al. “Numerical computations and visualization tests of the flow inside a cold gas simulation with characterization of a parietal vortex shedding”. In: *Tiré à part – Office national d’études et de recherches aerospatiales* (2001).

[7] F. E. C. Culick. “Acoustic oscillations in solid propellant rocket chambers”. In: *Astronautica Acta* 12.2 (1966), pp. 113–126.

[8] F. E. C. Culick. “Stability of Longitudinal Oscillations with Pressure and Velocity Coupling in a Solid Propellant Rocket”. In: *Combustion Science and Technology* 2.4 (1970), pp. 179–201. URL: `http://dx.doi.org/10.1080/00102207008952247`.

[9] G. P. Sutton and O. Biblarz. *Rocket Propulsion Elements*. Wiley, 2016. URL: `http://eu.wiley.com/WileyCDA/WileyTitle/productCd-1118753658.html`.

[10] E. Cavallini, B. Favini, and A. Neri. "Motor Scale and Propellant Geometry Effects on Pressure Oscillations in Aft-Finocyl Solid Rocket Motors". In: *52nd AIAA/SAE/ASEE Joint Propulsion Conference*. American Institute of Aeronautics and Astronautics, 2016. URL: `https://doi.org/10.2514/6.2016-4793`.

[11] F. M. Skalak and C. Y. Wang. "On the Nonunique Solutions of Laminar Flow Through a Porous Tube or Channel". In: 34.3 (1978), pp. 535–544. URL: `http://www.jstor.org/stable/2100952`.

[12] Y. K. Wu. "Magnetohydrodynamic boundary layer control with suction or injection". In: *Journal of Applied Physics* 44.5 (1973), pp. 2166–2171. URL: `http://dx.doi.org/10.1063/1.1662531`.

[13] G. Alvarez and D. Flick. "Modelling turbulent flow and heat transfer using macro-porous media approach used to predict cooling kinetics of stack of food products". In: *Journal of Food Engineering* 80.2 (2007), pp. 391–401. URL: `http://www.sciencedirect.com/science/article/pii/S0260877406000318`.

[14] K. Yamamoto and Z. I. Yoshida. "Flow through a Porous Wall with Convective Acceleration". In: *Journal of the Physical Society of Japan* 37.3 (1974), pp. 774–779. URL: `http://dx.doi.org/10.1143/JPSJ.37.774`.

[15] I. Lee, D. Kim, and J. Koo. "Breakup structure of two-phase jets with various momentum flux from a porous injector". In: *Journal of Thermal Science* 23.1 (Feb. 1, 2014), pp. 60–67. URL: `http://dx.doi.org/10.1007/s11630-014-0677-7`.

[16] R. E. Hewitt, P. W. Duck, and A. J. Williams. "Injection into boundary layers: solutions beyond the classical form". In: *Journal of Fluid Mechanics* 822 (2017), pp. 617–639. URL: `https://www.cambridge.org/core/article/injection-into-boundary-layers-solutions-beyond-the-classical-form/E79776026542AEA15A1565BC820F685A`.

[17] T. P. Torda. "Boundary Layer Control by Continuous Surface Suction or Injection". In: *Journal of Mathematics and Physics* 31.1-4 (1952), pp. 206–213. URL: `http://dx.doi.org/10.1002/sapm1952311206`.

[18] S. W. Yuan. *Laminar pipe flow with injection and suction through a porous wall*. Tech. rep. Polytechnic Institute of Brooklyn, 1955.

[19] S. W. Yuan. “Further Investigation of Laminar Flow in Channels with Porous Walls”. In: *Journal of Applied Physics* 27.3 (1956), pp. 267–269. URL: `http://dx.doi.org/10.1063/1.1722355`.

[20] R. L. Simpson, R. J. Moffat, and W. M. Kays. “The turbulent boundary layer on a porous plate: Experimental skin friction with variable injection and suction”. In: *International Journal of Heat and Mass Transfer* 12.7 (1969), pp. 771–789. URL: `http://www.sciencedirect.com/science/article/pii/0017931069901811`.

[21] R. J. Goldstein, G. Shavit, and T. S. Chen. “Film-Cooling Effectiveness With Injection Through a Porous Section”. In: *Journal of Heat Transfer* 87.3 (Aug. 1965), pp. 353–359. URL: `http://dx.doi.org/10.1115/1.3689114`.

[22] J. P. Hartnett, R. C. Birkebak, and E. R. G. Eckert. “Velocity Distributions, Temperature Distributions, Effectiveness and Heat Transfer for Air Injected Through a Tangential Slot Into a Turbulent Boundary Layer”. In: *Journal of Heat Transfer* 83.3 (Aug. 1961), pp. 293–305. URL: `http://dx.doi.org/10.1115/1.3682263`.

[23] L. L. Debruge and L. S. Han. “Heat Transfer in a Channel with a Porous Wall for Turbine Cooling Application”. In: *Journal of Heat Transfer* 94.4 (Nov. 1972), pp. 385–390. URL: `http://dx.doi.org/10.1115/1.3449956`.

[24] D. A. Nealy and S. B. Reider. “Evaluation of Laminated Porous Wall Materials for Combustor Liner Cooling”. In: *Journal of Engineering for Power* 102.2 (Apr. 1980), pp. 268–276. URL: `http://dx.doi.org/10.1115/1.3230247`.

[25] K. T. Lee and W. M. Yan. “Mixed convection heat transfer in horizontal rectangular ducts with wall transpiration effects”. In: *International Journal of Heat and Mass Transfer* 41.2 (1998), pp. 411–423. URL: `http://www.sciencedirect.com/science/article/pii/S0017931097001221`.

[26] O. D. Makinde and A. S. Eegunjobi. “Effects of Convective Heating on Entropy Generation Rate in a Channel with Permeable Walls”. In: *Entropy* 15.1 (2013), pp. 220–233. URL: `http://www.mdpi.com/1099-4300/15/1/220`.

[27] Z. Huang et al. “Experimental investigation of full-coverage effusion cooling through perforated flat plates”. In: *Applied Thermal Engineering* 76 (2015), pp. 76–85. URL: `http://www.sciencedirect.com/science/article/pii/S1359431114010904`.

[28] Y. Q. Liu et al. “Experimental and numerical investigation of transpiration cooling for sintered porous flat plates”. In: *Applied Thermal Engineering* 50.1 (2013), pp. 997–1007. URL: `http://www.sciencedirect.com/science/article/pii/S1359431112005510`.

[29] A. S. Berman. “Laminar Flow in Channels with Porous Walls”. In: *Journal of Applied Physics* 24.9 (1953), pp. 1232–1235. URL: `http://dx.doi.org/10.1063/1.1721476`.

[30] J. R. Sellars. “Laminar Flow in Channels with Porous Walls at High Suction Reynolds Numbers”. In: *Journal of Applied Physics* 26.4 (1955), pp. 489–490. URL: `http://dx.doi.org/10.1063/1.1722024`.

[31] F. T. McClure, R. H. Cantrell, and R. W. Hart. “Interaction Between Sound and Flow: Stability of T-Burners”. In: *AIAA Journal* 1.3 (Mar. 1963), pp. 586–590. URL: `https://doi.org/10.2514/3.54846`.

[32] G. Taylor. “Fluid Flow in Regions Bounded by Porous Surfaces”. In: *Proceedings of the Royal Society of London A: Mathematical, Physical and Engineering Sciences* 234.1199 (1956), pp. 456–475. URL: `http://rspa.royalsocietypublishing.org/content/234/1199/456`.

[33] F. E. C. Culick. “Rotational axisymmetric mean flow and damping of acoustic waves in asolid propellant rocket.” In: *AIAA Journal* 4.8 (1966), pp. 1462–1464.

[34] R. M. Terrill. “Laminar Flow in a Uniformly Porous Channel”. In: 15.3 (1964), pp. 299–310. URL: `https://www.cambridge.org/core/article/laminar-flow-in-a-uniformly-porous-channel/23834F0EAF507DCC5341360637571A79`.

[35] R. M. Terrill and G. M. Shrestha. “Laminar flow through parallel and uniformly porous walls of different permeability”. In: *Zeitschrift für angewandte Mathematik und Physik ZAMP* 16.4 (July 1, 1965), pp. 470–482. URL: `http://dx.doi.org/10.1007/BF01593923`.

[36] G. M. Shrestha and R. M. Terrill. “Laminar flow with large injection through parallel and uniformly porous walls of different permeability”. In: *The Quarterly Journal of Mechanics and Applied Mathematics* 21.4 (Nov. 1968), pp. 413–432. URL: `http://dx.doi.org/10.1093/qjmam/21.4.413`.

[37] A. S. Berman. “Effects of porous boundaries on the flow of fluids in systems with various geometries”. In: *Proceedings of the Second United Nations Internatinal Conference on the Peaceful Uses of Atomi Energy.* Vol. 4. 1958, pp. 351–358.

[38] S. W. Yuan. “Heat Transfer in Laminar Pipe Flow With Uniform Coolant Injection”. In: *Journal of Jet Propulsion* 28.3 (Mar. 1958), pp. 178–181. URL: `https://doi.org/10.2514/8.7264`.

[39] M. Morduchow. “On laminar flow through a channel or tube with injection: application of method of averages”. In: *Quarterly of Applied Mathematics* 14.4 (1957), pp. 361–368. URL: `http://www.jstor.org/stable/43636013`.

[40] R. M. Terrill and P. W. Thomas. “On laminar flow through a uniformly porous pipe”. In: *Applied Scientific Research* 21.1 (Jan. 1, 1969), pp. 37–67. URL: `http://dx.doi.org/10.1007/BF00411596`.

[41] H. L. Weissberg. “Laminar Flow in the Entrance Region of a Porous Pipe”. In: *The Physics of Fluids* 2.5 (1959), pp. 510–516. URL: `http://aip.scitation.org/doi/abs/10.1063/1.1705941`.

[42] H. S. Mickley et al. *Heat, mass and momentum transfer for flow over a flat plate with blowing or suction.* Tech. rep. 3208. Massachusetts Institute of Technology, July 1954.

[43] W. E. Wageman and F. A. Guevara. “Fluid Flow through a Porous Channel”. In: *The Physics of Fluids* 3.6 (1960), pp. 878–881. URL: `http://aip.scitation.org/doi/abs/10.1063/1.1706151`.

[44] H. S. Mickley and R. S. Davis. *Momentum transfer for flow over a flat plate with blowing.* Tech. rep. 4017. Massachusetts Institute of Technology, Nov. 1957.

[45] R. J. Moffat and W. M. Kays. “The turbulent boundary layer on a porous plate: Experimental heat transfer with uniform blowing and suction”. In: *International Journal of Heat and Mass Transfer* 11.10 (1968), pp. 1547–1566. URL: `http://www.sciencedirect.com/science/article/pii/0017931068901166`.

[46] R. D. Bundy and H. L. Weissberg. “Experimental Study of Fully Developed Laminar Flow in a Porous Pipe with Wall Injection”. In: *The Physics of Fluids* 13.10 (1970), pp. 2613–2615. URL: `http://aip.scitation.org/doi/abs/10.1063/1.1692835`.

[47] Y. C. Cheng and G. J. Hwang. “Experimental studies of laminar flow and heat transfer in a one-porous-wall square duct with wall injection”. In: *International Journal of Heat and Mass Transfer* 38.18 (1995), pp. 3475–3484. URL: `http://www.sciencedirect.com/science/article/pii/001793109500037A`.

[48] G. D. Raithby and D. C. Knudsen. “Hydrodynamic Development in a Duct With Suction and Blowing”. In: *Journal of Applied Mechanics* 41.4 (Dec. 1974), pp. 896–902. URL: `http://dx.doi.org/10.1115/1.3423479`.

[49] F. J. S. Bandeira et al. "Turbulence and Bubble Break up in Slug Flow with Wall Injection". In: *Flow, Turbulence and Combustion* 98.3 (2017), pp. 923–945.

[50] W. Dahmen et al. "Numerical boundary layer investigations of transpiration-cooled turbulent channel flow". In: *International Journal of Heat and Mass Transfer* 86 (2015), pp. 90–100. URL: `http://www.sciencedirect.com/science/article/pii/S0017931015002483`.

[51] W. Dahmen et al. "Numerical simulation of transpiration cooling through porous material". In: *International Journal for Numerical Methods in Fluids* 76.6 (2014), pp. 331–365. URL: `http://dx.doi.org/10.1002/fld.3935`.

[52] G. Brillant, S. Husson, and F. Bataille. "Experimental study of the blowing impact on a hot turbulent boundary layer". In: *International Journal of Heat and Mass Transfer* 51.7 (2008), pp. 1996–2005. URL: `http://www.sciencedirect.com/science/article/pii/S0017931007004073`.

[53] S. J. Alsaji and L. K. Isaacson. "Temperature laws for a turbulent boundary layer with injection and heat transfer." In: *AIAA Journal* 7.1 (Jan. 1969), pp. 157–159. URL: `https://doi.org/10.2514/3.5055`.

[54] F. E. C. Culick and P. Kuentzmann. *Unsteady motions in combustion chambers for propulsion systems.* Tech. rep. California Institute of Technology, 2006.

[55] G. A. Flandro. "On flow turning". In: *31st Joint Propulsion Conference and Exhibit.* American Institute of Aeronautics and Astronautics, 2017/07/20 1995. URL: `https://doi.org/10.2514/6.1995-2730`.

[56] G. A. Flandro. "Effects of vorticity on rocket combustion stability". In: *Journal of Propulsion and Power* 11.4 (July 1995), pp. 607–625. URL: `https://doi.org/10.2514/3.23887`.

[57] J. Majdalani and G. A. Flandro. "Rocket Gas Dynamics for an Arbitrary Mean Flowfield". In: *38th AIAA/ASME/SAE/ASEE Joint Propulsion Conference & Exhibit.* American Institute of Aeronautics and Astronautics, 2017/07/20 2002. URL: `https://doi.org/10.2514/6.2002-3891`.

[58] R. S. R. Brown, P. G. Willoughby, and R. Dunlap. "Coupling between velocity oscillations and solid propellant combustion". In: *22nd Aerospace Sciences Meeting.* American Institute of Aeronautics and Astronautics, Jan. 1984. URL: `https://doi.org/10.2514/6.1984-288`.

[59] R. Dunlap et al. "Internal flow field studies in a simulated cylindrical port rocket chamber". In: *Journal of Propulsion and Power* 6.6 (Nov. 1990), pp. 690–704. URL: `https://doi.org/10.2514/3.23274`.

[60] Y. Ma, W. K. Van Moorhem, and R. W. Shorthill. “Experimental investigation of velocity coupling in combustion instability”. In: *Journal of Propulsion and Power* 7.5 (Sept. 1991), pp. 692–699. URL: `https://doi.org/10.2514/3.23381`.

[61] J. T. Barron, W. K. Van Moorhem, and J. Majdalani. “A novel investigation of the oscillatory field over a transpiring surface”. In: *Journal of Sound and Vibration* 235.2 (2000), pp. 281–297. URL: `http://www.sciencedirect.com/science/article/pii/S0022460X00929201`.

[62] N. Zgheib and J. Majdalani. “Axial Waves in Simulated Solid Rocket Motors”. In: *46th AIAA/ASME/SAE/ASEE Joint Propulsion Conference & Exhibit*. American Institute of Aeronautics and Astronautics, July 2010. URL: `https://doi.org/10.2514/6.2010-6993`.

[63] J. Majdalani and W. K. Van Moorhem. “Improved Time-Dependent Flowfield Solution for Solid Rocket Motors”. In: *AIAA Journal* 36.2 (Feb. 1998), pp. 241–248. URL: `https://doi.org/10.2514/2.7507`.

[64] Q. Zhao et al. “Acoustically generated vorticity in an internal flow”. In: *Journal of Fluid Mechanics* 413 (2000), pp. 247–285.

[65] B. A. Maicke and J. Majdalani. “On the rotational compressible Taylor flow in injection-driven porous chambers”. In: *Journal of Fluid Mechanics* 603 (2008), pp. 391–411.

[66] B. A. Maicke, T. Saad, and J. Majdalani. “On the compressible Hart-McClure and Sellars mean flow motions”. In: *Physics of Fluids* 24.9 (2012), pp. 096–101. URL: `http://dx.doi.org/10.1063/1.4748349`.

[67] G. Balakrishnan, A. Linan, and F. A. Williams. “Compressibility effects in thin channels with injection”. In: *AIAA Journal* 29.12 (Dec. 1991), pp. 2149–2154. URL: `https://doi.org/10.2514/3.10852`.

[68] J. Majdalani, A. B. Vyas, and G. A. Flandro. “Higher Mean-Flow Approximation for Solid Rocket Motors with Radially Regressing Walls”. In: *AIAA Journal* 40.9 (Sept. 2002), pp. 1780–1788. URL: `https://doi.org/10.2514/2.1854`.

[69] J. Majdalani and C. Zhou. “Moderate-to-large injection and suction driven channel flows with expanding or contracting walls”. In: *ZAMM - Journal of Applied Mathematics and Mechanics / Zeitschrift für Angewandte Mathematik und Mechanik* 83.3 (Mar. 2003), pp. 181–196. URL: `http://dx.doi.org/10.1002/zamm.200310018`.

[70] E. C. Dauenhauer and J. Majdalani. "Exact self-similarity solution of the Navier–Stokes equations for a porous channel with orthogonally moving walls". In: *Physics of Fluids* 15.6 (2003), pp. 1485–1495. URL: `http://aip.scitation.org/doi/abs/10.1063/1.1567719`.

[71] Y. Z. Boutros et al. "Lie-group method for unsteady flows in a semi-infinite expanding or contracting pipe with injection or suction through a porous wall". In: *Journal of Computational and Applied Mathematics* 197.2 (2006), pp. 465–494. URL: `http://www.sciencedirect.com/science/article/pii/S0377042705006941`.

[72] S. Dinarvand and M. M. Rashidi. "A reliable treatment of a homotopy analysis method for two-dimensional viscous flow in a rectangular domain bounded by two moving porous walls". In: *Nonlinear Analysis: Real World Applications* 11.3 (2010), pp. 1502–1512. URL: `http://www.sciencedirect.com/science/article/pii/S1468121809001485`.

[73] Z. G. Makukula, P. Sibanda, and S. S. Motsa. "A Novel Numerical Technique for Two-Dimensional Laminar Flow between Two Moving Porous Walls". In: *Mathematical Problems in Engineering* (2010), p. 15. URL: `http://dx.doi.org/10.1155/2010/528956%20%]%20528956`.

[74] K. N. Volkov. "Simulation of a Fluid Flow in a Channel with a Moving Side Surface and Injection". English. In: *Journal of Engineering Physics and Thermophysics* 86.6 (2013). Translated from Inzhenerno-Fizicheskii Zhurnal, Vol. 86, No. 6, pp. 1359–1365, November–December, 2013., pp. 1447–1453.

[75] G. Casalis, G. Avalon, and J. P. Pineau. "Spatial instability of planar channel flow with fluid injection through porous walls". In: *Physics of Fluids* 10.10 (1998), pp. 2558–2568. URL: `http://dx.doi.org/10.1063/1.869770`.

[76] G. Avalon, G. Casalis, and J. Griffond. "Flow instabilities and acoustic resonance of channels with wall injection". In: *34th AIAA/ASME/SAE/ASEE Joint Propulsion Conference and Exhibit*. American Institute of Aeronautics and Astronautics, 1998. URL: `https://doi.org/10.2514/6.1998-3218`.

[77] R. S. Brown et al. "Vortex Shedding as a Source of Acoustic Energy in Segmented Solid Rockets". In: *Journal of Spacecraft and Rockets* 18.4 (July 1981), pp. 312–319. URL: `https://doi.org/10.2514/3.57822`.

[78] F. Vuillot. "Vortex-shedding phenomena in solid rocket motors". In: *Journal of Propulsion and Power* 11.4 (July 1995), pp. 626–639. URL: `https://doi.org/10.2514/3.23888`.

[79] J. Griffond, G. Casalis, and J. P. Pineau. “Spatial instability of flow in a semiinfinite cylinder with fluid injection through its porous walls”. In: *European Journal of Mechanics - B/Fluids* 19.1 (2000), pp. 69–87. URL: `http://www.sciencedirect.com/science/article/pii/S0997754600001059`.

[80] J. Griffond and G. Casalis. “Secondary instability of the planar Taylor flow”. In: *36th AIAA/ASME/SAE/ASEE Joint Propulsion Conference and Exhibit*. American Institute of Aeronautics and Astronautics, 2000. URL: `https://doi.org/10.2514/6.2000-3806`.

[81] F. Chedevergne, G. Casalis, and T. Féraille. “Biglobal linear stability analysis of the flow induced by wall injection”. In: *Physics of Fluids* 18.1 (2006), p. 014103. URL: `http://dx.doi.org/10.1063/1.2160524`.

[82] S. Cerqueira, G. Avalon, and F. Feyel. “An Experimental Investigation of Fluid-Structure Interaction Inside Solid Propellant Rocket Motors”. In: *45th AIAA/ASME/SAE/ASEE Joint Propulsion Conference & Exhibit*. American Institute of Aeronautics and Astronautics, 2009. URL: `https://doi.org/10.2514/6.2009-5427`.

[83] F. Chedevergne, G. Casalis, and J. Majdalani. “Direct numerical simulation and biglobal stability investigations of the gaseous motion in solid rocket motors”. In: *Journal of Fluid Mechanics* 706 (2012), pp. 190–218.

[84] S. V. Apte and V. Yang. “Unsteady Flow Evolution in Porous Chamber with Surface Mass Injection, Part 1: Free Oscillation”. In: *AIAA Journal* 39.8 (Aug. 2001), pp. 1577–1586. URL: `https://doi.org/10.2514/2.1483`.

[85] S. V. Apte and V. Yang. “Unsteady Flow Evolution in Porous Chamber with Surface Mass Injection, Part 2: Acoustic Excitation”. In: *AIAA Journal* 40.2 (Feb. 2002), pp. 244–253. URL: `https://doi.org/10.2514/2.1666`.

[86] S. V. Apte and V. Yang. “A large-eddy simulation study of transition and flow instability in a porous-walled chamber with mass injection”. In: *Journal of Fluid Mechanics* 477 (2003), pp. 215–225.

[87] G. Casalis, G. Boyer, and E. Radenac. “Some recent advances in the instabilities occurring in long Solid Rocket Motors”. In: *47th AIAA/ASME/SAE/ASEE Joint Propulsion Conference & Exhibit*. American Institute of Aeronautics and Astronautics, 2011. URL: `https://doi.org/10.2514/6.2011-5642`.

[88] G. Boyer, G. Casalis, and J. L. Estivalezes. “Theoretical Investigation of the Parietal Vortex Shedding in Solid Rocket Motors”. In: *48th AIAA/ASME/SAE/ASEE Joint Propulsion Conference & Exhibit*. American Institute of Aeronautics and Astronautics, 2012. URL: `https://doi.org/10.2514/6.2012-3825`.

[89] G. Boyer, G. Casalis, and J. L. Estivalèzes. “Stability analysis and numerical simulation of simplified solid rocket motors”. In: *Physics of Fluids* 25.8 (2013), p. 084109. URL: `http://dx.doi.org/10.1063/1.4818552`.

[90] J. Majdalani. “Asymptotic Adaptation of the Taylor-Culick Mean Flow Profile to Rockets with Non-Circular Grain Perforations”. In: *49th AIAA/ASME/SAE/ASEE Joint Propulsion Conference*. American Institute of Aeronautics and Astronautics, July 2013. URL: `https://doi.org/10.2514/6.2013-3916`.

[91] N. Lupoglazoff and F. Vuillot. “Two-dimensional numerical simulation of the stability of a solid propellant rocket motor”. In: *29th Aerospace Sciences Meeting*. American Institute of Aeronautics and Astronautics, Jan. 1991. URL: `https://doi.org/10.2514/6.1991-205`.

[92] N. Lupoglazoff and F. Vuillot. “Numerical simulation of vortex shedding phenomenon in 2D test case solid rocket motors”. In: *30th Aerospace Sciences Meeting and Exhibit*. American Institute of Aeronautics and Astronautics, 1992. URL: `https://doi.org/10.2514/6.1992-776`.

[93] A. Kourta. “Acoustic-mean flow interaction and vortex shedding in solid rocket motors vortex shedding in solid rocket motors”. In: *International Journal for Numerical Methods in Fluids* 22.6 (1996), pp. 449–465. URL: `http://dx.doi.org/10.1002/(SICI)1097-0363(19960330)22:6%3C449::AID-FLD320%3E3.0.CO;2-W`.

[94] N. Lupoglazoff and F. Vuillot. “Parietal vortex shedding as a cause of instability for long solid propellant motors - Numerial simulations and comparisons with firing tests”. In: *34th Aerospace Sciences Meeting and Exhibit*. American Institute of Aeronautics and Astronautics, Jan. 1996. URL: `https://doi.org/10.2514/6.1996-761`.

[95] N. Lupoglazoff and F. Vuillot. “Numerical simulations of parietal vortex-shedding phenomenon in a cold flow set-up”. In: *34th AIAA/ASME/SAE/ASEE Joint Propulsion Conference and Exhibit*. American Institute of Aeronautics and Astronautics, July 1998. URL: `https://doi.org/10.2514/6.1998-3220`.

[96] G. Avalon and D. Lambert. “Cold Gas Experiments Applied to the Understanding of Aeroacoustic Phenomena Inside Solid Propellant Boosters”. In: *42nd AIAA/ASME/SAE/ASEE Joint Propulsion Conference & Exhibit*. American Institute of Aeronautics and Astronautics, 2006. URL: `https://doi.org/10.2514/6.2006-5111`.

[97] E. Cavallini et al. "SRM Internal Ballistic Numerical Simulation by SPINBALL Model". In: *45th AIAA/ASME/SAE/ASEE Joint Propulsion Conference & Exhibit.* American Institute of Aeronautics and Astronautics, 2009. URL: `https://doi.org/10.2514/6.2009-5512`.

[98] A. Di Mascio et al. "Vortex-Sound Generation and Thrust Unsteadiness in Aft-Finocyl Solid Rocket Motor". In: *51st AIAA/SAE/ASEE Joint Propulsion Conference.* American Institute of Aeronautics and Astronautics, 2015. URL: `https://doi.org/10.2514/6.2015-3974`.

[99] M. Raffel et al. *Particle Image Velocimetry: A Practical Guide.* Experimental Fluid Mechanics. Springer Berlin Heidelberg, 2007. URL: `https://books.google.it/books?id=fdKd50rzfuMC`.

[100] Fulvio Scarano et al. "On the use of helium-filled soap bubbles for large-scale tomographic PIV in wind tunnel experiments". In: *Experiments in Fluids* 56.2 (2015), p. 42. URL: `https://doi.org/10.1007/s00348-015-1909-7`.

[101] J. Westerweel, P. F. Geelhoed, and R. Lindken. "Single-pixel resolution ensemble correlation for micro-PIV applications". In: *Experiments in Fluids* 37.3 (2004), pp. 375–384. URL: `https://doi.org/10.1007/s00348-004-0826-y`.

[102] Sven Scharnowski, Rainer Hain, and Christian J. Kähler. "Reynolds stress estimation up to single-pixel resolution using PIV-measurements". In: *Experiments in Fluids* 52.4 (2012), pp. 985–1002. URL: `https://doi.org/10.1007/s00348-011-1184-1`.

[103] W. Thielicke and E. J. Stamhuis. "PIVlab - Time-Resolved Digital Particle Image Velocimetry Tool for MATLAB". In: (Mar. 2015). URL: `https://figshare.com/articles/PIVlab_version_1_35/1092508`.

[104] D. Garcia. "Robust smoothing of gridded data in one and higher dimensions with missing values". In: *Computational Statistics & Data Analysis* 54.4 (2010), pp. 1167–1178. URL: `http://www.sciencedirect.com/science/article/pii/S0167947309003491`.

[105] P. G. Morgan. "The Stability of Flow Through Porous Screens". In: *The Journal of the Royal Aeronautical Society* 64.594 (1960), pp. 359–362.

[106] P. Bradshaw. "The effect of wind-tunnel screens on nominally two-dimensional boundary layers". In: *Journal of Fluid Mechanics* 22.4 (1965), pp. 679–687.

[107] M. Pimenta and R. J. Moffat. "Stability of Flow through Porous Plates: Coalescent Jets Effect". In: *AIAA Journal* 12.10 (Oct. 1974), pp. 1438–1440. URL: `https://doi.org/10.2514/3.49512`.

[108] R. A. Beddini. “Injection-induced flows in porous-walled ducts”. In: *AIAA Journal* 24.11 (Nov. 1986), pp. 1766–1773. URL: `https://doi.org/10.2514/3.9522`.

[109] N. Ramachandran, J. Heaman, and A. Smith. “An experimental study of the flow emerging from porous walls”. In: *Experiments in Fluids* 18.1 (Dec. 1, 1994), pp. 119–128. URL: `https://doi.org/10.1007/BF00209368`.

[110] K. -O. Tong and C. J. Knight. “Flow around an isolated porous tube with nonuniform wall thickness”. In: *AIAA Journal* 17.11 (Nov. 1979), pp. 1262–1263. URL: `https://arc.aiaa.org/doi/abs/10.2514/3.7620`.

[111] Y. Yeh et al. “Injection-induced flow from porous medium in cold-flow simulation of solid rocket motors”. In: *30th Joint Propulsion Conference and Exhibit*. American Institute of Aeronautics and Astronautics, 2017/08/12 1994. URL: `https://doi.org/10.2514/6.1994-3293`.

[112] L. Massa et al. “Fluctuations above a burning heterogeneous propellant”. In: *Journal of Fluid Mechanics* 581 (2007), pp. 1–32.

[113] Reuben M. Olson and E. R. G. Eckert. “Experimental Studies of Turbulent Flow in a Porous Circular Tube With Uniform Fluid Injection Through the Tube Wall”. In: *Journal of Applied Mechanics* 33.1 (Mar. 1966), pp. 7–17. URL: `http://dx.doi.org/10.1115/1.3625030`.

[114] K. Huesmann and E. R. G. Eckert. “Studies of the Laminar Flow and the Transition to Turbulence in Porous Tubes with Uniform Injection Through the Tube Wall”. In: *Warme-und Stoffubertragung* (1968).

[115] VI Yagodkin. *Use of channels with porous walls for studying flows which occur during combustion of solid propellants*. Tech. rep. 1980.

[116] Jinhee Jeong and Fazle Hussain. “On the identification of a vortex”. In: *Journal of Fluid Mechanics* 285 (Feb. 25, 1995), pp. 69–94. URL: `https://www.cambridge.org/core/article/div-class-title-on-the-identification-of-a-vortex-div/D26006DDB95FB28DA80E28A581182DF1`.

[117] K. Yamada and N. Ishikawa. “Simulative Study on the Erosive Burning of Solid Rocket Motors”. In: *AIAA Journal* 14.9 (2017/03/20 1976), pp. 1170–1176. URL: `https://arc.aiaa.org/doi/abs/10.2514/3.61451`.

[118] D. Laboureur, B. Tóth, and J. Anthoine. “Investigation of the Taylor-Culick Flow Through Particle Image Velocimetry and Numerical Simulation”. In: *AIAA Journal* 48.6 (2017/04/06 2010), pp. 1077–1084. URL: `http://dx.doi.org/10.2514/1.44616`.

[119] K. W. Dotson, S. Koshigoe, and K. K. Pace. “Vortex Shedding in a Large Solid Rocket Motor Without Inhibitors at the Segment Interfaces”. In: *Journal of Propulsion and Power* 13.2 (2017/09/28 1997), pp. 197–206. URL: `https://doi.org/10.2514/2.5170`.

[120] Virendra Sarohia. “Experimental Investigation of Oscillations in Flows Over Shallow Cavities”. In: *AIAA Journal* 15.7 (2017/09/28 1977), pp. 984–991. URL: `https://doi.org/10.2514/3.60739`.

[121] J.E. Rossiter. *Wind-tunnel Experiments on the Flow Over Rectangular Cavities at Subsonic and Transonic Speeds*. Reports and memoranda. H.M. Stationery Office, 1967. URL: `https://books.google.it/books?id=w5tJGwAACAAJ`.

[122] F. Daude et al. “A high-order finite-difference algorithm for direct computation of aerodynamic sound”. In: *Computers & Fluids* 61.Supplement C (2012), pp. 46–63. URL: `http://www.sciencedirect.com/science/article/pii/S0045793011002696`.

[123] Christopher K. W. Tam and Jay C. Webb. “Dispersion-Relation-Preserving Finite Difference Schemes for Computational Acoustics”. In: *Journal of Computational Physics* 107.2 (1993), pp. 262–281. URL: `http://www.sciencedirect.com/science/article/pii/S0021999183711423`.

[124] Christophe Bogey and Christophe Bailly. “A family of low dispersive and low dissipative explicit schemes for flow and noise computations”. In: *Journal of Computational Physics* 194.1 (2004), pp. 194–214. URL: `http://www.sciencedirect.com/science/article/pii/S0021999103004662`.

[125] Julien Berland et al. “High-order, low dispersive and low dissipative explicit schemes for multiple-scale and boundary problems”. In: *Journal of Computational Physics* 224.2 (2007), pp. 637–662. URL: `http://www.sciencedirect.com/science/article/pii/S0021999106005420`.

[126] A. Jameson, Wolfgang Schmidt, and Eli Turkel. “Numerical solution of the Euler equations by finite volume methods using Runge Kutta time stepping schemes”. In: *14th Fluid and Plasma Dynamics Conference*. American Institute of Aeronautics and Astronautics, 2017/10/09 1981. URL: `https://doi.org/10.2514/6.1981-1259`.

[127] Oleg V. Vasilyev, Thomas S. Lund, and Parviz Moin. “A General Class of Commutative Filters for LES in Complex Geometries”. In: *Journal of Computational Physics* 146.1 (1998), pp. 82–104. URL: `http://www.sciencedirect.com/science/article/pii/S0021999198960600`.

[128] Christopher K. W. Tam, Jay C. Webb, and Zhong Dong. “A STUDY OF THE SHORT WAVE COMPONENTS IN COMPUTATIONAL ACOUSTICS”. In: *Journal of Computational Acoustics* 01.01 (2017/10/09 1993), pp. 1–30. URL: `https://doi.org/10.1142/S0218396X93000020`.

[129] Miguel R. Visbal and Datta V. Gaitonde. “Very high-order spatially implicit schemes for computational acoustics on curvilinear meshes”. In: *Journal of Computational Acoustics* 09.04 (2017/10/09 2001), pp. 1259–1286. URL: `https://doi.org/10.1142/S0218396X01000541`.

[130] Kevin W Thompson. “Time dependent boundary conditions for hyperbolic systems”. In: *Journal of Computational Physics* 68.1 (1987), pp. 1–24. URL: `http://www.sciencedirect.com/science/article/pii/0021999187900416`.

[131] T. J Poinsot and S. K Lele. “Boundary conditions for direct simulations of compressible viscous flows”. In: *Journal of Computational Physics* 101.1 (1992), pp. 104–129. URL: `http://www.sciencedirect.com/science/article/pii/0021999192900462`.

[132] Guido Lodato, Pascale Domingo, and Luc Vervisch. “Three-dimensional boundary conditions for direct and large-eddy simulation of compressible viscous flows”. In: *Journal of Computational Physics* 227.10 (2008), pp. 5105–5143. URL: `http://www.sciencedirect.com/science/article/pii/S0021999108000685`.

[133] Marianne Cuif Sjöstrand, Yves D’Angelo, and Eric Albin. “No-slip wall acoustic boundary condition treatment in the incompressible limit”. In: *Computers & Fluids* 86.Supplement C (2013), pp. 92–102. URL: `http://www.sciencedirect.com/science/article/pii/S0045793013002867`.

[134] David H. Rudy and John C. Strikwerda. “A nonreflecting outflow boundary condition for subsonic navier-stokes calculations”. In: *Journal of Computational Physics* 36.1 (1980), pp. 55–70. URL: `http://www.sciencedirect.com/science/article/pii/0021999180901746`.

[135] Wolfgang Polifke, Clifton Wall, and Parviz Moin. “Partially reflecting and non-reflecting boundary conditions for simulation of compressible viscous flow”. In: *Journal of Computational Physics* 213.1 (2006), pp. 437–449. URL: `http://www.sciencedirect.com/science/article/pii/S0021999105003876`.

[136] Jan Kopitz, Eduard Bröcker, and Wolfgang Polifke. “Characteristics-based filter for identification of planar acoustic waves in numerical simulation of turbulent compressible flow”. In:

[137] S. Chandrasekhar. *Hydrodynamic and Hydromagnetic Stability*. Dover Books on Physics Series. Dover Publications, 1961. URL: `https://books.google.it/books?id=oU%5C_-6ikmidoC`.

[138] Alice Harang et al. “Kelvin–Helmholtz instability in the presence of variable viscosity for mudflow resuspension in estuaries”. In: *Environmental Fluid Mechanics* 14.4 (2014), pp. 743–769. URL: `https://doi.org/10.1007/s10652-014-9337-4`.

[139] A. K. Saha, K. Muralidhar, and G. Biswas. “Experimental study of flow past a square cylinder at high Reynolds numbers”. In: *Experiments in Fluids* 29.6 (2000), pp. 553–563. URL: `https://doi.org/10.1007/s003480000123`.

[140] Shih-Chieh Lo, Klaus A. Hoffmann, and Jean-Francois Dietiker. “Numerical Investigation of High Reynolds Number Flows over Square and Circular Cylinders”. In: *Journal of Thermophysics and Heat Transfer* 19.1 (2017/10/18 2005), pp. 72–80. URL: `https://doi.org/10.2514/1.9195`.

[141] M. Gharib and A. Roshko. “The effect of flow oscillations on cavity drag”. In: *Journal of Fluid Mechanics* 177 (1987), pp. 501–530.